Study of Nitrous Oxide Production in the Nitric Acid Process

by

Anton Fadic Eulefi

A thesis submitted in partial fulfillment of the requirements for the degree of

Doctor of Philosophy

in

CHEMICAL ENGINEERING

Department of Chemical and Materials Engineering

University of Alberta

Abstract

This work contains investigations relevant for the study of catalytic chemical reactors using the detailed microkinetics approach, with the intent of improving the prediction of the product distribution. The study is comprised of two main topics. The first one consists of an investigation of computational simplification for the chemistry. Two main approaches are studied. Firstly is the Lookup Table approach, where different techniques are explored with their limitations. The second approach is Neural Networks, which was found to provide lower memory requirements for the test case, and it can be computed by at least two orders of magnitude faster than the lookup table and than the direct computation of the chemistry. The second main area of investigation of this thesis consists of the study of the ammonia oxidation reactor, considering a chemical mechanism that shows reliable results based on the available literature. Different domains are studied, and the Sh and Nu numbers are investigated for these cases. It was found that correlations can predict accurately the wire temperature and the mass transfer coefficient. The production of the greenhouse gas nitrous oxide is investigated as a function of geometry and process conditions. The effect of radiation was studied, which showed a decrease of the wire temperatures which in turn led to a higher nitrous oxide selectivity, however it did not imply a shift on the trend. Not only the temperature was found to drive the selectivity. Also, the surface composition showed an effect, and a sensitivity study was performed. The results showed that the selectivity is most sensitive to the surface composition of ammonia, which was found from the CFD calculations. Lastly, the effect of turbulence was studied in a single wire case. It was found that the results are not different from the laminar case results in terms of wire temperature and selectivity.

Preface

This thesis is an original work by Anton Fadic Eulefi. No part of this thesis has been previously published. All the results presented were developed by Anton Fadic Eulefi with the exception of the unreacting hot wire simulations presented in Chapter 6, which were performed by PhD student Ivan Cornejo Garcia.

Este trabajo se lo dedico a mi madre Pilar,

y al amor de mi vida Valerie

Acknowledgements

I spent 4 years of my life doing this work, and by no means I can say that I did not have any help from others, either directly or indirectly, to see this work become what it has. When doing this, there is always the danger to leave people out, and to them I excuse myself beforehand, saying that there is absolutely no bad intention.

First and foremost I'd like to acknowledge the academic and personal support of my PhD advisor, Dr. Robert E. Hayes. It was about 8 years ago, during the summer holidays in Chile and frigid cold of Edmonton, when we first met. I was invited to visit his research group as an intern during my undergrad studies at the University of Alberta, which was my first experience abroad on my own. There were countless discussions that guided me through all what the post graduate studies imply, which many times go beyond just academia. I would like to thank him for giving me the opportunity of pursuing my interests. Very early on I met his wife, Marina de Rementeria, with whom I developed a great relationship. The conversations we had really helped me get more adapted to the new culture, especially during the meetings we had at the pub formerly known as Devaney's, where Marina taught me how to teach. This proved to be very helpful later on for my duties as teaching assistant.

At the University of Alberta I had the chance to meet Dr. Rajab Litto, to whom I am very grateful for since he guided me through the bureaucracy that a newcomer has to go through. I am also very grateful of Dr. Joseph Mmbaga who introduced me to the world of computational fluid dynamics. With both I had very enjoyable discussions, especially I remember at lunch times. I would like to thank also the academic support of Martin Votsmeier, who provided thorough and constructive opinions that helped improve this work. I would also like to acknowledge my supervisory committee and the external reviewer for the constructive feedback given.

I also had the chance to meet the now Dr. Teng-Wang Nien, who at the time was a PhD student from prof. Hayes's group. We had very interesting conversations about academic topics, and I am very thankful for his great disposition to help me when I was taking my grad courses. I met other people, classmates and grad studies colleagues, with whom I developed a good relationship and became my friends, some of them are in no special order: Andres Sola, Ana Bianchini, Andre Bader, Sebastian Schulze, Artur Wiser, Markus Her-

rmann, Markus Klingenberger, Philip Roessger, Colin Saraka, Tarvo Kuss, Pamela Jahnsen, Eduardo Rodriguez, Dallas Cormier, Janina Graham, among many others. I am very grateful for the new opportunities that every friendship gave me, such as exploring playing sports as Volleyball, Squash, Tennis and Waterpolo, not to forget playing board games, which was a very fun part of it as well. I most definitely must mention my great friends from back home Tomas Orrego, Ignacio Aravena, Gonzalo Garin and Jorge Sanchez, who despite the distance, have taken steps to make me feel part of the group and take the time to meet with me every time I go back home. This is incredibly important to me. Muchas gracias cabros y les deseo lo mejor! Recently Ivan Cornejo has joined the group of prof. Hayes. We have had excellent academic and non academic discussions, aside from ping pong matches. I am very grateful for all the ideas that have come as a fruit of our conversations, which certainly made me improve part of my work. During the beginning of my PhD I met Dave and Julie Klikach, who have been very supportive of my academic endevour, and to whom I'd like to thank for making me feel accepted so quickly as part of their family.

Last but absolutely not least I left on purpose my two favourite people, who without a doubt made everything possible. These two people are my mother, Pilar Eulefi and my now wife, Valerie Klikach.

"Muchas gracias por todo mama, especialmente por la paciencia. Se que han pasado dias muy duros y estoy muy orgulloso de tu fortaleza. Estoy muy contento de como las cosas han evolucionado para mejor y ciertamente todos mis logros, sean cuales sean, siempre han tenido y van a tener tu impronta dentro de mi."

I met Valerie during my first year of the PhD. We had an instant great connection, and it changed my life. Now we are married. "I really appreciate your patience during these stressful times. It certainly has made it easier and way more enjoyable for me. I appreciate all the fun times we have had together, and that you can cheer me up so well if I am in a bad mood. I love you honey"

Contents

List of Figures

List of Tables

Chapter 1

Introduction

1.1 Motivation

There is very little disagreement in the scientific community about the existence of climate change and the man made cause of it, as reflected in the Kyoto protocol signed by 192 parties. Due to its possibly catastrophic consequences, there has been almost worldwide consensus on curbing the emissions of greenhouse gases (GHG), reflected especially through, as already mentioned, the Kyoto protocol on December 1997, and more recently the Paris accord, which was signed by 196 parties at the 21st Conference of the Parties of the United Nations Framework Convention on Climate Change (UNFCCC) in Paris, and it was adopted by consensus on December 12th, 2015. The intention of the agreement consists of responding to the global climate change threat, with the aim of keeping the temperature raise in the planet below 2 degrees Celsius above pre-industrial levels and even to pursue efforts to reduce said tempearature increase below 1.5 degrees Celsius. The agreement does not have a mechanism of enforceability, however most of the governments have taken action in order to meet its stated goals. Since its inception, however, the United States has decided to abandon it in June 2017. This is important, and hopefully only a transient decision of the current administration, considering that the United States contribute a significant amount of GHG measured by millions of CO_2 equivalent per year, at 13.7% for the year 2012, the second top emitter in the year 2012, only after China doubling them with 26.9%, and before India and Brazil with 6.5 % each, as can be seen in Figure 1.1.

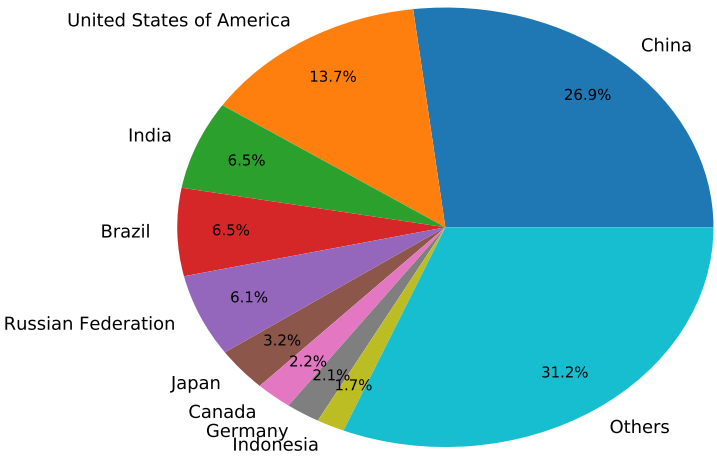

Figure 1.1: Greenhouse gases emissions measured in millions of equivalent CO_2 tons for the year 2012, in percentages. Data: Emission Database for Global Atmospheric Research (EDGAR)http://edgar.jrc.ec.europa.eu/

The trend of carbon emission has been upwards, with few moments in which it has been reduced as seen in Figure 1.1.

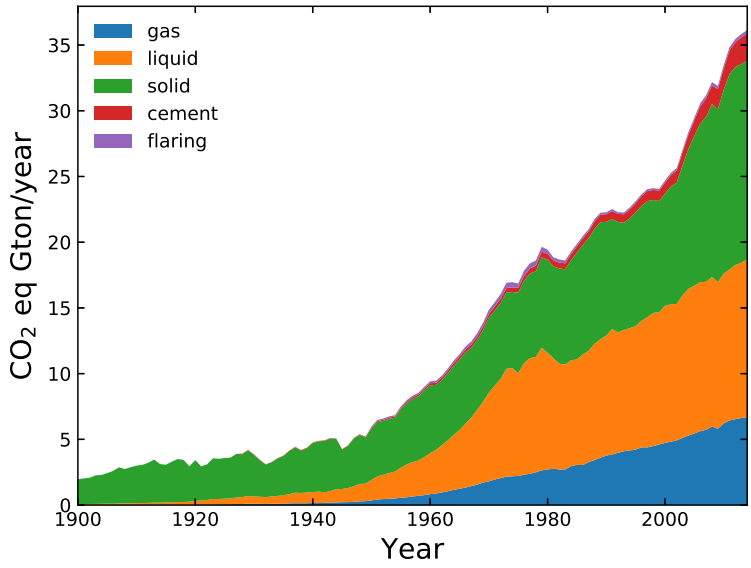

Figure 1.2: Total CO_2 emissions per year. Data: Carbon Dioxide Information Analysis Center, Oak Ridge National Laboratory, U.S. Department of Energy

The few moments in which the trend has declined have been when there are major world events, like World War I and II, the depression of 1921, and other moments of economic depression, as 1973, 1982, 2008.

Considering all of this, great effort is put in the scientific and industrial communities to analyse and minimize the emissions leading to the greenhouse effect. Since the industrial revolution, the economic output measured by the GDP in the world has increased rapidly. As more production relied on the use of machines, more fossil fuels were used. The relationship between the economic output is shown in Figure 1.3:

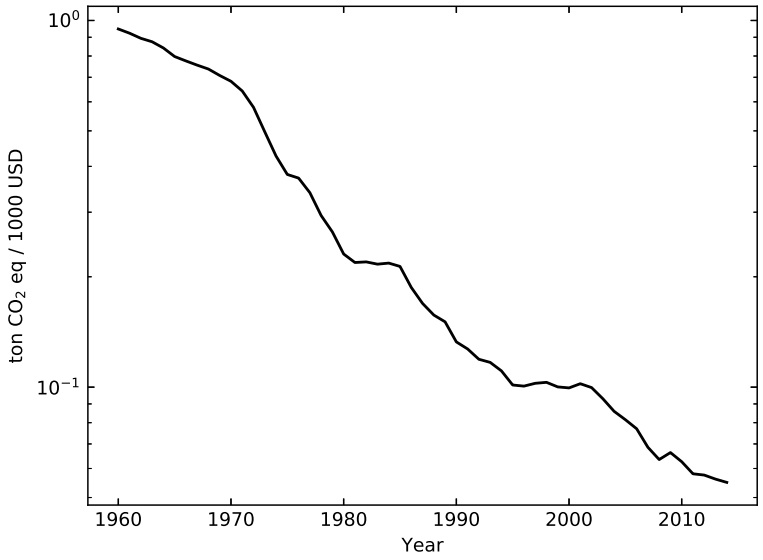

Figure 1.3: Total CO_2 emissions / world GDP USD$ per year. Data: Edgar database and World Bank

In Figure 1.1 it is possible to observe the positive relationship between world GDP and CO_2 emissions, however, when compared to the GDP as shown in Figure 1.3, the intensity of CO_2 emissions over the economic output is declining exponentially, which means that the output is increasing faster that the increase of the emissions. This can be explained partly by the expansion of the services sector worldwide, which is less emission intensive. Other possible explanations are the technological improvements which increase efficiency and decrease emissions, and the expansion of liquid and gas fuels, which generate less emissions. Considering that the Kyoto protocol and Paris agreement are relative recent, it is difficult to think of this reduction as a consequence of governmental emission reduction plans. Interestingly, coal is still the predominant fuel in year 2014, as seen from Figure 1.2, being the largest CO_2 contributor.

In this regard, there are several processes in industry that emit gases as a byproduct, and strong regulations exist to mitigate their effect. The most known of these can be the emission regulations of mobile sources, especially considering the case of diesel engines. In

this case what is sought is the efficient control of hydrocarbons resulting from combustion, nitrogen oxides produced by the internal combustion conditions of operation, carbon monoxide produced by incomplete combustion and finally particulate matter, using one or several devices that reduce pollution while at the same time minimizing any performance loss of the vehicle. The regulations are reviewed regularly with the objective to obtain better air quality, especially in bigger cities.

Similar regulations exist for stationary sources, which are related to the industrial sector. In this case the objective is the same of fulfill the emissions regulations with the constraint of not decrease the performance of the process significantly.

1.2 Greenhouse gases (GHG): Compounds and emitters

Several compounds have greenhouse gas effect. Each of them with different greenhouse warming potential due to its ability to retain radiant energy in the planet. In the province of Alberta, the emissions are regulated by the Climate Change and Emissions Management Act. In particular, in the Specified Gas Emitters regulation, the guidelines are based on tons of $CO2_e$, which is defined in article 1 part d as: *"CO_2e means the 100 year time horizon global warming potential of specified gas expressed in terms of equivalency to $CO2_2$ set out in column 3 of the Schedule"*. The Schedule in the regulation is presented in Table 1.1.

Table 1.1: Schedule gases according to GWP in climate change and emissions management act of the government of Alberta

Specified Gas	Chemical Formula	Global Warming Potential (100 year time horizon)
Carbon dioxide	CO_2	1
Methane	CH_4	25
Nitrous oxide	**N_2O**	**298**
HFC-23	CHF_3	14800
HFC-32	CH_2F_2	675
HFC-41	CH_3F	92
FHC-43-10mee	$C_5H_2F_10$	1640
HFC-125	C_2HF_5	3500
HFC-134	$C_2H_2F_4$	1100
HFC-134a	CH_2FCF_3	1430
HFC-152a	$C_2H_4F_2$	124
HFC-143	C_2H_3	353
HFC-143a	$C_2H_3F_3$	4470
HFC-227ea	C_3HF_7	3220
HFC-236fa	$C_3H_2F_6$	9810
HFC-245ca	$C_3H_3F_5$	693
Sulphur Hexafluoride	SF_6	22800
Perfluoromethane	CF_4	7390
Perfluoroethane	C_2F_6	12200
Perfluoropropane	C_3F_8	8830
Perfluorobutane	C_4F_10	8860
Perfluorocyclobutane	c-C_4F_8	10300
Perfluoropentane	C_5F_12	9160
Perfluorohexane	C_6F_14	9300

It is possible to see that many compounds exist that have higher GWP than CO_2. Methane (CH_4) is second in the list with GWP 25. This means that a gram of methane has an equivalent of 25 times the effect of a gram of CO_2 over a 100 years time span. Nitrous oxide, the focus of this thesis, is even more than ten times that, at 298. In terms of emissions, the largest share of the emissions in the United States in year 2016 is CO_2 with 81% of them. After it methane follows with only 10%, being followed by nitrous oxide with 6%. Finally, florinated gases contribute with 3%.

Therefore, nitrous oxide is the third top contributor to greenhouse gas emissions in the

United States. Considering the lack of reactivity of CO_2, major interest has been put in the scientific community to mitigate the emissions of methane. The control of emissions of nitrous oxide has lagged behind for several reasons, mainly due to the difficulty of its control, and the lag of regulation, as shown in Section 1.4. An important consideration therefore, is to show what are the main contributors of emissions of N_2O, so that their emissions can be curbed. Unlike methane, only 40% of the N_2O emissions come from human activities [19].

1.2.1 Alberta

According to data elaborated by the Government of Alberta in their Alberta Greenhouse Gas Reporting Program, from 2013 [50], the CO_2 emissions of year 2013 were of 125.8 Mton of CO_2 equivalent. The emissions were led by the energy sector accounting for 55.1% of the total emissions, followed by Electric Power Generation with 33.1%. Far behind are Chemical Manufacturing with 6.0% and Fertilizer Manufacturing with 3.3%.

In terms of N_2O production, it was of 1.13 Mton of CO_2 equivalent, account for 0.9 % of the emissions of the province. A similar picture is in the emissions of N_2O compared to the total CO_2 equivalent emissions. The largest emitter is the energy sector (48.8%), followed by electric power generation (23.3%). However, the in this case, it is followed by fertilizer manufacturing with 16.5% and followed by wood product manufacture with 7.4%. Therefore, overall the largest emitter in the provice of Alberta in terms of total CO_2 eq, and N_2O is the energy sector.

1.3 Pollutants that affect health

Although it is not the main topic of this work, it is important to mention the effect on health of other emissions tha can be produced from a nitric acid plant. Several compounds contribute to the pollution of air and depending on which ones are they, their impact can be from mild to serious on health. Certainly health is of paramount importance to lawmakers, although as explained in the previous section, interest exist also in gases that contribute to global warming.

In regards to health, the list of pollutants depends on the regulation of governments. A commonly used measure of pollution is called the air quality index. In Canada, this index is managed by the Ministry of the Environment, and it was formed in 2005. The index ranges from 1-10+, where 1-3 is deemed as low and above 10 is deemed as very high. Each of this indexes carry a certain message for at risk population and for the general population, advising against certain activities outdoors. The main inputs to the index are Nitrogen Dioxide (NO_2), ground level ozone (O_3) and fine particulate matter ($PM_{2.5}$), showing which are the most important pollutants regarding the health of the population. For the calculation of the index, a time average of three hours is used measuring the concentrations of the aforementioned compounds, according to the following formula:

$$AQHI = \frac{1000}{10.4}((e^{0.000537O_3} - 1) + (e^{0.000871NO_2} - 1) + (e^{0.000487PM_{2.5}} - 1)) \tag{1.1}$$

where O_3 and NO_2 are measured in parts per billion (ppb), and $PM_{2.5}$ is measured in micrograms per cubic metre (ug/m^3).

This is relevant, considering that in the Nitric Acid production, NO_2 is produced which must be controlled due to its effect on health. The description and effect of each of these compounds is discussed as follows:

Ground level ozone It is a colorless and irritating gas ocurring close to ground level. It is normally produced as a product of the reaction of Nitrogen oxides (NO_x) and volatile organic compounds (VOCs), which may come from natural sources or be related to human activities. According to the Government of Canada, about 95 % of NO_x come from human activity, mainly from the burning coal and gasoline, from homes, industries and power plants. As for VOCs, according to the same source, most of the human related ones come from gasoline combustion and distribution, upstream oil and gas production, residential wood combustion. A significant amount of VOCs is also emitted naturally from coniferous forests.

Nitrogen oxides (NO_x) This category comprises NO and NO_2. Note that it does not include N_2O due to its inert chemical nature. NO_2 of the two is the one of the most concern, since at high concentrations it produces inflammation of the airways. It also contributes to the formation of particulate matter and ozone (O_3). Its reaction with atmospheric water produces acid rain, and therefore it is of a high concern to control. The top contributors to nitrogen oxides are transportation, either diesel or gasoline. Other minor sources include marine transportation and electric utilities.

Fine particulate matter ($PM_{2.5}$) These particles have diameters of 2.5 μm or smaller, and can penetrate deep into the lungs, causing severe health effects in the population. They can be suspended in the air by construction sites, unpaved roads, fields, smokestacks or fires. The most important mechanism for its generation is due to reactions with ozone (O_3), volatile organic compounds (VOCs) and nitrogen oxides (NO_x) in internal combustion engines, power plants and industries.

1.4 Air pollution regulations

The most relevant pollution regulations regarding nitric acid plants is the one regarding NO_x. Indirectly other emissions are possible, for instance, fuels used for heating in the plant, but in general their impact is lower compared to one of NO_x. In this section the regulations pertaining the emissions of nitrogen oxides from nitric acid plants is presented.

1.4.1 United States

In the United States, pollution from Nitric Acid plants is covered under the Clean Air Act, which mandates the Environment Protection Agency to review or revise the New Source Performance Standards (NSPS) at least every 8 years. The one covering Nitric Acid Plants was initially promulgated in 1971, and has undergone review in 1979 and 1984. The most recent review which sets the requirements for facilities built or modified after 2011 was published in the Federal Register on August 14, 2012 (Federal Register Vol 77 No 157).

The most important limitation set by this law is the of this law is set in Article III point C, which establishes the following:

As proposed, and after consideration of the comments we received, we are reducing the NO_x emissions limit from 3.0 pounds of NO_x (expressed as NO_2) per ton of 100 percent of nitric acid (lb NO_x/ton acid) to 0.50 lb NO_x/ton acid as a 30 operating day based on the previous 30 operating days.

In the regulation N_2O is explicitly neglected, citing article III point B:

(...) also emit another nitrogen compound known as nitrous oxide (N_2O), which is considered a greenhouse gas (GHG). We are not taking final agency action with respect to a GHG emission standard in this action. (...)

The regulation states that new plants will be able to meet these new standards, citing examples of plants that use Non Selective Catalytic Reduction (NSCR), which emit in the range of 0.15-0.36 lb NO_x/ton acid.

It is important to note that no U.S. state has a law about carbon taxation, which would be relevant for the emission of N_2O. However, in some states there are active emissions trading programs, described in the following table:

Table 1.2: Emission Trade programs in the U.S.

Program	Agency	Type	Emissions	Source	Scope	Year
Acid Rain trading	U.S. EPA	CT	SO_2	Electricity generation	U.S	1990
RECLAIM	South coast AQM	CT	NO_x, SO_2	Stationary	L.A. Basin	1994
Averaging Banking and trading (ABT)	U.S. EPA	Av.	Various	Mobile	U.S.	1991
Cross-State Air Pollution rule	U.S. EPA	CT	NO_x, SO_2	Stationary	28 E. states	2017
Regional Greenhouse Gas Initiative (RGGI)	U.S. EPA	CT	CO_2	Electricity	9 N.E. states	2009
California GHG trading	U.S. EPA	CT	$CO_{2,eq}$	Stationary	Cal.	2013

Of all the programs shown in Table 1.2, the most relevant concerning N_2O is the California Greenhouse Gas trading program, which is one of the most active in the world only after the european emission trading program, and it comprises all stationary sources and all emissions according to their greenhouse warming potential. Therefore, depending on the location of the plant in the U.S., different rules apply.

1.4.2 Canada

Province of Alberta

Alberta is the largest emitter of GHG in Canada on an absolute basis. Alberta's GHG regulatory regime has been in place since July of 2007, being the oldest in North America. In the province of Alberta, air emissions are regulated by the Climate Change and Emissions Act, enacted January 1st, 2017. The Carbon Competitiveness incentive regulation is the current regulating body, and it is in effect since January 1st, 2018. Alberta requires any facility tha emits 100,000 tonnes or more of greenhouse gases a year to reduce their emissions intensity. Currently they must reduce it by 20%.

Companies can comply in four different ways:

1. Contribute to the Climate Change and Emissions Management Fund
2. Make improvements to their operations
3. Purchase Alberta-based carbon offset credits
4. Use emission performance credits

The price of carbon for facilities choosing to pay into the fund is $30 for every tonne over a facility's reduction target. Offsets are calculated in base of the EPA AP 42 compilation of air emission factors, which is dependent on the industry and facility type.

Province of British Columbia

This province has the objective of reduce by 33% the GHG levels of 2007 by 2020 and 80% less by 2050. The province has a carbon tax since 2012, set at $30 per tonne of CO_2 equivalent. The government is implementing the first stages of a cap and trade framework, currently being at the stage of reporting GHG emissions, however no legislation exist yet on cap on emissions or trading emissions credits.

In 2016 the Greenhouse Gas Industrial Reporting and Control Act came into force. This law is aligned with Alberta's pursuits to reduce GHG emissions. Industrial emissions emitting 10,0f00 tonnes of CO_2 equivalent mus report their GHG emissions. If the emissions surpass the 25,000 tonnes per year, this reports must be verified by an accredited third party. The GHG act also considers mechanisms for compliance. Offset units must be funded or earned credits, which can be traded. Funded means payments of a prescribed amount per tonne of GHG into a prescribed account. The carbon tax is expected to remain at $30, since the government dismissed a recommendation of a $10 per tonne per year increase.

Province of Saskatchewan

This province only accounts for 3% of the population in Canada, whereas their GHG emissions account for 10% of the national, making it the most intense emitter in terms per capita. Since 2010, the Management and Reduction of Greenhouse Gases and Adaption to Climate Change Act (Sask CC Act), requires emitters to reduce their annual GHG emissions collectively to meet the provincial emission target. The target is 20% below the emissions levels of 2006 by 2020. The regulated emitters are facilities that emit 50,000 tonnes or more of CO_2 equivalent per year. Any offset with respect to the targeted levels is required to pay a carbon compliance payment. However, the law has not been proclaimed yet to the date of this thesis, and therefore the law has not been put into effect.

Province of Ontario

After incentives to change gradually their electric power market away from GHG intense operations, the Climate Change Mitigiation and Low-carnon Economy Act was enacted in 2016, referred as the Ont CC Act. In the legislation, a cap and trade program is considered along with other measures to mitigate the emissions of GHG. The targets for reduction of the regulation is 15% reduction of GHG emissions compared to 1990 levels, 37% reduction for 2030 and 80% reduction by the end of 2050. Two other regulations were implemented: the Cap and Trade Program Regulation, which took effect in 2016, and the Quantification, Reporting and Verification of Greenhouse Gas Emissions Regulations, which took effect on January 1, 2017. The newly elected government led by the premier of Ontario has announced the decision to stop the Cap and Trade program existing in the province as of July 3rd. Not much information has been released to date of this work about further steps to enforce said decision. However, the federal government of Canada has announced a plan to enforce a CO_2 tax of 30 \$ / ton $CO_{2,e}$ on every province that does not have one, which might in fact establish a carbon tax in the province of Ontario.

Province of Quebec

One of the most prominent tools the government of Quebec has implemented for mitigating GHG emissions is the Climate Change Action Plan (CCAP 2020). The legislation sets a target of 20% reduction with respect of levels of 1990 by 2020. To achieve this goals, a Cap and Trade system has been established.

Under the Cap and Trade Regulation, a facility can emit only what is allowance permit. The allowances will decrease steadily each year between 2017-2020. The allowances that are not distributed, are set for auction. Also, facilities emitting under their allowance, obtain credit which can be sold. The Cap and Trade program is linked to the one in California since 2014. The regulations appliy for any emitter who exceeds 25,000 megatoones of CO_2 equivalent per year in a sector or activity listed uner the Cap and Trade Regulation (includes: electrical, electricity, mining and fosssil fuel distribution). Allowances are either

freely allocated, actioned off or sold by the Quebec Government.

1.4.3 Europe

In the European Union, the air quality legislation is based on several directives and decisions. Amongst the most relevant of these is the Directive 2008/50/EC known as the Air Quality Directive, which was entered into force on June 11, 2008. These directives are the norms for ambient air quality and cleaner air for Europe. Two important directives are the 2001/81/EC which sets upper limits for pollutants emitted for each member related to either acidification, eutrophication and ground-level ozone (SO_2, NO_x, VOC_s and ammonia). The measures to enforce these limits is left up to the member states.

Another relevant directive is 2010/75/EU on industrial emissions. It sets the principles and controls for installations based on the best available technologies (BAT), which are defined by a collaboration amongst the member states, industry and environmental organizations.

BAT for nitric acid plants is to reduce emissions during start-up and shutdown conditions. BAT is to reduce emissions of N_2O by applying a combination of the following techniques:

1. Optimizing the filtration of raw materials;
2. Optimizing the mixing of raw materials;
3. Optimizing the gas distribution over the catalyst;
4. Monitoring catalyst perfromance and adjusting the campaing length;
5. Optimization of the NH_3:air ratio;
6. Optimizing the pressure and temperature of the oxidation step;
7. N_2O decomposition by extension of the reactor chamber in new plants;
8. Catalytic N_2O decomposition in the reactor chamber combined NO_x and N_2O abatement in tail gases.

And the best available technologies (BAT) with its associated emissions levels (AEL) are for nitric acid plants:

New nitric acid plants:

1. N_2O emission level: 0.12 - 0.6 kg/t 100% HNO_3 (20-100 ppmv)

2. NO_x emission level, as NO_2: 5-75 ppmv

For existing nitric acid plants:

1. N_2O emission level: 0.12 - 1.85 kg/t 100% HNO_3 (20-300 ppmv)

2. NO_x emission level as NO2: 5 - 90 ppmv (up to 150 ppmv where safety aspects due to deposits of ammonion nitrate restric the effect of SCR or with addition of H_2O_2 instead of applying SCR)

Comment: For a typical mid pressure nitric acid plant with uncontrolled N_2O, the emissions are of the order or 7 kg/ton NH_3. This means that the regulation requires a 74 - 98 % control of the emissions of existing plants, and for new plants the required control is more stringent, in the range of 91.4% to 98%.

1.5 Organization of this work

The organization of this work is as follows. In Chapter Two, the process of nitric acid production is presented. The main reactions showing the path of ammonia to become nitric acid is exposed, along with the parallel reactions that show the production of undesired products. In the second part of that chapter, a discussion of the available technologies used to control these emissions is presented. In Chapter 3 relevant theoretical background is exposed, which covers from thermodynamics to computational fluid dynamics and turbulence modelling. In chapter 4 a discussion of acceleration techniques for detailed mechanism speed up is presented. This covers the use of lookup tables and neural networks, which is applied for ammonia oxidation mechanism plus a steam reforming mechanism for comparison purposes. In chapter 5 the ammonia oxidation process is presented in the context of

a single wire. The simulation is done coupling the transport phenomena with the detailed mechanism for ammonia oxidation, which allows to show the wire temperature, the surface concentrations and other variables that are difficult to measure under experimental or industrial conditions. In chapter 6, a simulation on a small scale wire is done using LES to study if the turbulence plays a role in the conversion and selectivity. Chapter 7 is the conclusions and future work.

Chapter 2

Nitric Acid, production and air pollution control

2.1 Nitric Acid

Nitric Acid, with the chemical formula HNO_3, is a strong acid that occurs in nature only in the form of nitrate salts. Before the industrial process was developed, it was obtained from sodium nitrate (soda saltpeter, Chile saltpeter). Once it is produced it can be stored as such in special tanks, or it can be treated with ammonia to form ammonium nitrate (NH_4NO_3) due to its easier manipulation. Its uses include mostly as a high nitrogen fertilizer ($\approx$ 80%) as either ammonium nitrate or nitrophosphate. Ammonium nitrate can be further treated as calcium nitrate, calcium ammonium nitrate, urea ammonium nitrate solution and ammonium sulphate nitrate depending on the specific needs as fertilizer. Nitric acid finds about 15% of its consumption as non fertilizer, mainly as ammonium nitrate for non fertilizing purpose, or chemicals suchs as caprolactam, adipic acid, dinitrotoluene, and nitrobenzene [33].

Nitric acid is an important chemical, being amongst the top 15 chemicals produced in the world [34], with a yearly production of about 55 million tonnes in 2006 [26].

2.1.1 Properties of Nitric Acid

Nitric acid has molecular weight of 63.013, and is miscible in water in all proportions. It forms an azeotrope at a concentration of 69.2 % w/w. The azeotropic mixture boils at 121.8 deg C, whereas pure anhydrous nitric acid boils at 83-87 deg C. Nitric acid decomposes with heat as:

$$4\,\mathrm{NH_3} \longrightarrow 2\,\mathrm{H_2O} + 4\,\mathrm{NO_2} + \mathrm{O_2}\ \Delta H_r^0 = -57\ \mathrm{kJ/mol}$$

At atmospheric pressure, nitric acid has a freezing point of -41.59 deg C, and a boiling point of 82.6 deg C. The density at 20 degC is of 1512.8 kg/m^3. Concentrated nitric acid is a potent oxidizer, which can attack steel. Therefore, alloyed steel materials are used in the nitric acid equipment process [67].

2.2 Nitric Acid Production

The modern route of nitric acid production is based on the Ostwald process of ammonia oxidation [52] over a metal that acts as catalyst. This technology has passed the test of time, since it was developed in the early 1900s, and it is used nowadays with only minor modifications. The Ostwald process begins with the oxidation of ammmonia over a Pt catalyst to produce nitrogen monoxide NO, as:

$$4\,\mathrm{NH_3} + 5\,\mathrm{O_2} \longrightarrow 4\,\mathrm{NO} + 6\,\mathrm{H_2O}\ \Delta H_r^0 = -227\ \mathrm{kJ/mol}$$

which is highly exothermic, with a heat of reaction of -227 kJ per mol of ammonia. This in turn creates a large temperature difference, which affects the transport properties, density and kinetics of the reaction on the surface. With the use of catalyst, high yields can be obtained from 94-98%, depending on the operating conditions and catalyst used.

However, other reactions take place concurrently with the ammonia oxidation that form nitrogen and that form nitrous oxide, with stochiometries:

$$4\,\mathrm{NH_3} + 3\,\mathrm{O_2} \longrightarrow 2\,\mathrm{N_2} + 6\,\mathrm{H_2O}\ \Delta H_r^0 = -315\ \mathrm{kJ/mol}$$

$$4\,NH_3 + 4\,O_2 \longrightarrow 2\,N_2O + 6\,H_2O\ \Delta H_r^0 = -368\ \text{kJ/mol}$$

these undesired reactions reduce the yield of NO and therefore reduce the efficiency of the process. Moreover, N_2O is a strong greenhouse gas, and depending on the location of the plant, penalties must be paid for its emission.

The nitrogen oxide NO is then further oxidized with the unreacted oxygen and oxygen fed in the absorption tower as:

$$NO + 0.5\,O_2 \longrightarrow NO_2\ \Delta H_r^0 = -57\ \text{kJ/mol}$$

NO_2 reacts to form as N_2O_4:

$$2\,NO_2 \longleftrightarrow N_2O_4$$

And the NO_2 reacts with water to produce nitric acid as:

$$NO_2 + H_2O \longrightarrow HNO_3\ \Delta H_r^0 = -315 kJ/mol$$

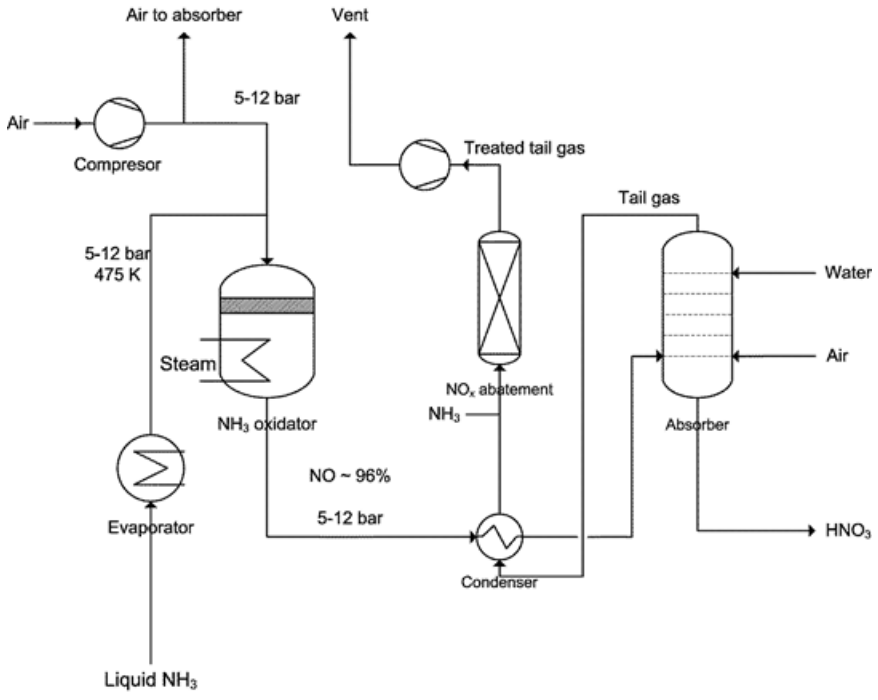

Figure 2.1: Simplified nitric acid production process

The simplified process is illustrated in Figure 2.1. As can be noted, the feed consists of air and ammonia. Ammonia can be either bought from a third party or it can be produced on site. This depends on the scope of the factory and on market variables that companies use for their strategic planning. If the ammonia is bought, then the investment for the nitric acid plant is lower compared to ammonia produced on site. In this case, an ammonia synthesis plant is required and a hydrogen source, which would be usually made on site by methane steam reforming. It is important to mention this considering that in matters of regulation the whole cycle is relevant. It is beyond the scope of this work to describe the ammonia synthesis plant or methane reforming plants. An excellent review in detail of these processes can be found in [1].

2.2.1 High concentration nitric acid

Due to the formation of the azeotrope, the maximum concentration of nitric acid is of 69.2% w/w. Some applications need nitric acid at higher concentrations. Two methods are used to produce concentrated nitric acid:

Direct processes

In these methods the water generated from the ammonia combustion is removed by rapid cooling so the nitric acid can be produced in two ways:

1. The NO_2 can be separated in liquid form in an absorption process in concentrated nitric acid and then led to a reactor where it is reacted with oxygen and water, under pressure to yield concentrated acid.

2. NO_2 can be reacted with azeotropic acid to form concentrated acid, which can be then distilled into weak acid and concentrated acid.

Indirect processes

Concentration is based on extractive distillation and rectification with sulfuric acid or magnesium nitrate.

In the United States, of the 40 nitric acid plants in operation as of 2010, only one produces concentrated nitric acid, based on the Uhde process which is a direct method. This plant is El Dorado Nitrogen, operated by LSB industries and located in El Dorado, Arkansas.

2.3 Operating conditions

The ammonia oxidation step in the nitric acid process is key regarding the output, due to its location upstream, its effect of pressure and due to its effect of feed composition on the gaseous composition that is fed into the absorption tower. Other important considerations is the fact that the mixture of ammonia in air can reach explosive limits, and therefore the operation must guarantee the functioning below said threshold. Another key variable is the feed mass flow rate, which has an effect on the conversion, composition and temperature, aside from modifying the explosive limit, and so it is the effect of the operating pressure. Finally, the most used catalyst of Pt or Pt/Rh are known to be very sensitive to the catalyst temperature, due to its effect on the Pt losses. Each of these considerations is explained in more detailed below.

2.3.1 Pressure and temperature

Most modern plants operate at medium pressure (4-8 bar) high pressure (8-14 bar), or dual pressure (medium pressure oxidation and high pressure absorption). Atmospheric pressure plants are no longer in use due to its inefficiencies, such as larger equipment requirement and larger operating costs. The development of stainless, austenitic chromium-nickel steels led to the use of non atmospheric pressure plants. The use of higher pressures, however, reduces the yield of NO [29]. The use of dual pressure plants was led by developments in the construction of large NO resistant turbo-compressors and turbo-expanders. This allowed to have a medium pressure operation in the ammonia oxidation step, and then a large pressure use in the absorption step, increasing its efficiency.

The temperature, in turn, is set regarding the desired wire temperature. This variable

has a considerable effect on the selectivity to N_2O and on the stability of the Pt/Rh catalyst. Higher temperature increase the selectivity to NO, however, they also increase the catalyst losses. Therefore, a tradeoff exist between conversion and catalyst stability, and for economic reasons the range of operation of the wires is usually of the range of 850 - 900 degrees Celsius. Since the reaction is extremely fast, feed temperatures do not affect the conversion noticeably.

2.3.2 Explosive limit, composition and mass flow rate

Typical operations of ammonia oxidation processes occur close to the explosive limit. This variable in turn depends also on the pressure and the speed of the flow. The explosive limit for atmospheric conditions can be found in Table 2.1:

Table 2.1: Explosive limits of ammonia-air mixtures at atmospheric pressure

flow velocity m/s	LEL %	UEL %
0	15.5	27.5
3	28	38
5-8	30	40
12	32	37
14	none	none

where LEL refers to Lower Explosive Limit and UEL refers to upper explosive limits in volume fractions. As can be seen from the table, higher flow velocities increase the LEL and the UEL, therefore this is preferred in terms of a safer operation. Operations at higher pressures decrease both the LEL and UEL. In a typical mid pressure plant, operating at 5 bar, the flow velocity is of the range of 0.75 - 3 m/s and the LEL under this circumstances is of about 11 % [29]. A safety margin must be considered, giving a typical ammonia mole fraction in the feed of 10%. Considering the risk hazard, the ammonia composition is checked continuously to avoid reaching the explosive limit with transient variations of the feed. Since measuring the feed composition on line is not practical, the method to measure the composition is based on the temperature of the catalyst gauze. The tempererature rise

is related to the composition, and the Equation 2.1 is usually used [29]:

$$T_{cat} = T_{feed} + x_{\mathrm{NH_3}} \cdot 6800 \tag{2.1}$$

where all the temperatures are in degrees Celsius. Therefore, with this method it is possible to estimate the composition of the feed, and verify the safe operation of the reactor.

A stream of 10% of ammonia of an idealized mixture of air of only N_2 and O_2 gives a composition of oxygen of 18.9%, giving therefore a ratio $O_2\ /NH_3 = 1.89$. However, the stoichiometry ratio of O_2/NH_3 is 1.25. Therefore the operation occurs in excess of oxygen. The benefit of this, aside from the safety, is an increased yield of NO [29].

Finally, the massflow rate is obtained by setting density of the feed, which after fixing the composition is determined by the temperature and the pressure, and the area of the oxidation which is determined by the plant design. An important constraint to speed is its positive correlation with Pt losses, which sets a ceiling to the maximum economically feasible speed.

2.3.3 Catalyst, deactivation, and losses

The catalyst in ammonia oxidation is a key component of the process. The equilibrium of the reaction in gas phase is dominated by the production of N_2. Therefore, metal catalyst have been used. The original process proposed by Ostwald used Pt wires. This catalyst has not been able to be replaced by cheaper materials at the moment [29].

As shown in Figure 5 of [56], all the catalyst for ammonia oxidation are some kind of woven or knitted metal wires. It was discovered after the original proposal of Ostwald that the addition of Rh to a Pt catalyst can improve the performance of it by increasing its lifetime, and increasing the yield to NO. The maximum benefit is obtained after the addition of 10% of Rh, and after that a flat catalyst loss is found. Therefore, most catalyst for ammonia oxidation are of Pt/Rh 90/10 %.

This catalyst is very sensitive to impurities. NO yields are reduced if impurities are found of metals such as gold, manganese, nickel, uranium, copper, beryllium, calcium,

barium and aluminium. In addition to these, other impurities can reduce the mechanical strength of the catalyst [29]. Therefore, the catalyst are provided with a purity of Pt/Rh of at least 99.9%.

The catalyst structure is usually regarded as Pt/Rh wire diameter and screen size. Typical wire diameters are 0.06mm and 0.076 mm and typical screen sizes are of 1024 mesh/cm^2 [67]. This means that the for a square arrangement, there are 3.2 mesh/mm or 0.3125 mesh/mm. Discounting the wire diameter, the separations range from 0.2365 mm for a diameter of 0.076 to 0.2525 for a diameter of 0.06. This means that the typical wire to wire separation is of 3.11D to 4.21D for diameters of 0.076mm and 0.06mm respectively.

Regarding catalyst deactivation, the most common mechanism of deactivation is by the evaporation losses. Pt has a very low vapor pressure even at higher temperatures [67]. However, when PtO_2 is formed, especially when the temperatures increase, it vaporizes and reduce the activity by reducing the exposed area and the mechanical strength of the mesh. Since Pt is an expensive precious metal, it accounts for large part of the costs of a plant [67]. Therefore, it is common to install recuperation devices downstream the oxidation step. These recuperation catalyst are typically made of Pd/Au 80/20 with gauzes of 100-1350 ms/cm^2 and wire diameters ranging from 0.2-0.06 mm [67]. Some Pd losses occur, of about 0.4g per gram of capture Pt [29]. Considering the relative low cost of Pd, this is a very effective method to reduce costs of the operation by recovering the evaporated Pt.

For completeness, other catalyst metals have been used in the ammonia oxidation step. More remarkably is what has been called brown oxide catalyst (90% Fe_2O_3, 5% Mn_2O_3 and 5% Bi_2O_3) which was used by Germany during the First World War due to scarcity of Pt. This catalyst had to operate at lower ammonia mole fraction of 7.1 to 7.3 % and with lower yields to NO of 92 to 94 % [29].

2.3.4 Absorption step

The absorption step is a relatively complicated step in the process. An unusual aspect of it is that one of the important reactions of formation of NO_2 from NO and O_2 has

a negative apparent activation energy. Therefore, downstream of the highly exothermic ammonia oxidation, the gases have to be cooled down. To operate the absorption more efficiently, the pressure can be increased.

In the gas phase, a mixture of different compounds exist (NO, NO_2, N_2O_3, N_2O_4). The main reaction to produce nitric acid is the following:

$$N_2O_4 + H_2O \longrightarrow HNO_3 + HNO_2$$

Further reactions of HNO_2 are:

$$3\,HNO_2 \longrightarrow HNO_3 + H_2O + 2\,NO$$

Forming more NO that can be further oxidized to NO_2, which exists in equilibrium with N_2O_4.

2.4 Air pollution control

As can be seen in the regulation section, the emissions of NO_x have been regulated strongly since the seventies considering their effect on acid rain and public health. Therefore, the technology for controlling the emissions of nitrogen oxides is rather mature. These technologies can control the emissions of NO and NO_2. Since NO and NO_2 are desired products in the absorption tower, the control occurs downstream, as seen in Figure 2.1. The selection of technology depends on the cost and the desired reduction level, which depends on the legislation that the plant is covered in. The technologies than can control the emissions of NO_x are presented in the next section.

2.4.1 Control of NO_x

Catalytic Reduction (SCR and NSCR)

This methods use a reducing agent, typically methane or ammonia, to reduce NO and NO_2 to N_2 and H_2O. The choice of catalyst affects the selectivity of the measure. For

non selective catalytic reduction, the usual catalyst are platinum, vanadium pentoxide, iron oxide or titanium. The required amount of the fuel, either NH_3 or CH_4 depends on the stoichiomestry and usually some excess is added. This process, however, is not selective, producing some by products such as carbon moxide or hydrogen cyanide.

Scrubbing

The idea of scrubbing is to promote the absorption of the compound with a fluid. In the nitric acid process, this is the same desired objective. Then, technologies for improvement of fugitive emissions of NO_x generally consider improvements in the absorption step.

2.4.2 Control of N_2O

Typical values for emissions of N_2O in uncontrolled plants is of the order of 7 kg/tonne of HNO_3 produced (100%) for medium pressure plants (4-8 bar) [69]. Considering that the worldwide annual production of HNO_3 is of about 55 million ton [26] and the GWP of N_2O of 298, then the worldwide emissions are of 115 million ton CO_2 equivalent if the plants are uncontrolled for N_2O. Considering the worldwide emissions, the nitrous oxide production from industrial and chemical plants represents 0.35% of the worldwide emissions. For comparison purposes, the GHG emissions in Europe in 2016 was 22% lower than the emissions in 1990, with a absolute reduction of 279 million ton of CO_2 equivalent. Therefore, controlling the emissions of N_2O is a substantial way of reducing the GHG gases emissions. In this work it will be common to refer to the N_2O selectivity, defined as the ratio of the number of moles created of N_2O in the ammonia oxidation process, versus the number of moles of ammonia reacted, all in terms of their stoichiometric proportions. The definition of the selectivity according to the stoichiometry:

$$4\,NH_3 + 4\,O_2 \longleftrightarrow 6\,H_2O + 2\,N_2O$$

Using this definition, 7 kg / ton HNO_3 100% can be referred in terms of selectivity as:

$$sel = 2\frac{N_{N_2O}}{N_{NH_3}} \tag{2.2}$$

Therefore, using this definition of selectivity, the selectivity of the process can be written as:

$$sel = 7\frac{\mathrm{kg}_{N_2O}}{\mathrm{t}_{HNO_3}}\frac{63\mathrm{g/mol}_{HNO_3}}{17\mathrm{g/mol}_{NH_3}}\frac{1\mathrm{t}}{1000\mathrm{kg}}\frac{17\mathrm{g/mol}_{NH_3}}{44\mathrm{g/mol}_{N_2O}}\cdot 2 = 2.0\% \tag{2.3}$$

Usually the control technologies for N_2O are defined in terms of its location in the process. Three alternatives are devised [19]:

Primary control

Refers to modifications of the catalyst itself to lower the selectivity to N_2O or to the operating conditions of the reactor. This can be for example, modifying the shape of the gauze, or changing the organization of the Pt wires. The study of the N_2O production on Pt wires is the main topic of this thesis. The effect of the operating conditions is also included in this work.

An illustration of the catalyst gauze similar to the one used in this study can be found in [56] Figure 5.

Secondary control

Refers to modifications that occur immediately downstream the oxidation step, within the reactor, so that the fluid is still at high temperatures. It is placed usually downstream of the Pt recovery catalyst, when the reaction gases are still at high temperatures, which is necessary for the reaction to occur. This technology has been demonstrated in practice, with effectiveness of 70-90% of removal of N_2O and operating costs of \$0.12 - \$0.97 per CO_2 equivalent removed.

Two secondary controls are common. One is the extended chamber concept developed

by Norsk-Hydro. Here, gas phase reactions occur in an extended reactor to increase the residence times to up to 2s, with reported reduction levels of up to 70%, with increase of capital cost but no increase of operational costs [56]. This method is feasible for new plants but it is difficult or impossible to be used in existing plant due to space considerations.

Tertiary control

This control occurs downstream the absorption tower and it is usually used when the retrofitting of the plant cannot be done for space or process reasons. This technology has been demonstrated in practice and the emission reduction of N_2O is higher than 80%. Its capital costs per ton of CO_2 equivalent goes from \$2.18 - \$3.55, and its operating costs go from \$0.14 - \$1.91 per ton of CO_2 equivalent removed. The largest operating costs of this technology are a direct consequence of the placement downstream the absorption tower, and therefore a heating step has to be considered additionally to use this technology.

A fourth method is considered by [56], called quarternary control. This method is similar to tertiary control, but occurs downstream the expansion turbine, at atmospheric pressure.

Chapter 3

Theoretical background

3.1 Thermodynamics

3.1.1 Single component

The fundamental relationships of thermodynamics are important laws that are used explicitly or implicitly in this work. The first law of thermodynamics, called the conservation of energy, is stated as follows:

$$dU = \delta Q - \delta W \tag{3.1}$$

The quantities δQ and δW can be expressed in terms of intensive variables for a reversible process as [53]:

$$\delta Q_{rev} = Tds \tag{3.2}$$

For reversible pressure volume work done by the system on its surroundings, the term δW can be written as [53]:

$$\delta W_{rev} = Pdv \tag{3.3}$$

Obtaining:

$$dU = Tds - Pdv \tag{3.4}$$

Which is an exact differential, and hence a function of the state in terms of U, S and V. This relationship is therefore not exclusive for a reversible process [53]. Defining the following variable, called enthalpy:

$$h = U + PV \tag{3.5}$$

Taking its total differential:

$$dh = dU + Pdv + vdP \tag{3.6}$$

and substituting it into the energy balance equation:

$$dh = Tds + vdP \tag{3.7}$$

According to the Gibbs phase rule, the number of independent intensive variables needed to describe the thermodynamic state of a system are two for a single phase, single component system. Therefore, the enthalpy can be written as function of temperature and pressure, as follows:

$$dh = \frac{\partial H}{\partial T}|_P dT + \frac{\partial H}{\partial P}|_T dP \tag{3.8}$$

The enthalpy variation with respect to the temperature at constant pressure is defined as the heat capacity at constant pressure, and it is defined as follows:

$$\frac{\partial H}{\partial T}|_P = C_p(T) \tag{3.9}$$

Which is a function of temperature. For an ideal gas, the dependency on the pressure

of the enthalpy can be shown to be zero, and therefore, the enthalpy variation of an ideal gas is:

$$dh = \frac{\partial H}{\partial T}|_P dT = C_p(T)dT \tag{3.10}$$

The quantity C_p is commonly tabulated as polynomials, which are available for many species. These polynomials are normally a forth degree polynomial in temperature, and they are measured at a reference temperature. The C_p is defined as:

$$C_p(T) = \sum_{i=0}^{n} a_i T^i \tag{3.11}$$

Hence, the enthalpy change due to a variation in temperature can be computed as:

$$\Delta H = \int_{T_{ref}}^{T} C_p(T)dT = \sum_{i=0}^{n} a_i \frac{(T^{i+1} - T_{ref}^{i+1})}{i+1} \tag{3.12}$$

Finally, from Equation 3.7, it is possible to determine the entropy change from an isothermal process. Since $dT = 0$, then:

$$Tds = -vdP \tag{3.13}$$

Considering the ideal gas equation:

$$Pv = RT \tag{3.14}$$

then Equation 3.13 becomes:

$$ds = -\frac{R}{P}dP \tag{3.15}$$

and integrating:

$$\Delta s = R \ln \frac{P_1}{P_2} = -R \ln \frac{P_2}{P_1} \tag{3.16}$$

This result will prove useful to calculate thermodynamical equilibrium of mixtures. The entropy dependency at constant pressure as a function of the temperature, can be computed from Equation 3.7:

$$\frac{\partial s}{\partial T}|_P = \frac{C_p(T)}{T} \tag{3.17}$$

3.1.2 Multiple species

In the case of a mixture consisting of multiple species, the are more variables which contribute to the change of enthalpy. Enthalpy is never measured absolutely, and it is always required as a change with respect to a reference, such as was shown in the previous section where a reference for the temperature was set. However, in the case of changes of composition in the mixture, a reference with respect to a compound must be set. This is the role of the Enthalpy of formation ΔH_f^0, which is set to 0 for a pure compound in its standard form. Therefore, the enthalpy of a substance i can be determined as:

$$H(T)_i = \Delta H_{f,i}^0 + \int_{T_{ref}}^{T} C_p(T)dT \tag{3.18}$$

Other effects such as phase changes, or dilution, among others can affect the enthalpy which are not covered here.

3.1.3 Chemical equilibrium

An important concept in reaction engineering is the one of chemical equilibrium, which has the ability of limiting the extent of a reaction. The following quantity is defined, called the Gibbs free energy:

$$G = H - TS \tag{3.19}$$

The Gibbs free energy is also a function of state, which can be expressed as a function of temperature and pressure. Unlike a pure compound, for a mixture the Gibbs function is

a function of the temperature, pressure and the composition, so that its differential can be computed as:

$$(dG)_T = -Tds_T \tag{3.20}$$

Equation 3.16 where a result to calculate the change of entropy as a function of pressure for an isothermal process was found, can be combined with equation 3.20:

$$(\Delta G)_T = -RT \ln \frac{P_2}{P_1} \tag{3.21}$$

It states that the system will evolve spontaneously in the direction of minimum free energy $dG < 0$. Therefore, the equilibrium is obtained at the limit, where $dG = 0$. For a typical ideal gas reacting system, let us consider the following reaction:

$$\nu_a \mathrm{A} + \nu_b \mathrm{B} \rightleftharpoons \nu_c \mathrm{C} + \nu_D \mathrm{D}$$

The Gibbs function can be expressed as a Standard Gibbs energy plus the additional term due to the change in pressure. Considering a reference state of pressure equals to 1, in arbitrary consistent units, typically atmospheres or bars, then:

$$g_i(T, P)_i = g^*(T) + RT \ln P_i \tag{3.22}$$

Calculating the associated change in Gibbs free energy for the associated reaction:

$$\nu_C[g_C^* + RT \ln P_C] + \nu_D[g_D^* + RT \ln P_D] - \nu_A[g_A^* + RT \ln P_A] - \nu_B[g_B^* + RT \ln P_B] = 0 \tag{3.23}$$

Which shows that the only way to obtain the equality at a given pressure and temperature, consists of changing the composition of the mixture. It is convenient to define the Standard State Gibbs function change due to the reaction, as:

$$\Delta G^*(T) = \nu_C g_C^* + \nu_D g_D^* - \nu_A g_A^* - \nu_B g_B^* \tag{3.24}$$

and substituting into Equation 3.23:

$$\Delta G^*(T) = -RT \ln \frac{P_C^{\nu_C} P_D^{\nu_D}}{P_A^{\nu_A} P_B^{\nu_B}} = -RT \ln K_p \tag{3.25}$$

Or

$$K_p = \exp -\frac{\Delta G^*(T)}{RT} \tag{3.26}$$

The equilibrium constant shows what is the expected state of a system at its equilibrium, but it does not say anything about the kinetics, or how fast the equilibrium is achieved. The equilibrium may be achieved very quickly or it can take years. The subindex p refers that the equilibrium constant K_p is calculated in terms of partial pressures.

3.2 Chemical kinetics

The effect of the temperature in the chemical kinetics is explained by the Arrhenius law. The reaction kinetics can be based on simple collision theory, which states that when two molecules with sufficient energy collide and react. Arrhenius then proposed that the rate constant as function of the temperature follows :

$$k = A \exp -\frac{E_a}{RT} \tag{3.27}$$

Which has been verified empirically. A physical interpretation of the activation energy E_a corresponds to the minimum energy available in a system with reactants to obtain a chemical reaction. Another Arrhenius type law, with a temperature dependent preexponential factor β is:

$$k = AT^{\beta} \exp -\frac{E_a}{RT} \tag{3.28}$$

3.2.1 Law of mass action

The effect of the quantity of material in the reaction rate is explained by the law of mass action. It was proposed by Guldberg and Waage in 1867 [21] and it states that the rate of an elementary step is proportional to the concentration of the reactants powered to their stoichiometric coefficients, as:

$$r = k \prod_i c^{|\nu_i|} \tag{3.29}$$

where ν_i corresponds to the stoichiometric coefficients of the forward reaction. An elementary step is defined as

> *A reaction for which no reaction intermediates have been detected or need to be postulated in order to describe the chemical reaction on a molecular scale. An elementary reaction is assumed to occur in a single step and to pass through a single transition state.* [46]

Examples of elementary steps are: unimolecular or bimolecular. According to the collision theory, a termolecular reaction has a neglegible probability of occurring.

A reversible reaction rate can be written as:

$$r = k_f \prod_i c^{|\nu_i|} - k_b \prod_j c^{|\nu_j|} \tag{3.30}$$

where i runs for the reactants, and j runs for the products. Consider that the reaction is in equilibrium, hence, the net rate is 0. Then, at equilibrium:

$$\frac{k_f}{k_b} = \frac{\prod_j c^{|\nu_j|}}{\prod_i c^{|\nu_i|}} = K_c \tag{3.31}$$

where K_c is the equilibrium constant based on concentrations. These concentrations can be transformed to partial pressures for an ideal gas by using its equation of state.

Let us define the factor relating the equilibrium constant based on the partial pressures

and concentrations as $F_{C/P}$. Therefore, the following must hold for a reversible reaction:

$$K_c F_{C/P} = K_p = \exp -\frac{\Delta G^*(T)}{RT} \tag{3.32}$$

equation that defines thermodynamical consistency, which guarantees the correct thermodynamical behaviour of the kinetics parameters of the forward and backward kinetics parameters. The consequence of this result is that one degree of freedom is lost for every reversible reaction proposed in the chemical mechanism.

3.3 Heterogeneous Catalysis

More than 80% of reactions of industrial relevance are catalytic [1]. They are of economic importance due to their property of speeding up chemical reactions by proving alternative paths of lower activation energy. In heterogeneous catalysis, these paths include the formation of intermediaries on the surface of a solid catalyst, which react with either another intermediary or with a gas phase species. An extensive discussion of heterogeneous catalysis can be found in [29, 1]. More relevant for this work is the calculation of the rate. Generally speaking, the reaction rates for an elementary step is given by [14]:

$$r_i = A_i T_i^{\beta} \exp(\frac{-E_{a,i}}{RT}) \prod_i c^{|\nu_i|} \prod_i \Theta_i^{|\nu_i|} \tag{3.33}$$

where Θ_i refers to the surface coverage of species i. A is known as the preexponential factor, E_a is the activation energy, c_i is the concentration of the gas species i. Many reactions can be modelled with this formula. However, other reactions have the complexity of having an activation energy that is surface coverage dependent [14]:

$$r_i = A_i T^{\beta_i} \exp(-\frac{E_{a,i}}{RT}) \prod_i \exp(\frac{\epsilon_{i,k}\Theta_k}{RT}) c^{|\nu_i|} \prod_i \Theta_i^{|\nu_i|} \tag{3.34}$$

In this case, the parameter ϵ modifies the energy of activation depending on the surface

coverage. As a reminder, the surface coverage is defined as:

$$\Theta_i = \frac{C_i}{\Gamma} \tag{3.35}$$

where C_i is the surface concentration of species i and Γ is the surface site density, which is typically expressed in units of mol/m^2

3.4 Computational fluid dynamics

The basis of this work lies in the combination of thermodynamics, fluid dynamics, transport phenomena and chemistry to simulate the reaction process, specifically in the ammonia oxidation process in the nitric acid production. The principles of the aforementioned sciences are used in this case, such as conservation of mass, conservation of momentum, conservation of energy and conservation of chemical species. In this section a general overview of the equations and their methods of solution is presented.

3.4.1 Conservation equations

In engineering many principles of conservation are used to simulate either analytically or numerically the states of a system. A good review of conservation equations can be found in [5]. The boundary conditions, necessary to solve the conservation problems are specific to each problem to be solved and are presented where needed. The governing equations are:

Overall mass conservation For transient flow, the overall mass conservation of the fluid phase is [2]:

$$\frac{\partial \rho}{\partial t} + \nabla \cdot (\rho \vec{u}) = 0 \tag{3.36}$$

where ρ is the mixture density, and it is calculated from ideal gas law, and $\vec{u}$ is the velocity field.

Conservation of momentum Laminar flow, Newtonian fluid and ideal gas behaviour are assumed. This equation is valid for turbulente flows as well, but in general if turbulence is modelled it affects the structure of the momentum equations. Thus, the conservation of momentum can be written as [2]:

$$\frac{\partial(\rho\vec{u})}{\partial t} + \nabla\cdot(\rho\vec{u}\,\vec{u}^T) = -\nabla P + \nabla\cdot\mu(\nabla(\vec{u}+\vec{u}^T) - \frac{2}{3}\nabla\cdot\vec{u}I) \tag{3.37}$$

where P is the pressure, μ is the fluid viscosity and I is the identity matrix. The viscosity of the mixture is computed using the ideal gas mixing law from fluent as [2]:

$$\mu = \sum_i \frac{x_i\mu_i}{\sum_j x_i\phi_{ij}} \tag{3.38}$$

where ϕ_{ij} is computed as [2]:

$$\phi_{ij} = \frac{[1+(\frac{\mu_i}{\mu_j})^{0.5}(\frac{M_j}{M_i})^{0.25}]^2}{[8(1+\frac{M_i}{M_j})]^{0.5}} \tag{3.39}$$

Conservation of energy Considering the existence of two phases in the problem, a conservation of energy for each phase is required. The conservation of energy in the fluid phase is [2]:

$$\frac{\partial\rho h}{\partial t} + \nabla\cdot(\rho h\vec{u}) = \nabla\cdot(k\nabla T) \tag{3.40}$$

which represents the transport equation of the enthalpy. For this work the viscous heating is neglected. This can be sustained by the low Brikman number expected for the cases under study:

$$Br = \frac{\mu u^2}{k\Delta T} \tag{3.41}$$

Wich relates the viscous heating energy per unit of time versus the heat energy dissipated per unit of time. If the ratio is very low, then the viscous term can be neglected in

comparison to the dissipated heat. For the simulations in this work, Br ≈ 4e-7, so that the viscous heating term can be neglected. The relationship between enthalpy and temperature is given by:

$$\frac{\partial h}{\partial T}|_P = C_p \tag{3.42}$$

The thermal capacity of the mixture is modeled similarly as the viscosity using Equations 3.38 and Equation 3.39, substituting the viscosities μ_i for the thermal conductivities k_i. The calculation using this relationship gave undistinguishable results compared to using the mass weighted approach for all the simulations presented in Chapter 5.

The energy balance for the solid phase is similar to the fluid phase, but without the convective term and with the parameters of thermal conductivity and density relevant for platinum. It is:

$$\frac{\partial \rho h_s}{\partial t} = \nabla \cdot (k_s \nabla T_s) \tag{3.43}$$

Species transport The species transport equation represents the convection and diffusion of the species in the fluid phase. It must be done for every species in the problem. Since the overall mass conservation equation accounts for the totality of the species, one of the species is redundant. For numerical stability, the most abundant species N_2 was calculated from the balance. The species balance can be written as [2]:

$$\frac{\partial \rho w_k}{\partial t} + \nabla \cdot (\rho w_k \vec{u}) = -\nabla \cdot \vec{J_k} \tag{3.44}$$

where w_i is the mass fraction of species i. The diffusive term is modelled according to Fick's law:

$$\vec{J_k} = -\rho D_{k,m} \nabla w_k \tag{3.45}$$

As the diffusivity of the mixture is a function of the composition, it was accounted for

in the following way [2]:

$$D_{i,m} = \frac{1 - X_i}{\sum_{j,j \neq i} X_j / D_{ij}} \tag{3.46}$$

The diffusivity matrix in this work is computed using Fuller correlation [23].

The system of governing equations is a coupled system of partial differential equations. The convective term of the equations make them nonlinear, and the preferred solution method is computational. In this work all results are made in Ansys Fluent 18.2, unless otherwise stated.

3.4.2 Turbulence and modelling

An important topic considered in this work is the effect of turbulence. Laminar flow is characterized by no significant mixing, and flow in sheets, hence the name. A turbulent flow, on the other hand, is characterized by irregular motions so that quantities such as velocity and pressure show a random variation with time and space coordinates [61]. The origin of turbulence can be thought with regards to a perturbation in the fluid field. The effect can either be magnified or it can disappear. If the instability is magnified, the flow may become turbulent. If the instability is reduced, then the flow may be laminar but time dependent [61].

The instability can originate from small perturbations in the flow. The accepted quantity to refer to when the perturbation may originate a magnified instability is the Reynolds number, which refers to the ratio of inertial forces against the viscous forces. Different situations have different critical Reynolds numbers.

Turbulence modelling

Many alternatives for modelling turbulence have been proposed. Some of them only apply to certain situations and other claim to be more general. Different modelling techniques vary in complexity. Good reviews of turbulence models can be found in [60, 76]. Considering the scope of this work, only one turbulence model will be explained in detail, called Large

Eddy Simulation.

Large Eddy Simulation Large eddy simulation represents directly the large unsteady turbulent motions in the flow. If the computational expense of Direct Numerical Simulation (DNS) prohibits its use for modelling turbulent flows, due to extremely fine grid requirements which are a cubic function of the Re [60], then DNS is very rarely used for industrial applications. A computational simplification is made with the use of LES in which the smallest dissipative motions, which are where most of the computational power is spent, is modelled by using simpler models. Larger modes of turbulence, which are rather specific to the geometry are computed explicitly. This simplification makes LES modelling more feasible to for engineering computations compared to DNS [60]. The steps to compute an LES models are [60]:

1. Filtering operation to the velocity, so that the mean velocity and fluctuations can be computed.

2. The equations of the filtered velocity field are derived from the Navier-Stokes equations. In the standard form, the stress tensor arises from the velocity residual, i.e., the actual velocity minus the filtered velocity.

3. Closure equations by modelling the residual stress tensor by an eddy viscosity model.

4. The model filtered equations are solved numerically for the filtered velocity field, providing information of the large scale motions of one realization of the turbulent flow.

The filter variable ϕ can be represented as:

$$\overline{\phi}(x) = \int_D \phi(x) G(x, x') dx' \tag{3.47}$$

where $\overline{\phi}(x)$ is the filtered variable, and $G(x, x')$ is the filtered function with respect to local coordinates x' and $G(x, x')$ is the filter function and D is the fluid domain. In this work LES

modelling is done using Ansys Fluent. The choice of filter of a variable ϕ is done naturally by the discretization process of the geometry as [2]:

$$\overline{\phi}(x) = \frac{1}{V}\int_V \phi(x')dx', x' \in V \tag{3.48}$$

Applying this filter to the velocity to obtain the filter velocity vector $\overline{u_i}$, the mass conservation equation remains seemingly unchanged from its non filtered counterpart [2]:

$$\frac{\partial \rho}{\partial t} + \frac{\partial}{\partial x_i}(\rho\overline{u_i}) = 0 \tag{3.49}$$

and for the momentum equation [2]:

$$\frac{\partial}{\partial t}(\rho\overline{u_i}) + \frac{\partial}{\partial x_j}(\rho\bar{u}_i\bar{u}_j) = \frac{\partial}{\partial x_j}(\sigma_{ij}) - \frac{\partial \overline{p}}{\partial x_i} - \frac{\partial \tau_{ij}}{\partial x_j} \tag{3.50}$$

where σ_{ij} is the stress tensor due to molecular viscosity defined as [2]:

$$\sigma_{ij} = \mu(\frac{\partial \overline{u_i}}{\partial x_j} + \frac{\partial \overline{u_j}}{\partial x_i}) - \frac{2}{3}\mu\frac{\partial \overline{u_l}}{\partial x_l}\delta_{ij} \tag{3.51}$$

and the term τ_{ij} is the the subgrid scale stress defined by [2]:

$$\tau_{ij} = \rho\overline{u_i u_j} - \rho\bar{u}_i\bar{u}_j \tag{3.52}$$

the subgrid scale stress tensor τ_{ij} is done with different eddy viscosity models, using the Boussinsq hypothesis. The definition of each of these models is beyond the scope of this section, however they will be named for completeness. One alternative is the use of the Smagorinsky-Lilly model, which uses a mixing length concept. An improvement to this model is the Dynamic Smagorinsky model in which the Smagorinsky model constant is modelled dynamically depending on the scales of motion. The Wall-Adapting Local Eddy-Viscosity (WALE) model is designed to return the correct wall asymptotic behaviour for wall bounded flows. The last of the methods covered by Ansys Fluent is the Dynamic Kinetic Energy Subgrid-Scale model. All of the details about the subgrid scale stress models can

be found in the Ansys Fluent documentation [2].

Inlet boundary conditions To simulate the behaviour of turbulent flow, in this work the spectral synthesizer method is used. This method generates a flow with fluctuating velocity components that are computed according to the methodology proposed by Kraichnan [41] and modified by Smirnov [66] according to the Ansys Fluent user manual [2]. Fluent generates a fixed number of 100 harmonics [2].

Chapter 4

Acceleration techniques for detailed microkinetics implementation

4.1 Lookup tables

In this chapter two approaches to precompute chemical data for computational acceleration are presented, namely the Lookup table approach and the Neural Network approach. In this section the lookup table is presented. All the code presented in this section can be found at www.github.com/antonfadic

4.1.1 Introduction

There are many situations found in chemical engineering where advanced computational modelling is used to simulate processes that are multi-scale in nature. Here we use the term multi-scale to identify process that occur at several spatial scales, which in typical problems can range over several orders of magnitude. Many such problems are modelled by a set of partial differential equations in space and time, the solution of which must be effected by an appropriate numerical method such as finite volume or finite element. A typical approach taken in the solution of multi-scale problems is to discretize only the largest scale, and then to incorporate the smaller scales into the simulation by the introduction of an appropriate sub-model. The generic term applied to sub-models in whatever form is a scale-bridge,

because it provides a method to include high resolution effects in a relatively low resolution model. Sub models can be as complex as a system of coupled partial differential equations, or as simple as a correlation via an algebraic equation. However, many times the price of simplicity is low accuracy or a narrow application range, which can lead to important deviations in either research or industrial applications. On the other hand, complex sub models can be computationally expensive and prohibitive to use in practice.

An example of a sub model consists of a detailed kinetic mechanism, which accounts for chemical transformations at a molecular scale. These sub-models are often reduced to so called global reactions, reducing considerably the number of intermediate species, at the cost of reducing its accuracy or application range. However, in many reactor models it is desirable to include detailed kinetic models, which consist of many elementary or pseudo-elementary steps containing a large number of species and reaction steps. An example of this is a combustion reaction, either homogeneous or heterogeneous catalytically enhanced, the latter being the example case of sub model used in this paper. However, the main issue with the use of a detailed kinetics model is that to obtain the surface reaction rates from those mechanisms, a considerable computational effort is often required. To determine the local reaction rates in terms of gas phase concentrations requires the solution of an initial value problem coupled with an algebraic condition giving a Differential Algebraic Equation (DAE), condition that arises from the site mole balance. These systems are stiff and differ considerably from ordinary initial value problems. Different packages exist to solve these systems, such as DASSL, or under Sundials (open source) the package IDA and CVODE for initial value problems. Specifically, for chemical kinetics rates computation, CHEMKIN and Cantera, (open source,using CVODE) are widely used. A general mathematical description of such mechanisms can be formulated as [35]:

$$\dot{\theta}_{k,j} = f(\theta_{k,j}, C_i, T) \tag{4.1}$$

$$g(\theta_{k,j}) = 0 \tag{4.2}$$

Equation (4.1) is a set of initial value problems that depends on the species coverage $\theta_{k,j}$, where the index k runs for all adsorbed species including the empty adsorption site, and the index j runs for the different sites if more than one is present. The rates of reaction, adsorption and desorption depend on the vector of surface species concentrations C_i and the surface temperature T. f is a function, defined as $f : \mathbb{R}^{N_{siSp}+N_{C_i}+1} \rightarrow \mathbb{R}^{N_{siSp}}$. g is a set of algebraic constraints, which physically represents the sites mole balance. In this mapping, f is a function taking the number of input parameters, the number site coverages N_{siSp}, plus the number of concentrations required by the mechanism N_{C_i}, typically equal to the number of adsorbed species, and the surface temperature T. The system is integrated until steady state is achieved, obtaining the equilibrium species coverages $\theta_{k,j}^{eq}$ as a function of the surface temperature T and surface concentrations that affect the mechanism C_i. With these parameters it is then possible to obtain the species reaction rates. In catalytic combustion, it is usually assumed that the source term for site species concentrations are in steady state, owing to the fast reacting timescales compared to those of the transport processes involved, as noted for example by [17]. Once the steady-state adsorbed species concentrations are found, the surface reaction rates can be computed. The microkinetic mechanism can be seen from a black box perspective, as a function of input of surface temperature, and surface concentrations and providing as output a set of surface reaction rates, and site coverages, and therefore, a good candidate for scale bridging. Normally these reactions are related to changes in temperature, concentration, pressure, density and flow distribution. To account for the transport effects, these mechanisms are normally coupled to computational fluid dynamics (CFD) packages. The direct solution of this mechanistic model at runtime with the CFD code by solving for each combination and node of surface concentration and temperature may be extremely expensive depending on the mechanism, and can show a dramatic increase in the computation time, being especially relevant as the number of adsorbed species is high. Several methods have been proposed to improve computational efficiency of the calculation of these rates without modifying the mechanism, and the majority corresponds to some form of data precomputation. A review of these methods

can be found in [68], and two of the most common approaches in data precomputation are presented as follows:

- Precomputed data stored in look-up tables: Also called repro-modelling. The idea consists of precomputing source terms at specified values of the parametric space (e.g., temperature, pressure, surface concentrations) that defines a grid, normally equally spaced. When a value is required for a given set of conditions, it can be interpolated from the values stored in the table. An important advantage of this approach is that it is an embarrassingly parallel problem, which allows the table generation to be distributed on several processors efficiently. The parameter ranges have to be set a priori, therefore, allowing for a complete decoupling of the mechanism with the underlying problem, which is one of the most important benefits of this method. However, it has not been possible to date to use it for mechanisms consisting of more than 6 variables, due to the exponential increase of the lookup table size with respect to the number of dimensions. Another problem that arises from this approach is that, due to the fact that the parameter space may not be cartesian (e.g., compositions due to stoichiometric restrictions), several nodes are never used. Even worse, depending on the application, some combinations within the feasible domain may not be needed at all, and therefore unnecessarily increase the size of the table.

- In Situ Adaptive Tabulation: This idea also consists of data precomputation, however the nodes are generated adaptively depending on the application, which corresponds to the in-situ part, and most commonly the call comes from a CFD application. This approach of data generation implies that the table is not equally spaced. A criterion is adopted for accuracy, and a rule is used to decide if whether a new call has to be made, or if a query can be used from a precomputed value [59]. The feasible domain is "patched" with ellipsoids. With a new query, the algorithm first checks if it lies within an area of tolerated error already computed. If not, then it computes the value at the node, and its ellipsoid of accuracy.

Look-up tables have recently been shown to be very effective in reducing the computational time of models for the catalytic combustion of methane in a washcoated monolith reactor using a detailed mechanistic model proposed by [16]. [72] used a lookup table for the reaction source terms that were pre-computed by integrating the chemistry of a grid of parameters. He showed that the same reactor performance was predicted with both the look-up table and the reactor simulator that used Cantera directly, but the lookup table required significantly less execution time. The multivariate spline methodology has found applications besides the domain of microkinetics mapping, such as multiscale modeling, [65, 71, 64, 63, 47, 20]. Another recent use of multivariate splines was done by [54], who use them to map the partial oxidation of methane and ethylene, and later implemented them into a commercial CFD package. More recently [75] used a memory optimized lookup table approach to simulate turbulent combustion. In a different field, splines have been used to accelerate the computation of the potential energy surface in molecular dynamics using splines [55].

ISAT has been extensively used in homogeneous combustion, and currently it is implemented in Fluent. [45] adapted the idea to heterogeneous combustion and used it for a mechanism consisting of 19 species, obtaining asymptotic speed up factors of 3 to 89, which varied depending on the tolerance. However, 5 % of the retrieved results were in violation of the prescribed tolerance. [42] have modified this technique and applied it to two different mechanisms consisting of 19 and 34 species, obtaining speed-up factors of 1.4 to 2.4 respectively. More recently, [9] have extended the use of ISAT to transient simulation, applying it on a methane reforming problem, and obtaining asymptotic speed up factors of the order of 20.

It is worth noting that precomputed data have found applications of scale bridging outside of the kinetic mechanism mapping. [47] extended the concept by developing look-up tables for average reaction rates that included the effects of both internal and external heat and mass transfer. They modelled a full scale catalytic converter by solving the transport equations for the macroscale, where the monolith brick was treated as a porous medium.

The complex fillet shape for the washcoat was accounted for in the calculation of the interal diffusion resistance. For this case, a hierarchical complete scheme for scale bridging was developed using pre-computed data stored in look-up tables. Speed-up factors of the order of 400,000 were achieved, compared to the case without any use of look-up tables. [20] then showed how such an efficient scheme could be used for a realistic parameter study of catalytic converters, in which a shape optimization study was performed. Another example of the application of this methodology in heterogeneous combustion is given in [63], who showed the speed-up for the solution of a dual layer catalyst for selective catalytic reduction.

In all of the cases mentioned above, the interpolation was done using the tensor product splines for interpolation. In this work we compare and contrast three alternatives for interpolation of precomputed data, namely, tensor product, Hermite splines and what we call the 4 point interpolation splines, such as Catmull-Rom splines, our hybrid method and the 4 point polynomial fit. The parameters to study are the size of the map, the number of function calls required to build a map, the time for interpolation, and their accuracy. First, background is provided about different interpolating schemes for one and several dimensions from a theoretical standpoint. Then, a brief explanation of the methodology used to obtain the tables is presented, showing the error measures, and the optimization of the number of nodes algorithm. Finally, an application for mechanism reduction is presented by taking as an example the ammonia oxidation mechanism, [40], and comparing the three schemes using the aforementioned performance measures.

4.1.2 Interpolation schemes

The basis of the interpolation schemes used in this study is one dimension, and several alternatives are discussed. However, most applications require the mapping of several variables, e.g., chemical species, and temperature, which requires several dimensions. Therefore, two alternatives are introduced to allow for a multiple dimension map.

One dimension

Let us consider in the first instance one dimensional interpolation schemes. The function to be approximated is $f(x)$ over the domain D. The function is approximated by an interpolating polynomial given by:

$$f(x) \approx p_j(t) = \sum_{i=0}^{p} a_{i,j} t^i \tag{4.3}$$

Because a low order interpolating polynomial is wanted to prevent the Runge phenomenon, the interpolation is done in a piecewise manner over sub-intervals of the domain, leading to splines. Usually the interpolating polynomials are of orders 1,2 or 3. The ramifications of each order are explained as follows:

- Linear (p=1): This is the most straightforward approach, in which a linear function consisting of two unknown coefficients is fitted over an interval. Its derivatives are not continuous between elements. The two coefficients can be obtained by enforcing element endpoints values on the element nodes.

- Quadratic (p=2): Three boundary conditions are needed for quadratic interpolation. Two of them are chosen as the interpolating boundary conditions, as done with the linear polynomial, which reduces the number of non determined coefficients to one. The most common approach to determine these coefficients is by enforcing continuity of the derivatives on the interior nodes, therefore being C^1. For the two boundary nodes, the second derivative is specified as 0, which effectively means that a linear polynomial is used to interpolate within the boundary element. If the assumption differs from the actual value, the implied error will be reduced as the grid is refined. The imposition of these boundary conditions leads to a matrix specification of the

system for each element, which is shown in Equation 4.4.

$$\begin{bmatrix} 1 & 0 & 0 & 0 & 0 & 0 & 0 & 0 & 0 \\ 1 & 1 & 1 & 0 & 0 & 0 & 0 & 0 & 0 \\ 0 & 0 & 2 & 0 & 0 & 0 & 0 & 0 & 0 \\ 0 & 0 & 0 & 1 & 0 & 0 & 0 & 0 & 0 \\ 0 & 0 & 0 & 1 & 1 & 1 & 0 & 0 & 0 \\ 0 & 0 & 0 & 0 & 1 & 2 & 0 & -1 & 0 \\ \cdots & \cdots & \cdots & \cdots & \cdots & \cdots & \cdots & \cdots & \cdots \\ \cdots & \cdots & \cdots & \cdots & \cdots & \cdots & \cdots & \cdots & \cdots \\ \cdots & \cdots & \cdots & \cdots & \cdots & \cdots & \cdots & \cdots & \cdots \\ 0 & 0 & 0 & 0 & 0 & 0 & 1 & 0 & 0 \\ 0 & 0 & 0 & 0 & 0 & 0 & 1 & 1 & 1 \\ 0 & 0 & 0 & 0 & 0 & 0 & 0 & 0 & 2 \end{bmatrix} \begin{bmatrix} a_{0,1} \\ a_{1,1} \\ a_{2,1} \\ a_{0,2} \\ a_{1,2} \\ a_{2,2} \\ \cdots \\ \cdots \\ \cdots \\ a_{0,k} \\ a_{1,k} \\ a_{2,k} \end{bmatrix} = \begin{bmatrix} f_1(0) \\ f_1(1) \\ 0 \\ f_2(0) \\ f_2(1) \\ 0 \\ \cdots \\ \cdots \\ \cdots \\ f_k(0) \\ f_k(1) \\ 0 \end{bmatrix} \tag{4.4}$$

Once the linear system of equations is solved, the coefficients are stored in a lookup table for interpolation, when needed. Note that a transformation has been made, by which instead of using absolute coordinates x_i, local coordinates are preferred using a parameter t, referring to the position of each element. The terms $f_j(t)$ refer to the function evaluation. If $t = 0$, it means the location on the left of element i and 1 means the right of element i. k refers to the number of elements into which the domain is partioned, and $a_{i,j}$ refer to the coefficients of the spline shown in Equation (4.3). Note that the obtained system is non-local, which means that if for some reason, some function evaluation is perturbed from the actual value, it will impact all the coefficients $a_{i,j}$. This is a consequence of the imposition of the condition of continuity of the derivatives.

- Cubic (p=3): For a cubic polynomial, four coefficients must be determined. This family of curves is $\mathcal{O}(4)$, although its overall order of accuracy depends on how the boundary conditions are implemented. Two of them are obtained by imposing the

interpolating boundary conditions, as shown in the previous two cases. To determine the remaining coefficients, in addition to the two interpolating boundary conditions, three alternatives are commonly used, namely:

- Natural: Enforce continuity of the first derivatives, and continuity of the second derivatives. Assume that the third derivatives at the boundary nodes are 0, [13], which effectively means using second order polynomial for the boundary elements. This method is non-local and it is C^2. Its formulation is similar to the one shown in equation 4.4.
- Imposed derivatives: Also called Hermite. If the partial derivatives at the nodes are known, as well as the function values, then use them to compute the interpolating polynomial. Its order of accuracy depends on the quality of the partial derivatives provided. After implementing these boundary conditions for each element, it is clear that the resulting interpolating polynomials do not depend on the values outside the elements, which shows that the approach is local. After inverting the resulting matrix to obtain the coefficients, the spline polynomial can be written as:

$$p_j(t) = \begin{bmatrix} 1 & t & t^2 & t^3 \end{bmatrix} \begin{bmatrix} 1 & 0 & 0 & 0 \\ 0 & 0 & 1 & 0 \\ -3 & 3 & -2 & -1 \\ 2 & -2 & 1 & 1 \end{bmatrix} \begin{bmatrix} f_j(0) \\ f_j(1) \\ f'_j(0) \\ f'_j(1) \end{bmatrix} \tag{4.5}$$

  which is C^1 continuous. This method is local, and therefore it can be used without calculating other coefficients. It is worth noting that the function derivatives must be provided as input.

  Recently, [36] have shown that the use of Hermite splines can reduce the data storage requirements for a test case when compared to the tensor product splines, which are a multidimensional spline approach discussed in the following section, while preserving the accuracy. They proposed two versions to estimate the

derivatives, namely, artificial and physical. In the former, the computation of the derivatives is made by two extra computations in the vicinity of a node to obtain its partial derivative using the central differencing scheme. The latter consist of fitting cubic spline with natural boundary conditions on the whole domain, from which the function derivatives at the nodes can be obtained analytically.

– Catmull-Rom: Similarly to the approach shown above, the interpolating boundary conditions can determine two of the four required coefficients. In this case, another approach to determine the derivatives at the nodes is used, which is based on the central difference scheme to estimate the first derivative at each node, as proposed by [10]. The partial derivatives provided in this case are therefore $\mathcal{O}(2)$. If a node has two neighbouring nodes, the derivative at the central node can be determined using central difference scheme. This approach is shown as follows:

$$p_j(t) = \begin{bmatrix} 1 & t & t^2 & t^3 \end{bmatrix} \begin{bmatrix} 1 & 0 & 0 & 0 \\ 0 & 0 & 1 & 0 \\ -3 & 3 & -2 & -1 \\ 2 & -2 & 1 & 1 \end{bmatrix} \begin{bmatrix} fl \\ fr \\ 0.5(fr - fll) \\ 0.5(frr - fl) \end{bmatrix} \tag{4.6}$$

Where fll is the function value on the left of the left node in the reference element $f_j(0)$, and frr is the function value on the right of the right node of the reference element $f_j(1)$. This approach does not use as an input the function derivatives, but instead, uses function values in the vicinity to estimate it.

The interpolation time is a parameter of critical importance, and it is strictly related to the number of floating point operations required to obtain an output. Therefore, for implementation purposes, it is important to use Horner's algorithm, which minimizes the number of floating point operations required to evaluate the polynomial. This is done by taking advantage of the matrix form,

and the coefficients of the polynomial can be computed as follows:

$$p_j(t) = a_0 + t(a_1 + t(a_2 + t(a_3))) \tag{4.7}$$

whose values are found in Table 4.1:

Table 4.1: Constants for interpolation based on the reference element

Constant	value
a_0	fl
a_1	fpl
a_2	$-3fl + 3fr - 2fpl - fpr$
a_3	$2fl - 2fr + fpl + fpr$

In case a query is located on a boundary element, perform a 3 point interpolation, computing the derivative where it is available.

- 4 Point polynomial fitting: Finally, another method was considered taking advantage of the 4 point stencil of the Catmull-Rom scheme. Considering the fact that the derivative calculation is only $\mathcal{O}(2)$ using central difference, this method takes advantage of the regular grid, and that 4 points are available for interpolation. In this way, in principle, a $\mathcal{O}(4)$ scheme for the derivative can be obtained. To do so, we used the interpolation across the whole element considering its 4 points, with a 3rd degree polynomial, same as the one shown in Equation 4.3. To obtain the corresponding boundary conditions, consider a 3th order polynomial that passes through the 4 point stencil.

$$\begin{bmatrix} 1 & -1 & 1 & -1 \\ 1 & 0 & 0 & 0 \\ 1 & 1 & 1 & 1 \\ 1 & 2 & 4 & 8 \end{bmatrix} \begin{bmatrix} a_0 \\ a_1 \\ a_2 \\ a_3 \end{bmatrix} = \begin{bmatrix} fll \\ fl \\ fr \\ frr \end{bmatrix} \tag{4.8}$$

After inverting the matrix, it is possible to obtain the coefficients, which are found in

table 4.2:

Table 4.2: Constants for interpolation based on the reference element, 4point polynomial fit.

Constant	value
a_0	fl
a_1	$\frac{1}{12}(-4fll - 6fl + 12fr - 2frr)$
a_2	$\frac{1}{2}(fll - 2fl + fr)$
a_3	$\frac{1}{6}(-fll + 3fl - 3fr + frr)$

In case the query lies on a boundary element, use a 3 point scheme to approximate the derivative, which reduces the order of convergence to 2. This method is equivalent to using the interpolating boundary conditions and calculating the derivatives using polynomial interpolation using the 4 point stencil.

Several dimensions

Now let us expand the analysis to consider the multidimensional case. In this study we consider three main approaches used to describe multiple dimension functions through splines. The p order polynomial tensor product spline used by [72] solves the following polynomial in D dimensions:

$$f(\mathbf{x}) \approx p(\mathbf{x}) = \sum_{j=0}^{p} \cdots \sum_{i=0}^{p} a_{i\ldots j} x_1^i \cdots x_j^p \tag{4.9}$$

It is easy to observe that this approach can lead to a large number of coefficients $a_{i\ldots j}$, which can be represented as a D rank tensor with each coordinate spanning a range from $0 \ldots p$.

An alternative approach for multidimensional interpolation, is the dimension reduction approach, which can be done in a similar way to a multilinear interpolation, which consists of creating a new grid that passes through the interpolated point in that dimension, and with it, reducing the number of dimensions by one, until 1 dimension is reached and then

using the scheme shown in the previous section. The computational implementation of this method is further explained in the next section.

Computational considerations

In this section we explain computational considerations only for our implementation of the Catmull-Rom scheme and the multidimensional 4 point polynomial fit. Tensor product splines are covered by [13] and stepwise Hermite splines are covered in [36]. The latter has been shown to reduce considerably the table size, when compared to a tensor product approach, however, at the expense of an increased number of computations per iteration, which is the trade off and it increases dramatically as the number of dimensions increase. [36] used Hermite spline with this approach for several dimension interpolation. This method belongs to the 2 point stencil method, which leads to the following number of polynomial evaluations.

$$N_{2P} = \sum_{j=1}^{D} 2^{D-j} = 2^D - 1 \tag{4.10}$$

For the case of Catmull-Rom in several dimensions the methodology differs, in which the new interpolated grids are calculated by using a four point stencil of the C-R splines. In this case the four point stencil in several dimensions must be retrieved from the table of function values. The number of values to be retrieved correspond to 4^D, as shown in figure 4.1, which shows an example for 2D.

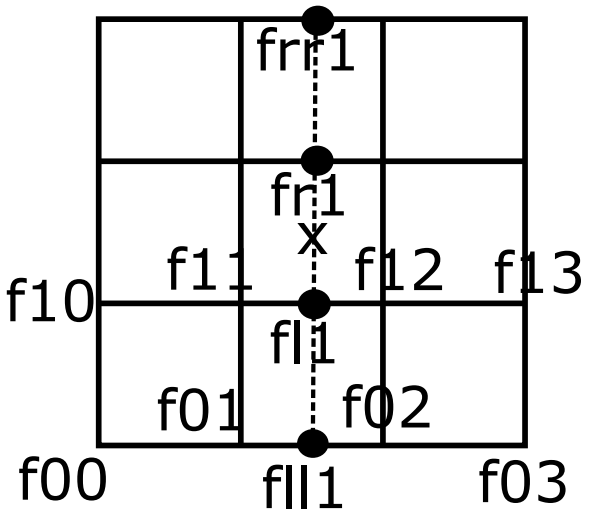

Figure 4.1: Dimension reduction from 2D to 1D with stepwise construction using Catmull-Rom Splines. X represents the query point location in the table.

The values are stored in memory contiguously, so they can be accessed by function efficiently. The order of cycling the dimensions is first X_1, then X_2 until X_n for n dimensions. This means that by finding the location of point f00, one immediately can compute the location of f01 to $f_{4\cdots4}$ in the table of function values.

Once these values are located, one can use either 4 point polynomial fit to find the interpolated point fll1 is calculated from the points f00, f01, f02 and f03, plus a variable t which is used to located the position of the query within the element and moves between 0 and 1, denoting the position of the coordinate to be reduced within the interval between f01 and f02. With this, the value of fll1 is obtained. The procedure is repeated advancing the next dimension to be reduced (x_2 in this case) by one breakpoint, and the procedure is repeated to obtain fl1, fr1 and frr1. Finally, a 1D mesh is obtained, which requires as input the values of fll1, fl1, fr1 and frr1 and the position with respect to x_2. For a general case, the number of interpolations required to obtain the solution is:

$$N_{4P} = \sum_{j=1}^{D} 4^{D-j} = \frac{4^D - 1}{3} \tag{4.11}$$

For our implementation, the code profiling of the 4 point interpolation at N=5 dimen-

sions, shows 85% of the time is spent on retrieving the 4D values from memory, whilst about 13% is spent on the CR interpolations. The remaining time is overhead. This indicates that the bottleneck of the implementation is accessing the table from RAM. No significant differences in time profile were encountered between the Catmull-Rom scheme and the 4 point polynomial fit.

Alternatively, to reduce the number of operations, we consider a combined scheme, in which we start from the table of function values, and from there, in the hypercube where a query is needed we compute the derivatives in RAM for use in the imposed derivative approach. This approach requires the same number of polynomial interpolations as shown in Equation 4.10, although it also requires the calculation of the partial derivatives with each query and requires the storage of the partial derivatives in RAM. The profiling of this code is the following: retrieving the values from memory takes 79% of time; calculating the derivatives takes 19% of time. Interestingly, the time to interpolate is reduced considerably, taking only 1% of time. Remaining time is overhead. It is important to notice that the implementation for this case takes about 10% longer to execute.

Summary and key parameters for comparison

The number of breakpoints required in each dimension is a function of the size of the parameter space in each dimension, the required accuracy, and the rate of change of the variable corresponding to its dimension. Because each interpolation method has different levels of accuracy, the required table size will vary among the methods. It is, however, useful to make a general comparison about the required memory usage for each method. In many cases, and especially for problems of higher dimensions, the memory requirements may be the most critical aspect. We emphasize that it is important that the entire table fit in RAM, else the disc access time will eliminate the advantages of using the table. A summary of the relationship between size, number of data and number of function evaluations is presented in Table 4.3.

Table 4.3: Comparison of different interpolation schemes, showing the number of function evaluations required to create a table, and the number of stored coefficients required for a table. N_i is the number of breakpoints in dimension i, and D is the total number of dimensions of the map.

Method	f(x) eval	number stored coeff
Tensor Product order p	$\prod_{i=1}^{D} N_i$	$\prod_{i=1}^{D}(N_i-1)(p+1)$
Hermite/Analytical.	$\prod_{i=1}^{D} N_i$	$(D+1)\prod_{i=1}^{D} N_i$
C-R, Hybrid and 4p Poly	$\prod_{i=1}^{D} N_i$	$\prod_{i=1}^{D} N_i$

The time to construct the table is dominated by the number of **function evaluations**, which is directly related to the number of stored coefficients, which in turn depends on the number of dimensions and on the number of breakpoints per dimension. Let us consider a case where $D = 5$, and taking $N_i = 10$ for every dimension. The overall time required will be the average time per computation times the number of required computations. The former varies widely depending on the application, and in this section we refer to the average computing time needed in this work in Section 4.1.4 which was found to be 4.8 ms. Clearly if the number of breakpoints is the same in each dimension, there is no difference in construction time for Tensor product of order p, Hermite analytical, and Catmull-Rom modified, in which case the time would be $N^D \cdot \bar{t}$. Substituting these known quantities, we obtain $10^5 \cdot 4.8/1000 = 8\ min$. It is important to remark that the Tensor product approach requires a global matrix inversion, whose time has not been considered and it might be considerable for large matrix sizes, which is the case when either N or D is large. Similarly, the Hermite/analytical approach requires the approximation of a spline through the table to compute the derivatives, which also requires computational power. It is important to mention that all the function evaluations are completely independent of each other, and therefore their computation is easy to parallelize. All the time estimations presented here assume that the evaluations are performed in series.

Let us continue our analysis with the table **size**. This parameter for each approach depends on the number of breakpoints and the number of dimensions of the problem. For

the Tensor Product, Hermite Spline, and Catmull-Rom, the total number of stored values is N^D. For Hermite, it would require 5 times that. Let us consider then, for illustration purposes, a situation where ten breakpoints are required in each dimension. The amount of memory can then be computed based on double precision storage, for each method with the number of dimensions. If we accept that a typical low cost personal computer has 128 GB of RAM, then for the case shown the use of tensor product splines with second order polynomials limits us to 7 dimensions, whilst the same splines with third order polynomials would be limited to 6 dimensions. Using Hermite splines increases the limit to 9 dimensions, whilst the Catmull-Rom splines allow for 10 dimensions.

The **interpolation time** depends on the time to retrieve the 2^D or 4^D function values from the table, depending on the approach, into another pointer plus the number of floating point operations required to obtain the interpolated value. For the 4 point stencil multidimensional interpolation schemes, the number of interpolations required to obtain a single value increases exponentially with the number of dimensions, as was shown in Equation 4.11, which can be derived by understanding that for a lookup table with D dimensions, a new grid of D-1 dimensions must be computed. This leads to a telescopic sum, which results in the given number of interpolations.

Finally, a fair comparison can be made only when leveling for **accuracy**. This is strictly case dependent upon the function f($\mathbf{x}$). Its speed of convergence can be known by the order of accuracy of the chosen method, which can be computed by analyzing the errors produced by successive mesh refinements. The error definition is presented in next section.

Error definition

To obtain a scalar representative of the deviation of the spline with respect to the actual function, at least two alternatives are proposed, based on a sample of N random data points lying within the domain:

- Root mean squared error:

$$e_j = \sqrt{\frac{1}{N}\sum_{i=1}^{N}(S_i - \hat{S}_i)^2} \tag{4.12}$$

where S_i stands for the source term from the combination of input i from the test data set and is computed from the mechanism, and $\hat{S}_i$ is the estimated output computed from the interpolation. e_j is the error of the j output. We also consider the following measure of accuracy, the root mean relative error:

- Root mean squared relative error:

$$e_j = \frac{1}{N}\sqrt{\sum_{i=1}^{N}\frac{(S_i - \hat{S}_i)^2}{S_i}} \tag{4.13}$$

Grid refinement strategy

The algorithm to refine the mesh follows a naive approach. From a starting grid of breakpoints, subdivide each dimension. Determine the RMSE associated with the subdivision and keep the breakpoints that give the largest decrease in RMSE.

4.1.3 Comparison results

In this section we consider a test function to precomputed using the three spline schemes discussed in this paper. The functions Combined and Catmull-Rom were developed in C, whilst the code for Hermite (imposed derivatives) is called from Matlab through a mex file. The first performed test was the required time to retrieve data from a query, whose results are presented in Figure 4.2.

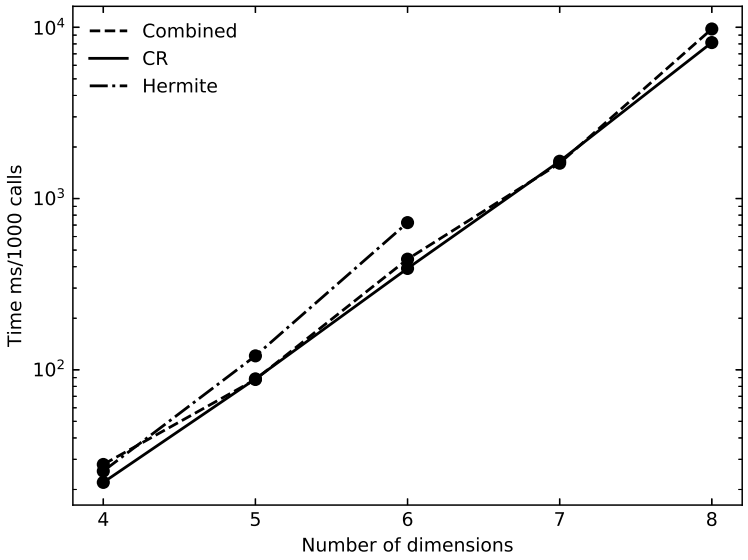

Figure 4.2: Interpolation time v/s number of dimensions for a test function. $N_i = 10$. Hermite spline code from [36].

All the breakpoints per dimension are 10. It is noticeable that the interpolation time escalates exponentially with the number of dimensions, as predicted by Equations and 4.10 and 4.11. However, they show similar trend, and Hermite shows a steeper trend. This might indicate that the bottleneck in the interpolation calculation does not occur in the stepwise dimension calculation. No data could be obtained after 6.

Another important timing test is to determine if whether the interpolation time escalates with the size of the grid, maintaining the number of dimensions constant. The test for 4 dimensions and successive mesh size increase is shown in Figure 4.3.

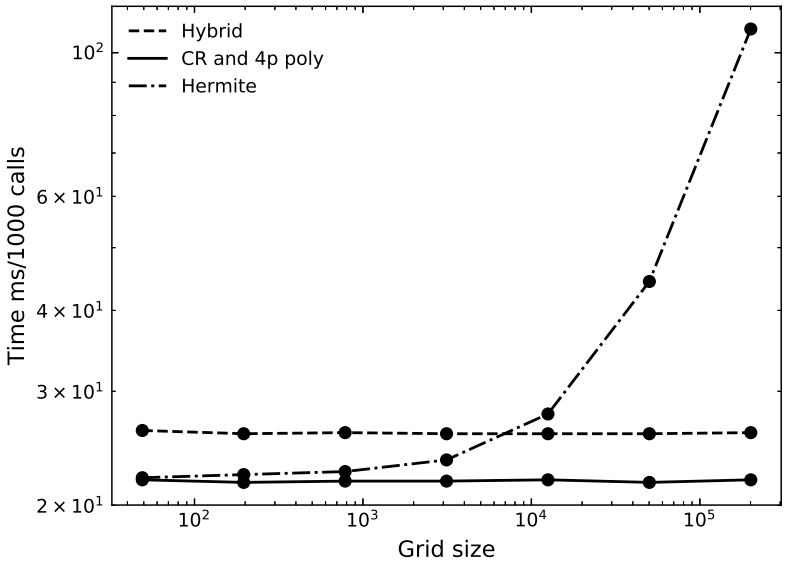

Figure 4.3: Interpolation time for varying grid sizes, for a 4 dimension table. Hermite spline code from [36].

The results of the test show that our implementation is efficient, in terms that the interpolation time is not a function of the number of elements of the grid. This is because we used functions to locate the values in memory as opposed to use search functions. The latter is the case of the Hermite interpolation scheme implemented by [36], which explains the behaviour shown in Figure 4.3.

A fair comparison of the performance of the different interpolating schemes must be done by comparing their benefits against their cost. One way to do so is by mapping the residuals against the memory required to build such tables. The results of this comparison are shown in the next section.

4.1.4 Applied comparison: ammonia oxidation mechanism

In this section we present a real test case and to account for accuracy, in this section we compare the performance of the three interpolating schemes to reduce the ammonia oxidation mechanism proposed by [40], which consists of 10 reactions and 4 adsorbed species.

The pressure is fixed at 5 bar, and for this study ideal gas behaviour is assumed. The reaction mechanism is shown in the following table:

Table 4.4: Reaction expression, rates and parameters [40] for the oxidation of ammonia over Pt

Reaction	Rate exp	$k_{i,T=385^\circ C}$	E_a kJ/mol
$NH_3 + b \longrightarrow NH_3{-}b$	$k_1 p_{NH_3} \theta_b$	6.38E-01	0
$NH_3{-}b \longrightarrow NH_3 + b$	$k_2 \theta_{NH_3-b}$	2.17E+00	60.9
$O_2 + 2\,a \longrightarrow 2\,O{-}a$	$k_3 p_{O_2} \theta_a^2$	2.94E-01	0
$2\,O{-}a \longrightarrow O_2 + 2\,a$	$k_4 \theta_{O-a}^2$	1.09E-10	181.0
$NH_3{-}b + (3/2)O{-}a \longrightarrow$ $N{-}a + (3/2)\,H_2O + (1/2)\,a + b$	$k_5 \theta_{NH_3-b} \theta_{O-a}$	5.91E02	99.5
$NO{-}a \longrightarrow NO + a$	$k_6 \theta_{NO-a}$	1.24E+00	154.8
$NO + a \longrightarrow NO{-}a$	$k_7 p_{NO} \theta_a$	2.63E-01	63.5
$2\,N{-}a \longrightarrow N_2 + 2\,a$	$k_8 \theta_{N-a}^2$	6.42E+01	139.0
$N{-}a + O{-}a \longrightarrow NO{-}a + a$	$k_9 \theta_{N-a} \theta_{O-a}$	9.34E+00	135.4
$NO{-}a + N{-}a \longrightarrow N_2O + 2\,a$	$k_{10} \theta_{NO-a} \theta_{N-a}$	5.20E+00	155.2

The reaction rates are obtained by computing the Arrhenius term for each reaction k_j, where Tref = 385 °C:

$$k_i(T) = k_i(T_{ref}) exp\big[- \frac{E_{a,j}}{R} (\frac{1}{T} - \frac{1}{T_{ref}}) \big] \tag{4.14}$$

And the reaction rates are obtained by:

$$r_i(T) = k_i(T) \prod_j p_j^{n_{i,j}} \prod_k \theta_k^{n_{i,j}} \tag{4.15}$$

The surface coverages are found by integrating the DAE equations:

$$\frac{d\theta_{k,j}}{dt} = \sum_i \nu_{kji} r_i \tag{4.16}$$

$$\sum_j \theta_{k,j} = 1 \tag{4.17}$$

$$\theta_{k,j}(0) = \theta_{k,j}|_0 \tag{4.18}$$

The DAE system shown in Equation (4.16), is integrated until the surface coverages $\theta_{k,j}$ are in steady state. For the lookup table computation, the range of the input parameters has to be specified beforehand. All the schemes use the same ranges and scales, which are shown in Table 4.5.

Table 4.5: Domain description

Variable	min	max	scale
Temperature K	450	1400	$1/x$
xNH_3	1e-6 %	12 %	log(x)
xNO	1e-6 %	12 %	log(x)
xO_2	8 %	20 %	log(x)
Output			
rNH_3 rNO rN_2O			log(x)

A better perfomance was obtained when the input parameters were scaled, following [72], and also the output source rates are stored in a scaled manner which proved to affect the most the error reduction.

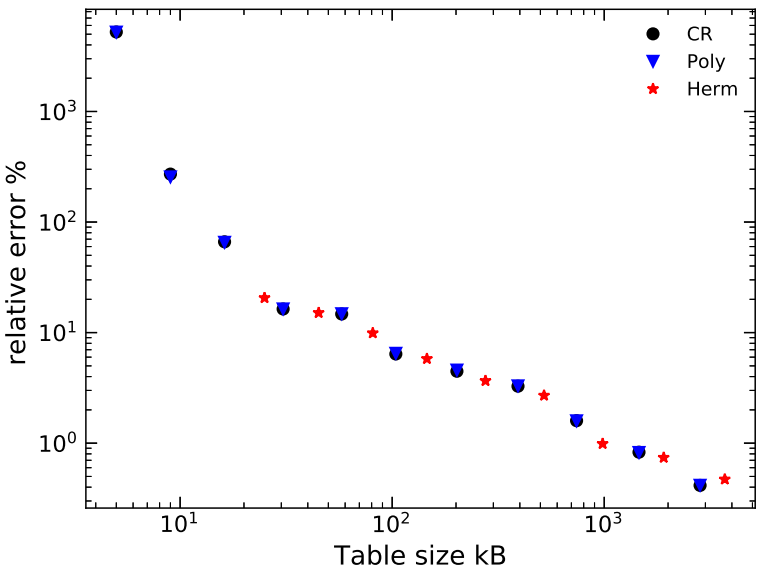

Figure 4.4: Relative errors Ammonia oxidation source term versus table size. Data generated from grid refinement. Same sample data for every comparison. Hermite spline code from [36].

In Figure 4.4, the results of the application of different interpolation method are presented. The residuals evaluated by their relative errors are shown as a function of the table size. The different data points correspond to the grid obtained by the refinement strategy using relative errors, following the same methodology described in this paper, starting at 5 breakpoints per dimension. The two different schemes followed different paths to convergence. The location of every point in Figure 4.4 can be understood as the information density of a given scheme. It is found that for a given amount of memory required, all methods have similar information density, as they lie on the same line. This implies that these methods are not different in terms of memory requirement compared to their accuracy.

In terms of the interpolation time, the average time to compute a data point from the chemistry module is of 4.8 ms. This compares to 0.59 ms to retrieve the value from Hermite mex file, and 0.22 ms to retrieve the value from a 4D CR or 4 point polynomial fit table in C, which gives speeds ups of 8.13x for Hermite, and 21.81x for the four points methods.

Finally, it is worthwhile noting that for achieving the same accuracy, the four point

methods require a finer grid, which implies more function calls, as shown in Figure 4.5. Evaluating the function might be expensive, depending on the submodel, and makes the Hermite family of methods more beneficial for building the table.

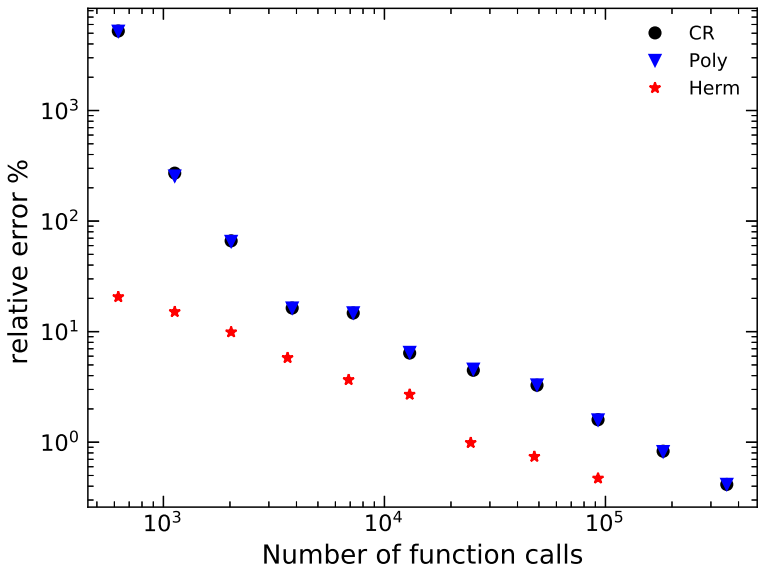

Figure 4.5: Relative errors as a function of the required number of function evaluations for different interpolation schemes. Hermite spline code from [36].

4.1.5 Example of an application: six dimensional steam methane reforming

To show the use of the lookup table in higher dimensions, a mechanism for methane reforming of six input variables was used. The overall reactions are known to be equilibrium reactions shown as follows:

Table 4.6: Overall reactions for steam methane reforming

$CH_4 + H_2O \longleftrightarrow CO + 3\,H_2$	Methane Steam Reforming
$CO + H_2O \longleftrightarrow H_2 + CO_2$	Water Shift reaction

The reaction to be mapped is the methane reforming over Nickel catalyst, of which

a detailed kinetic mechanism was developed in [14]. The reaction was converted from Chemkin format to Cantera format using Cantera version 2.3 [25], and then run using the Cantera Matlab toolbox. The mechanism consists of 6 inputs (Surface temperature and surface concentration of the adsorbed species), 15 site species and 52 reactions.

The interpolation tool used to map this mechanism is the modified Catmull-Rom, and the same methodology shown in Sections 4.1.2 and 4.1.3 was used. For the error calculation, a random set of data points within the hypercube comprised by the cartesian product of the vectors of the any breakpoints would not be representative of the realizable composition space, since many combinations of it can be not physical. To account for this, the two overall equations were advanced from a presumptive inlet feed composition. Independent random numbers were generated to account for the degree of progress of each reaction, giving place to a composition space to generate the source rates. The initial mole fractions for doing so are xCH_4=0.25 and xH_2O=0.75, which are representative of industrial operation [34].

Because of the equilibrium nature of the reaction, source rates are expected for CO_2 and CO to be either positive or negative, which impedes the application of the logarithm transformation. In this case, density of breakpoints was chosen as an alternative to map the mechanism, whose parameters are shown in table 4.8.

The resulting table contains 24,137,569 entries. If stored in double precision, each tables' size is 193.1 MB. The table construction was divided into 10,000 sections, which are all independent among each other, and run in parallel in the same machine with 3 workers at any given time. Each section took on average 2 min to run, giving a total CPU time of 80.5 h . It was found out that it was required to do so since the Matlab implementation of Cantera tended to leak memory. Every iteration to obtain the result started with an initial guess of the last iteration. If the solver failed to converge, the initial conditions were imposed. If the solver failed to converge after this step, the last converged value replaced the value in the table.

Table 4.7: Rates and parameters [14] for the reforming of methane over Ni

	Reaction	A (cm,mol,s)	E_a (kJ/mol)	β (-)	ϵ_i (kJ/mol)
R1	$H_2 + 2\,Ni(s) \longrightarrow 2\,H(s)$	3.00 x 10^{-2}	5.0	0.000	
R2	$2\,H(s) \longrightarrow 2\,Ni(s) + H_2$	2.54 x 10^{+19}	95.2	0.000	
R3	$O_2 + 2\,Ni(s) \longrightarrow 2\,O(s)$	4.36 x 10^{-2}	1.5	-0.206	
R4	$2\,O(s) \longrightarrow O_2 + 2\,Ni(s)$	1.18 x 10^{+21}	468.9	0.823	
R5	$H_2O + Ni(s) \longrightarrow H_2O(s)$	1.00 x 10^{-1}	0.0	0.000	
R6	$H_2O(s) \longrightarrow H_2O + Ni(s)$	3.73 x 10^{+12}	60.7	0.000	
R7	$CO_2 + Ni(s) \longrightarrow CO_2(s)$	7.00 x 10^{-6}	0.0	0.000	
R8	$CO_2(s) \longrightarrow CO_2 + Ni(s)$	6.44 x 10^{+7}	25.9	0.000	
R9	$CO + Ni(s) \longrightarrow CO(s)$	5.00 x 10^{-1}	0.0	0.000	
R10	$CO(s) \longrightarrow CO + Ni(s)$	3.56 x 10^{+11}	111.2	0.000	-50.0 $\theta_{CO(s)}$
R11	$CH_4 + Ni(s) \longrightarrow CH_4(s)$	8.00 x 10^{-3}	0.0	0.000	
R12	$CH_4(s) \longrightarrow CH_4 + Ni(s)$	8.70 x 10^{+15}	37.5	0.000	
R13	$CH_4(s) + Ni(s) \longrightarrow CH_3(s) + H(s)$	1.54 x 10^{+21}	55.8	0.087	
R14	$CH_3(s) + H(s) \longrightarrow CH_4(s) + Ni(s)$	1.44 x 10^{+22}	63.4	-0.087	
R15	$CH_3(s) + Ni(s) \longrightarrow CH_2(s) + Ni(s)$	1.54 x 10^{+24}	98.1	0.087	
R16	$CH_2(s) + H(s) \longrightarrow CH_3(s) + Ni(s)$	3.09 x 10^{+23}	57.2	-0.087	
R17	$CH_2(s) + Ni(s) \longrightarrow CH(s) + H(s)$	3.70 x 10^{+24}	95.2	0.087	
R18	$CH(s) + H(s) \longrightarrow CH_2(s) + Ni(s)$	9.77 x 10^{+24}	81.0	-0.087	
R19	$CH(s) + Ni(s) \longrightarrow C(s) + H(s)$	9.88 x 10^{+20}	21.9	0.500	
R20	$C(s) + H(s) \longrightarrow CH(s) + Ni(s)$	1.70 x 10^{+24}	157.9	-0.500	
R21	$CH_4(s) + O(s) \longrightarrow CH_3(s) + OH(s)$	5.62 x 10^{+24}	92.7	-0.101	
R22	$CH_3(s) + OH(s) \longrightarrow CH_4(s) + O(s)$	2.98 x 10^{+22}	25.8	0.101	
R23	$CH_3(s) + O(s) \longrightarrow CH_2(s) + OH(s)$	1.22 x 10^{+25}	134.9	-0.101	
R24	$CH_2(s) + OH(s) \longrightarrow CH_3(s) + O(s)$	1.39 x 10^{+21}	19.0	0.101	
R25	$CH_2(s) + O(s) \longrightarrow CH(s) + OH(s)$	1.22 x 10^{+25}	131.3	-0.101	
R26	$CH(s) + OH(s) \longrightarrow CH_2(s) + O(s)$	4.40 x 10^{+22}	42.4	0.101	
R27	$CH(s) + O(s) \longrightarrow C(s) + OH(s)$	2.47 x 10^{+21}	57.7	0.312	
R28	$C(s) + OH(s) \longrightarrow CH(s) + O(s)$	2.43 x 10^{+21}	118.9	-0.312	
R29	$H_2O(s) + Ni(s) \longrightarrow H(s) + OH(s)$	3.67 x 10^{+21}	92.9	-0.086	
R30	$H(s) + OH(s) \longrightarrow H_2O(s) + Ni(s)$	1.85 x 10^{+20}	41.5	0.086	
R31	$H(s) + O(s) \longrightarrow OH(s) + Ni(s)$	3.95 x 10^{+23}	104.3	-0.188	
R32	$OH(s) + Ni(s) \longrightarrow H(s) + O(s)$	2.25 x 10^{+20}	29.6	0.188	
R33	$2\,OH(s) \longrightarrow H_2O(s) + O(s)$	2.34 x 10^{+20}	92.3	0.274	
R34	$H_2O(s) + O(s) \longrightarrow 2\,OH(s)$	8.14 x 10^{+24}	218.4	-0.274	
R35	$C(s) + O(s) \longrightarrow CO(s) + Ni(s)$	3.40 x 10^{+23}	148.1	0.000	
R36	$CO(s) + Ni(s) \longrightarrow C(s) + O(s)$	1.75 x 10^{+13}	116.2	0.000	
R37	$CO(s) + H(s) \longrightarrow C(s) + OH(s)$	3.52 x 10^{+18}	105.4	-0.188	
R38	$C(s) + OH(s) \longrightarrow H(s) + CO(s)$	3.88 x 10^{+25}	62.5	0.188	-50 $\theta_{CO(S)}$
R39	$2\,CO(s) \longrightarrow C(s) + CO_2(s)$	1.62 x 10^{+14}	241.7	0.500	-50 $\theta_{CO(S)}$
R40	$CO_2(s) + C(s) \longrightarrow 2\,CO(s)$	7.29 x 10^{+28}	239.2	-0.500	-100 $\theta_{CO(S)}$
R41	$CO(s) + O(s) \longrightarrow CO_2(s) + Ni(s)$	2.00 x 10^{+19}	123.6	0.000	
R42	$CO_2(s) + Ni(s) \longrightarrow CO(s) + O(s)$	4.64 x 10^{+23}	89.3	-1.000	-50 $\theta_{CO(S)}$
R43	$CO(s) + OH(s) \longrightarrow COOH(s) + Ni(s)$	6.00 x 10^{+21}	97.6	0.213	
R44	$COOH(s) + Ni(s) \longrightarrow CO(s) + OH(s)$	1.46 x 10^{+24}	54.3	-0.213	
R45	$CO_2(s) + H(s) \longrightarrow COOH(s) + Ni(s)$	6.25 x 10^{+24}	117.2	-0.475	
R46	$COOH(s) + Ni(s) \longrightarrow CO_2(s) + H(s)$	3.73 x 10^{+20}	33.6	0.475	
R47	$CO(s) + H(s) \longrightarrow HCO(s) + Ni(s)$	4.00 x 10^{+20}	132.2	-1.000	-50 $\theta_{CO(S)}$
R48	$HCO(s) + Ni(s) \longrightarrow CO(s) + H(s)$	3.71 x 10^{+21}	0.0	0.000	
R49	$HCO(s) + Ni(s) \longrightarrow CH(s) + O(s)$	3.79 x 10^{+14}	81.9	0.000	+50 $\theta_{CO(S)}$
R50	$CH(s) + O(s) \longrightarrow HCO(s) + Ni(s)$	4.59 x 10^{+20}	109.9	0.000	
R51	$H(s) + COOH(s) \longrightarrow HCO(s) + OH(s)$	6.00 x 10^{+22}	104.8	-1.163	
R52	$HCO(s) + OH(s) \longrightarrow COOH(s) + H(s)$	2.28 x 10^{+20}	15.9	0.263	

Table 4.8: Domain description and errors for methane reforming detailed kinetic mapping

Variable	min	max	breakpoints
Temperature K	850	1100	17
xCH_4	0.08	0.25	17
xH_2O	1e-4	0.75	17
xH_2	1e-4	0.52	17
xCO	1e-4	0.13	17
xCO_2	1e-4	0.13	17
Output			
source rate	error		
rCO	0.40 %		
rCO_2	1.90%		

For comparison purposes, each table would be 1.35 GB under Hermite splines approach, 8.59 TB under Tensor Product second order, and 97.8 TB under Tensor Product 3rd order. The accuracy of the resulting table is shown in Table 4.8.

As for interpolation time, the code in Matlab runs at an average of 15.1 ms per iteration, whilst the average time in Cantera for solving the chemistry is 49.7 ms, giving a speed up factor fo 3.31x. When the interpolation is done in C, the interpolation time is on average of 9 ms, pushing the speed up factor to 5.52x. This might be connected to the fact of the contiguous allocation of memory in C, which if not done, as shown in the previous section with the timing profile for execution, can delay the execution. It is worthwhile noting then the benefit of storing less memory in RAM, because if more is needed as in the case of the other splining techniques, it would be difficult to allocate it contiguously, leading to a memory fragmentation which in turn will lead to a performance loss.

4.1.6 Conclusions

Detailed mechanisms for catalytic combustion are available, and several methods for reducing their computational complexity have been proposed. Normal drawbacks of the precomputed data approach are extensive memory requirements for a given accuracy, large interpolation times which are especially important for functions of several dimensions, and

interpolation times that are dependent on the grid size. It this paper we present a way in which the interpolation times can be made independent of the grid size, while being as memory efficient as other similar methods.

It is worthwhile noting that the same methodology can be used to bridge different scales that are inherent to modelling these kind of reactors in an efficient manner [20, 47, 63, 72]. Thus, here it has been shown that a more efficient approach can be obtained by using a modified Catmull-Rom spline interpolation scheme for these applications, which can provide considerably higher speed up factors if the function to be mapped is computationally expensive, such as those involving the resolution of the transport equations, while preserving the accuracy and reducing the disc space required and without increasing the number of function calls.

4.2 Artificial Neural Networks

A natural extension of the lookup table approach consists of using neural networks. More specifically, the kind of neural network to consider are those use for regression such as a multilayer perceptron. In this section, an investigation of the use of neural network to study its ability to predict the source rates of ammonia oxidation. The idea to explore is the Neural Network's approach to predict reaction rates accurately, fast and with limited memory usage.

4.2.1 Literature review

The idea of using neural networks for precomputation of source terms is not new, having been considered by many studies especially in the homogeneous combustion [12, 8, 7, 11, 44]. More recently [22], following the work by [7] has used a combination of a Kohonen Self Organizing map (SOM) with the Multilayer Perceptron (MLP) to precompute the calculation of the thermochemistry for a Sydney flame L, which is a turbulent non-premixed flame. This was done using the GRI 1.2 mechanism and reducing it wit the Rate-Controlled-Constrained-Equilibrium (RCCE) and the Computational Singular Pertubartion (CSP).

They resolved the flow field using LES, and the turbulence-chemistry interaction was modelled with the transport of the probability density function (PDF). They showed that the combined SOM-MLP can provide a good representation of the composition space while offering large savings in CPU time. To the best of the author's knowledge, this methodology has never been used in heterogeneous combustion, such as the ammonia oxidation over Pt.

4.2.2 Methodology

Considering the results of the lookup tables section, there is enough information to train a Multilayer Perceptron to study if the lookup table can be computed faster and with smaller use of memory. The inputs are the same as with the lookup table case, as T,xNH_3, xNO, xO_2. The output for the case of study consists of only the ammonia oxidation rate rNH_3. For this, 500,000 data points were taken from the lookup table approach.

The first step is to transform the input data, similarly as the step shown in the lookup tables, as:

Table 4.9: Data transformation

Variable	min
Temperature K	$1/x$
xNH_3	log(x)
xNO	log(x)
xO_2	log(x)
Output	
rNH_3 rNO rN_2O	log(x)

The next step is to determine the architecture of the net.

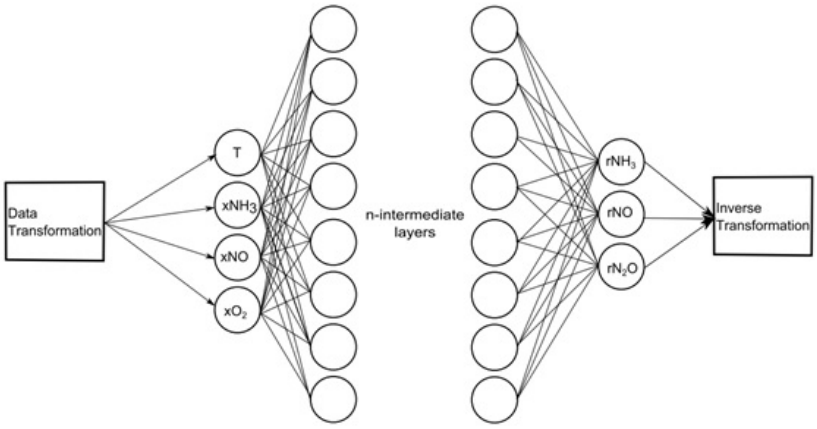

Figure 4.6: Schematics of the Multilayer Perceptron

The input layer shown in Figure 4.6 is a random subset of all the combinations used to build the lookup table used in the previous section. This random set is called the training set. A testing set was set aside which was used later to observe the performance of the model without interference in its calculation. This is useful to prevent overfitting. Each intermediate layer consists of neurons connected to the previous layer and the next layer. Neurons are connected among themselves through the weights, which is one of the parameters needed for the calculation of the output. Aside from the weights, a bias is required on each layer.

Consider the weights in the network from layer i to the layer j as w_{ij} and bias of layer j b_j. Consider the values of the layer i-1 as L_{i-1}. Then the values of the layer L can be computed as:

$$L_j = a(w_{ij}L_{i-1} + b_j) \tag{4.19}$$

where a = a(x) is the activation function. The activation function can be in principle any function, for example the identitity function, a linear function or a non-linear function. For the output layer a linear activation function was used. For every other layer, the activation

function was:

$$a(x) = \frac{2}{1 + e^{-2x}} - 1 \tag{4.20}$$

called the tansig function. This is mathematically equivalent to the hyperbolic tangent function, but Matlab implements it in this form for performance. The election of the hyperbolic tangent function has advantages for the training algorithm. Since the algorithm relies on a minimization process, the derivatives of the algorithm are used. The derivative of the tansig function is:

$$\frac{d(\text{tansig}(x))}{dx} = d\text{tansig}(x) = \frac{4e^{-2x}}{(e^{-2x} + 1)^2} \tag{4.21}$$

Considering that the inputs are mapped into the (-1,1) interval linearly, the activation function looks like:

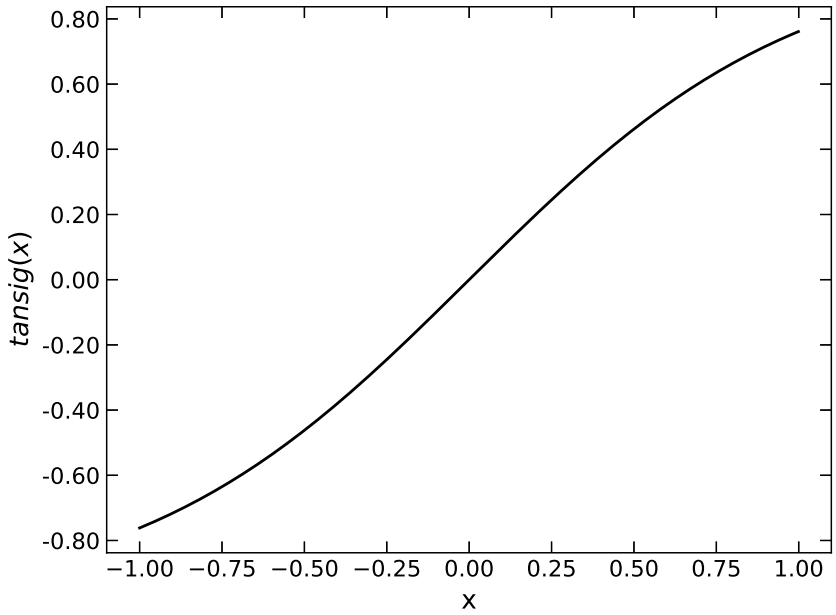

Figure 4.7: Tansig activation function in [-1,1]

Although there is no limit in any hidden neuron to have a value bounded by [-1,1]. However, when the tansig function is applied on a value much higher than 1, the output

will be very close to 1. In these cases it can be said that the neuron is saturated.

The function tansig is shown in the range of [-1,1]. Other properties of this function is its nonlinearity, which is needed to approximate nonlinear functions and that it does not saturate easily, meaning that it does not reach high or low values very easily. This is a good property to have for function representations [6]

Once the neural network is set up the training process can start. Firstly, as mentioned above, the data is separated into a training set and a validation set. For this case 70% training and 30% validation was used. Then the net was initiated with random weights. Then the backpropagation algorithm is used to compute the errors of the network associated to the current weights, consisting of evaluating the weight corrections for each of the layers [6]. The correction method depends on the training algorithm and the error function. In this case, the sum of the errors was used:

$$\epsilon = \frac{1}{2}\sum e_i^2 = \frac{1}{2}\sum \log(\frac{y_m}{y_d})^2 \tag{4.22}$$

which is the function to minimize. The values y_m and y_d are the outputs modelled and the one regargind the data, respectively, so that the error function is the sum of the relative deviations and not absolute. This proved to work better in this case.

There are several options for training algorithm, each of them with advantages and disadvantages. In this case, the Levenberg-Marquardt algorithm was used. The discussion of the different algorithms is beyond the scope of this work, but good reviews can be found in [6] and [27].

4.2.3 Optimization algorithm

In this section a brief explanation of the Matlab implementation of the Levenberg-Marquardt algorithm is provided. First, the optimization process starts from considering the error or loss function shown in Equation 4.22. The optimal is achieved when the partial derivatives

to the parameters, in this case weights and biases, are 0:

$$\frac{\partial \epsilon(x, w_i))}{\partial w_i} = 0 \tag{4.23}$$

The backpropagation algorithm starts by having an initial value for the weights, so that an initial error estimate can be made. Then, the partial derivatives of the error can be made with respect to every weight or bias. For a two hidden neuron architecture, where the input is treated with activation function a and the layer close to the output is treated with the identity function, the output is computed as:

$$O(x) = w_{11}^2 L_1 + w_{21}^2 L_2 + b_2 \tag{4.24}$$

Where w_{11}^2 is the weight connecting the first neuron of layer 1 to the first neuron of output 1. In general, it can be written as w_{ij}^N, where N is the hidden layer N, i is the originating neuron and j is the destination neuron. In this reference, the input corresponds to layer 1.

The hidden layer neuron L_1 as:

$$L_1(x) = a(w_{11}^1 x_1 + w_{21}^1 x_2 + b_1) \tag{4.25}$$

Where a is the activation function. In this work the function tansig was used, shown in Equation 4.21. In general the neuron i of layer N can be computed as:

$$L_i^{N+1}(x) = a(b_N + \sum_1^k w_{ij}^N L_j^N) \tag{4.26}$$

Therefore, the output is a composition of functions. The quantity inside the brackets is referred as net_i^N. When computing the derivative of the output with respect to the weights, the chain rule can be used:

$$\frac{\partial O}{\partial w_{11}} = \frac{\partial O}{L_1^1} \frac{\partial L_1^1}{\partial net_1} \frac{\partial net_1^1}{\partial w_{11}} \tag{4.27}$$

Which for this example yields:

$$\frac{\partial O}{\partial w_{11}} = w_{11}^2 d\text{tansig}(net_1)x_1 \tag{4.28}$$

Considering the derivative of the residual:

$$\frac{\partial \epsilon}{\partial w_{11}} = \sum_{i=1}^{p}(y_i - O(x_i))\frac{\partial O}{\partial w_{11}} \tag{4.29}$$

Where y is the desired output, x is the input and p is the number of patterns, which is the length of the y_i vector. The derivatives must be calculated for all the parameters, and therefore the derivatives are a vector of size equals to the number of parameters. For deeper nets, which require higher number of hidden layers, the same procedure can done.

Levenberg-Marquardt algorithm

Now the question lies on how to minimize the function $\epsilon(w, x)$. The gradient indicates the direction in which the minimization occurs, but no information about the optimal step size is given. If a gradient descent method is used, a constant learning rate γ is used to update the weights as:

$$\delta w_{ij}^N = -\gamma \frac{\partial \epsilon}{\partial w_{ij}^N} \tag{4.30}$$

This method is slow because it has a linear convergence rate. However, it is stable, and it is good for early approximations, when the initial guess is far from the optimum. A second order convergence rate can be achieved with Newton method, which has the advantage of being fast, but it lacks reliability due to its instabilities and lack performance due to the need of computing the determinant of the Hessian matrix. This method can be derived by simply applying Taylor's expansion around (x+h) for a single variable function f(x):

$$f'(x+h) = f'(x) + hf''(x) + H.O.T. = 0 \tag{4.31}$$

Where H.O.T. refer to higher order terms. By making the derivative around the next iteration point x+h zero, then the step size can be found to be:

$$h = -f'(x)/f''(x) \tag{4.32}$$

Using a similar argument, it generalizes to higher dimensions by substituting the derivative by the Jacobian, and the second derivative by the Hessian of the function f, in which case the vector h is obtained.

The drawbacks of this method consists mainly of its instability and computational expense to compute the determinant of the Hessian. However, when the error is low, the solution can converge very quickly.

The Gauss-Newton method can remedy the expensiveness of the Hessian determinant for quadratic type objective functions. The Hessian of the error if it is a quadratic function is the gradient of the gradient of the errors:

$$\nabla E = r^T \nabla r \tag{4.33}$$

hence, the Hessian is:

$$\nabla^2 E = r^T \nabla^2 r + \nabla r \nabla r^T \tag{4.34}$$

since the gradient of the residual is ∇O, then for small errors the Hessian can be approximated by:

$$\nabla^2 E = \nabla O \nabla O^T \tag{4.35}$$

The Levenberg-Marquardt algorithm tries to blend the best capabilities of both the gradient descent, and the Gauss-Newton algorithm, by calculating the Hessian as:

$$\nabla^2 E = \nabla O \nabla O^T + \mu I \tag{4.36}$$

Where μ is the parameter that blends between the Gauss Newton method when μ is very small, or the gradient descent with very small step when the parameter μ is large. Therefore, the weights update in the Levenberg-Marquardt algorithm is:

$$\delta w_{ij}^{N} = -\frac{\nabla O}{\nabla O \nabla O^{T} + \mu I} \tag{4.37}$$

Different heuristics exist. In this work Matlab's default heuristic of initial $\mu = 1e3$ is used, with update rule of $\mu_{i+1}/\mu_i = 0.1$ if the error is reduced in the iteration, or $\mu_{i+1}/\mu_i = 10$ if the error is increased in the iteration. Of the different algorithms studied for to optimize this problem, the Levenberg-Marquardt performed gave the best performance in terms of cpu time and in terms of number of iterations.

4.2.4 Results

The loss function as a function of the iteration number can be found in Figure 4.8:

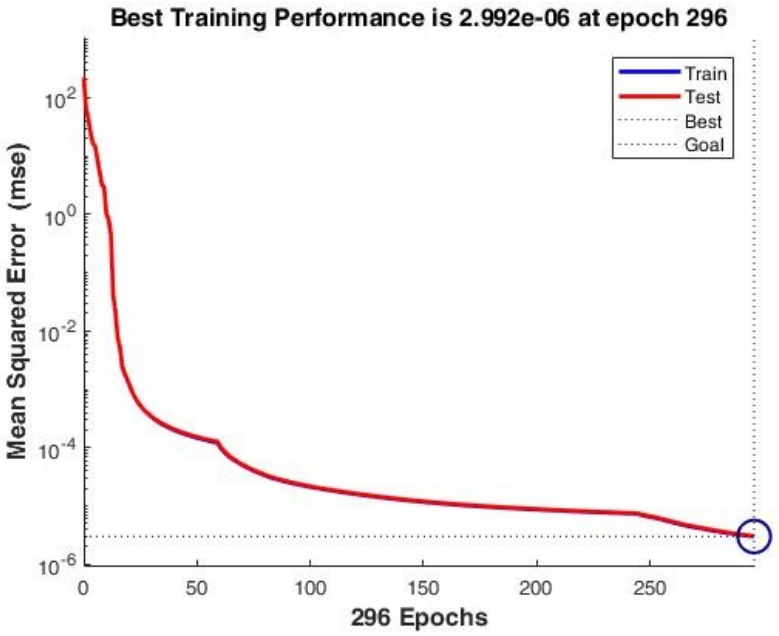

Figure 4.8: NH_3 loss function during the optimization procedure

Of several architechtures studied, the best performance was found to be of 6 layers and

12 neurons each. This consists of a total of 787 parameters to be fitted. The prediction of the ammonia source rate is shown in Figure 4.9, where the lines show a deviation of +/- 5%.

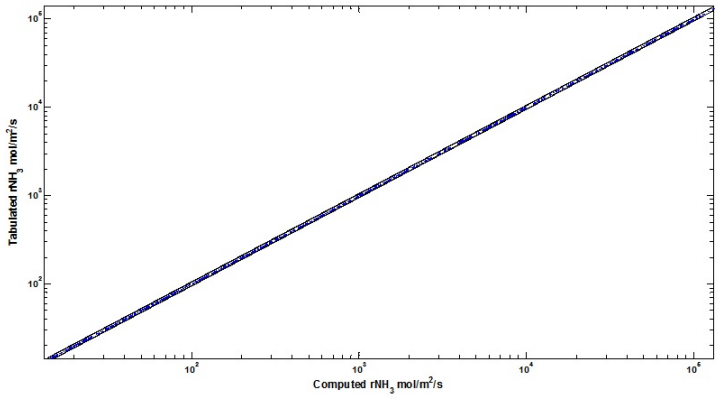

Figure 4.9: Neural network ammonia oxidation predicted rate

Figure 4.10 shows the error distribution of the ammonia oxidation rate.

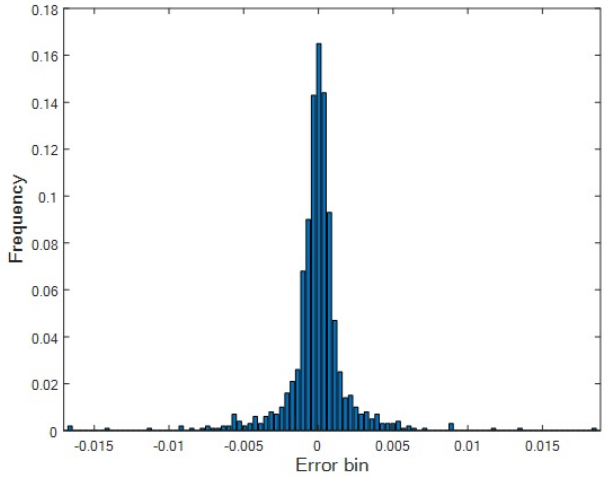

Figure 4.10: Relative error distribution ammonia oxidation predicted rate

The largest error are found to be bounded under 2%. Most of the errors lie within 0.5%. As for the performance of the net, the average error is of 0.12%. The average time to retrieve a rate from the network is of 0.003 ms and the size of the network with this architecture is of 6.3 kB.

Similar computations were performed for the selectivity of N_2O. N_2 was not calculated due to its known low selectivity.

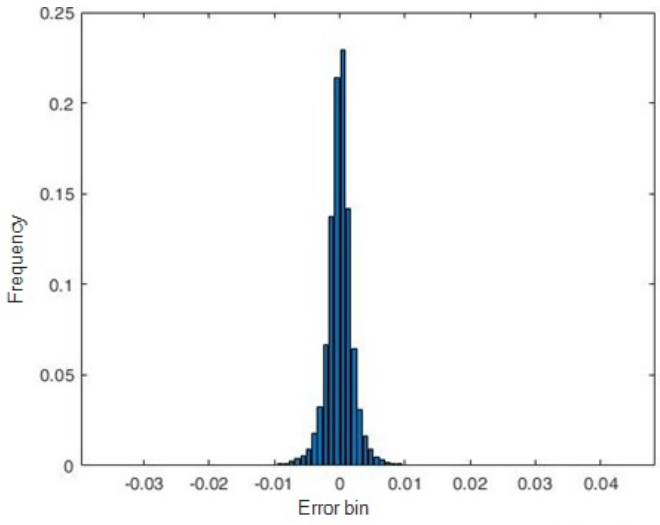

Figure 4.11: Relative error distribution for the N_2O selectivity. Number of parameters = 787

In Figure 4.11 the histogram of the errors of the predicted selectivities is shown. It can be seen that the maximum errors are bounded to +/- 4% and that the majority of the errors lie within +/- 1%. This shows that in terms of accuracy, both tables can be combined to predict the reaction rates and selectivities for the same parameter range of the lookup table, and with fewer paramters.

4.2.5 Conclusions

In this section the use of Neural Networks for data precomputation was investigated, using the ammonia oxidation case. The expected advantages are the use of a non-cartesian grid, which could prevent the storage of non feasible data. It was found that for the ammonia oxidation source rate there is an architecture that can predict well the rate of adsorption of ammonia. When testing the errors, they are bounded to 2%. Most of the errors are within 0.5% and the average error is of 0.12%. The information retrieval was faster than any of the lookup tables studied in the previous section, being of 0.003 ms, being faster by a factor

of almost 100x compared to the lookup tables. The memory usage was less intense. The Neural Network approach used 6.3kB, compared to 12 MB for a table of similar error. The selectivity towards N_2O can be computed similarly with a maximum error of 4%, and with the majority of the error being bounded between +/- 1%.

Chapter 5

Study of N_2O formation on Pt wires

5.1 Introduction

Ammonia oxidation is one of the steps in the production of nitric acid, being a process older than a hundred years old to current date since Ostwald patented his process [52]. The catalytic oxidation of ammonia was known from before that date, and was developed at industrial scale in the 1920s [48].

The main reactions are:

$$4\,NH_3 + 5\,O_2 \longrightarrow 4\,NO + 6\,H_2O$$
$$4\,NH_3 + 3\,O_2 \longrightarrow 2\,N_2 + 6\,H_2O$$
$$4\,NH_3 + 4\,O_2 \longrightarrow 2\,N_2O + 6\,H_2O$$

Minor modifications followed the Ostwald process. The most significant improvement was the use of Pt-Rh alloy gauze, where of 5%-10 % of the catalyst is comprised of the latter. This optimizes the process by giving good conversion, while limiting the precious metal losses [28] and has been wideley studied [49]. Additionally, this metal alloy increases the yield towards NO [28, 29]. The Ostwald process requires an ammonia source, which became available at an industrial scale in the same period of time that the Ostwald process was developed thanks to the discoveries of Haber of the catalytic synthesis of ammonia from from nitrogen contained in the air and hydrogen, which in turn meant the independence

from the use of saltpetre to produce nitric acid. Alternative methods to produce NO existed, which oxidized directly the nitrogen from air, however, compared to the Ostwald process, much more energy was required per mass of product [34]. The combination of Haber-Bosch and Ostwald process were remarkable for being the first which had an economically feasible energy consumption per kg of produced nitric acid, and it is still used today with minor modifications. Currently this compound is amongst the top 10 produced chemicals in the world [29]. The product finds applications in the manufacturing of fertilizer and explosives, among several others uses [56].

Despite the long standing knowledge of the process in the industry, there are still aspects that are not known about it, and are still far from being understood [51]. A very important one is the correct chemical mechanism to describe the heterogeneous combustion. Thanks to current advances, several mechanisms are available which can describe with accuracy to a certain extent the observed reaction rates. However, much more is needed to have full understanding.

One method of calculating the reaction kinetics is done by the use of Langmuir-Hinshelwood or Hougen-Watson assumptions, in which a mechanism is proposed, and an assumption is made with respect of one of the reactions, assuming all of the others are in equilibrium. This is the approach taken by [58], who used a L-H reaction type to predict the reaction rate of NH_3 on polycrystalline Pt. They consider competition for adsorption sites between NH_3 and NO. More recently, [74] approached the same problem using a L-H assumption, and comparing against experiments.

On the other hand, detailed mechanisms are harder to obtain, due to several complications in measuring key variables over the course of the reaction due to fast reaction times, and extreme operating conditions, among others. However, if they represent well the reality at a reaction level, they could be a very good tool to extrapolate, which helps to perform numerical design experiments. The level of detail of a detailed mechanism can be overwhelming and certain intermediates may be hard to measure, therefore the researcher interested in detailed chemistry modeling faces a compromise regarding level of detail and

access of information on intermediates [18].

One study worth noting is [4] in which the ammonia oxidation was studied over a Pt surface under a wide range of temperature and pressures. Pathways of production of N_2O are discussed. [31] studied the process of ammonia oxidation using a combination of experimental and computational methods. Later on a mechanism developed by [40], showed the oxidation of ammonia over polycrystalline Pt based on experiments. They found a model which adjusted relatively well for the production of NO and N_2O. [48] took a different approach, using DFT of Pt(100) faces to determine kinetic parameters of ammonia oxidation. [57] used a DFT approach to study the activation energies of the mechanism. More recently [24] explored further the studies with DFT calculations.

It is known from reactor operation that byproducts are produced, most relevantly nitrous oxide, also known as laughing gas, which has gained attention recently especially due to its contribution as a greenhouse gas, being 298 times stronger than that of CO_2 on a mass basis. It also has an impact on the atmospheric chemistries of NO and in ozone [56]. The reaction is set to occur on wire gauzes, most commonly made of Pt/10 % Rh. This configuration is beneficial due to its low pressure drop, and it takes advantage of the short contact times required. Other processes use gauzes as well for similar reasons, for example in the HCN manufacturing process, the Andrussow process [73]. Due to these widespread applications, the gauze itself has been the subject of different studies [37, 38, 39]. It has been known that the gauze's wire configuration has an effect on the performance of the reactor [56], and further industrial observations confirm it [70].

Despite the long usage of the ammonia oxidation reactor, few publications exist about them and to the best of the author's knowledge, there are not any about coupling the transport phenomena and detailed surface mechanism under industrial operating conditions. Noteworthy related publications are the kinetic mechanism studies, as mentioned before. On the reactor study, a model using an adjusted global mechanism was developed by [30]. This model does not account for the flow and temperature profiles within the reactor. Another publication by [3] included these effects on an industrial scale ammonia oxidation reactor.

However, they did not include the reactions into the model. Moreover, the specifics of the reactor besides its dimensions were not reported. Worthwhile is to mention the catalytic partial oxidation of methane performed first by [15]. Another similar study worthwhile to mention is the work performed by [62], who modeled the catalytic partial oxidation of methane on a gauze reactor, including surface chemistry and gas phase chemistry using CFD to account for transport phenomena.

The study of the selectivity of N_2O in the ammonia combustion process is the main topic of this chapter. We study the effect numerically using CFD, and include a detailed kinetic mechanism, investigating the causes behind the creation of this compound under industrial process conditions.

5.2 Computational model

Let us consider for illustration purposes a simple domain. We take a two dimensional cross section of a single cylindrical wire surrounded by a following gas, as shown in Figure 5.1.

In this instance the solution domain consists of the fluid phase, the flowing gas, and the solid phase, the metal wire. It is necessary to consider the wire as part of the domain, to account for the conduction of heat through it. To analyse this system it is necessary to solve the conseration equations for species, energy and momentum. The conservation equation and associated boundary conditions are given in the following section.

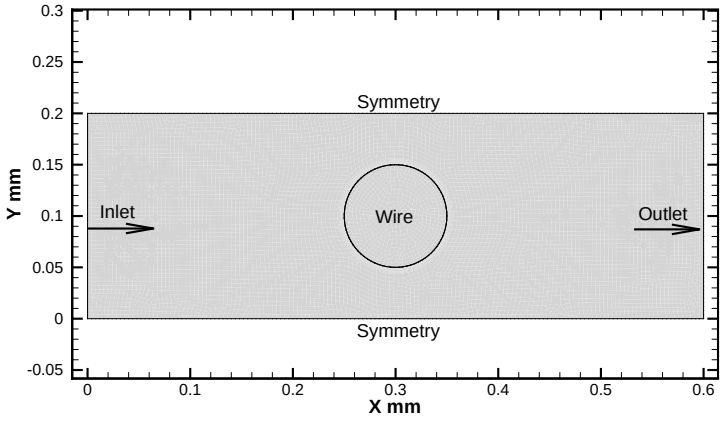

(a) Domain

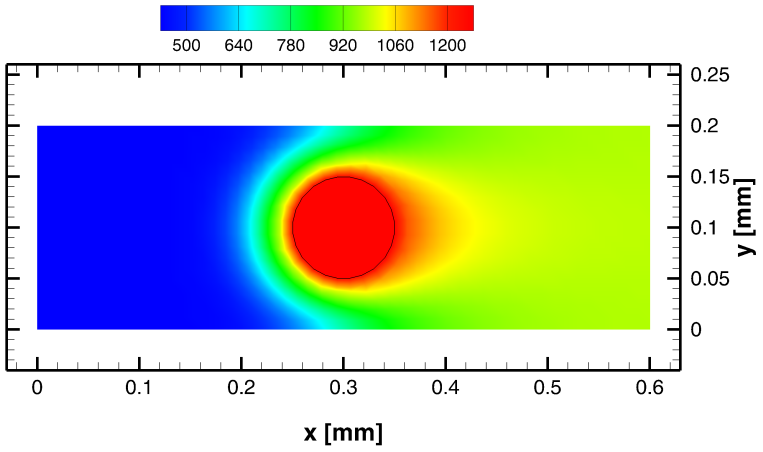

(b) Solution showing the temperature profile

Figure 5.1: Representative 2D geometry for wire diameter of 100 μm. Inlet, outlet and symmetry boundary conditions are shown. The domain height is represented as S, meaning the separation between wire centres along the y axis.

5.2.1 Conservation equations

On the domain shown in Figure 5.1, the following conservation equations can be applied. In this section the same conservation equations shown in the theory section, Chapter 3 are used. The thermodynamical and transport properties are provided Appendix of Chapter 4. In addition, the radiation is modelled as well, which is described as follows:

Radiation model The radiation effects were modelled using two alternatives: the Surface to Surface (S2S) model, which neglects the participation of radiation in the media, and only accounts for radiation of surfaces; and the second model we considered was the Discrete Ordinates (DO) model. Both models gave similar results with maximum wire temperature differences of 0.2 %. All the results shown are with the S2S model. This model assumes that the participating surfaces are diffuse, so that their transmittance $\tau = 0$. Therefore, each surface can either absorb a fraction of the energy α or reflect a fraction of the energy ρ. The general radiative energy conservation equation $\alpha = \tau + \rho$ reduces to $\epsilon = \rho$ for this model, since $\tau = 0$ and the emissivity is the same as the absorptivity by Kirchoff's law.

The method is based on the calculation of view factors which are then used to calculate the radiosity of the participating surfaces. We consider as participating surfaces only the inlet at the prescribed boundary condition temperature, the outlet, at the computed temperature, and the wires at their temperatures. The emissivity of all relevant surfaces were set to 1. The equations that describe the radiation are presented as follows:

The energy reflected from surface k is [2]:

$$q_{out,k} = \epsilon_k \sigma T_k^4 + \rho_k q_{in,k} \tag{5.1}$$

where q is the energy flux leaving surface k, ϵ_k is the emmisivity of surface k, T_k is the temperature of surface k, ρ_k is the reflected fraction of incident radiative flux on surface k, and $q_{in,k}$ is the incident radiative flux on surface k. The radiosity of every pair of surfaces k,j is related to their view factor $F_{k,j}$, which represents the fraction of energy leaving the surface k that is incident to surface j.

Therefore, the incident energy can be computed as [2]:

$$A_k q_{in,k} = \sum_{j=1}^{N} A_j q_{out,j} F_{j,k} \tag{5.2}$$

where A_k and A_j are the areas of the emmiting surface, and the receiver surface respectively. Considering the view factor relationship: $A_j F_{j,k} = A_k F_{k,j}$, then [2]:

$$A_k q_{in,k} = \sum_{j=1}^{N} F_{k,j} q_{out,j} \tag{5.3}$$

Upon substitution into Equation 5.1, the radiosity of surface k can be computed as [2]:

$$J_k = \epsilon_k \sigma T_k^4 + \rho_k \sum_{j=1}^{N} F_{k,j} J_j \tag{5.4}$$

The view factors are computed as [2]:

$$F_{i,j} = \frac{1}{A_i} \int_{Ai} \int_{A_j} \frac{\cos\theta_i \cos\theta_j}{\pi r^2} \delta_{ij} dA_i dA_j \tag{5.5}$$

where $d_{ij} = 1$ if the surface i sees surface j, or 0 if surface i does not see surface j.

All other surfaces present in the study not mentioned above are set to symmetry, which consider no heat flux across those boundaries, either in the fluid phase, or solid phase.

5.2.2 Boundary conditions

For every inlet we impose a velocity inlet, for every outlet we impose a pressure outlet. For the walls we impose symmetry. The boundary conditions at the wire surface are described now. The wire surface is modeled as no-slip for fluid flow. No thermal boundary condition is needed for the fluid, because the solid-fluid problem is modeled as conjugated heat transfer. The boundary condition for the wire surface includes the source term accounting for the heat of reaction. For species source terms, we used a modified version of the ammonia oxidation mechanism proposed by [40] with surface density of $\Gamma = 2.72 \cdot 10^{-5}\ mol/m^2$ [62] for both active sites. The surface rates are integrated over time until steady state is obtained [35],

which gives the surface coverages of the species, with which the reaction source terms can be computed. The net source terms for each species are expressed as:

$$\frac{d\Theta_i}{dt} = \frac{\dot{s}_i}{\Gamma} \rightarrow 0 \tag{5.6}$$

where i refers to the adsorbed species i and s is the net source term of adsorbed species i. Once in steady state, the surface concentrations of the adsorbed species can be found, and used to calculate the net source terms of the gas phase species. These source terms are coupled with the boundary conditions on the wire. First, the species flux boundary conditions is presented in Equation (6.2) ([32]):

$$-D_{im}\frac{\partial C_i}{\partial n}|_{wire} = \dot{s}_i \tag{5.7}$$

The thermal boundary condition is given by the net difference of enthalpy of formation on the surface for each of the reactions, which in steady state is equals to the heat flux from the surface to the flow:

$$-k_s\frac{\partial T_f}{\partial n}|_{wire,in} - k_f\frac{\partial T_f}{\partial n}|_{wire} = \sum_j \Delta H_{R,j}\dot{s}_j \tag{5.8}$$

j runs for each of the products NO, N_2O and N_2, k_f is the thermal conductivity of the fluid and $\Delta H_{R,j}$ is the heat of reaction of species j.

5.2.3 Numerical considerations

Mesh studies to guarantee a mesh independent solution were performed. An inflation layer with sufficient layers is necessary to capture the strong gradients found close to the wire. In this study we use 15, with smooth transition parameter of 1.2. The number of elements on the wire surface was parameterized, so that a mesh independent number was found. It was found that the number of surface elements needed to describe the Nusselt number with 0.12% error with is N=60, which was found sufficient for this study. Surface cells are related to chemistry calls, hence, the time per iteration increases with the number

of surface cells. The equation for the final solutions reported here are discretized with third order MUSCL scheme for all variables with the exception of the pressure, which is discretized using the standard discretization. The SIMPLE scheme was used for pressure coupling. The criteria for convergence consisted of having all residuals below 10^{-9} and additionally having stabilized wire temperature, heat, drag, and amount of N_2O at the outlet. All the simulations presented here were performed with Ansys Fluent 17.2 on a Windows 7 Machine, with hardware Intel i7-3820 and 64GB of RAM.

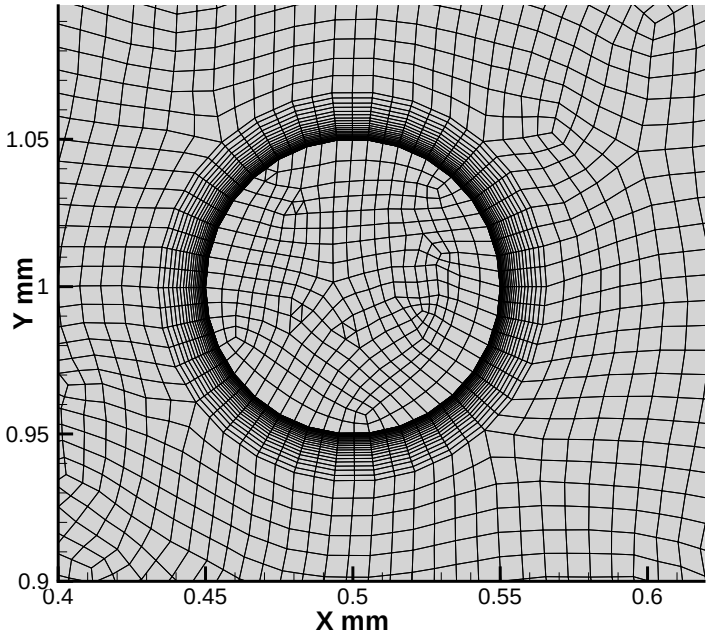

Figure 5.2: Close up of the mesh around the wire of diameter 100 μm and 60 cells on the boundary

5.3 Results and discussion

In this section we present a systematic study of the selectivity. Several experiments were performed. We will refer to conversion and integral and differential selectivities, defined as:

$$X = 1 - \frac{F_{NH_3}}{F_{NH_{3,0}}} \tag{5.9}$$

where X is the conversion, and $F_{NH_{3,0}}$ and F_{NH_3} are the inlet and outlet molar flow rates of ammonia, respectively.

The integral selectivities is defined in Equation (5.10):

$$S_{i,i} = \frac{\nu_i}{\nu_{NH_3}} \cdot \frac{F_{i,0} - F_i}{F_{NH_3,0} - F_{NH_3}} \tag{5.10}$$

where ν_i are the stoichiometric coefficients. The differential selectivity is defined as:

$$S_{i,d} = \frac{\nu_i}{\nu_{NH_3}} \cdot \frac{R_i}{R_{NH_3}} \tag{5.11}$$

5.3.1 2D without wire to wire interaction

Considering that the Reynolds number for this study is always well under 200, whether it is defined based on film properties, bulk properties, or surface properties, it is possible to consider the flow around a single wire as a 2D flow [43]. We separate the studies in the domains and test performed. First, we explore a single wire in 2D with a large domain compared to the wire 20 wire diameters along the y axis, and 10 wire diameters from the wire center to the outlet. This ensures that the heat flux measured by the Nusselt number is within 0.15% of the boundary independent domain, which was calculated as the value where the domain is large enough, so that no further change can be seen. The values for a large domain in separation is S/D=160, the length is L/D = 40. Considering that many parameters may change independently, we define a base case with the following boundary conditions for the inlet:

Table 5.1: Base case parameters

parameter	value
inlet velocity m/s	0.75
Pressure bar	5
inlet temperature °C	150
xNH_3	0.10
xO_2	0.19
wire diameter μm	100
Re_∞ /Re_{wire}	10.6 / 2.0

Velocity field For the base case it was found that the velocity field around the single non-interacting wire is better described by the Reynolds number based on the wire diameter.

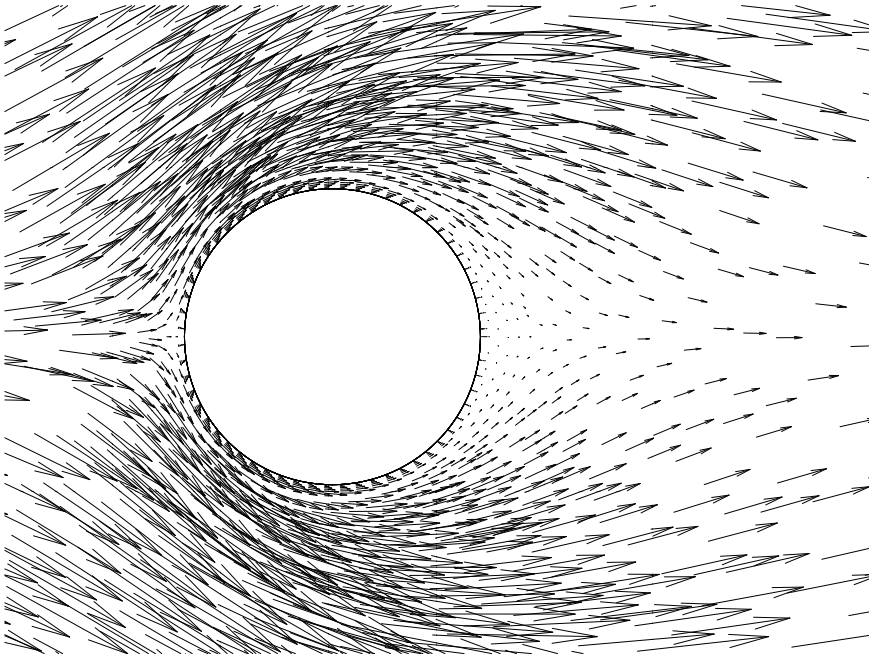

Figure 5.3: Close up of the velocity vector field around the wire. D=100 μm, $Re_{bulk} = 10.6$

In Figure 5.3 it can be seen that the vector field does not show any boundary layer separation nor recirculation on the back of the wire. This is despite the $Re_\infty = 10.6$. This is due to the temperature gradient between the bulk and the surface, so that the properties evaluated at the bulk conditions do not predict the flow field around the wire. The flow field found here, without boundary layer separation is better described by a Re<5 compared to

the findings of [43], so that for this study Re_{wire} is considered to be the better predictor of the flow field around the wire. For all of the parameters used in this study, it was found that the flow around the cylinder is steady and the boundary layer does not detach.

Effect of wire diameter The wire diameter was varied to observe if it induced an effect on the selectivities, keeping every inlet boundary condition constant. Since we consider a large domain, there is no boundary placement effect, despite changing the size of the wire.

Table 5.2: Conversion, N_2O selectivity and wire temperature for different wire diameters

Diam μm	X %	N_2O sel %	wire temp K
50	3.8	1.44	1229.3
75	4.4	1.22	1229.6
100	5.0	1.10	1229.6
125	5.5	1.02	1229.5

Table 5.2 shows that the modification of the wire diameter under the base case parameters, changes the conversion, as expected due to the decreased exposed area. However, there is also a noticeable change in the selectivity to N_2O as well. The selectivity difference cannot be explained by a difference of wire temperatures, because they are almost the same. The chemical mechanism has only as input parameters the temperature and partial pressures of ammonia, oxygen and nitrogen oxide. Because of this, we study how the variation of these quantities on the surface of the wire.

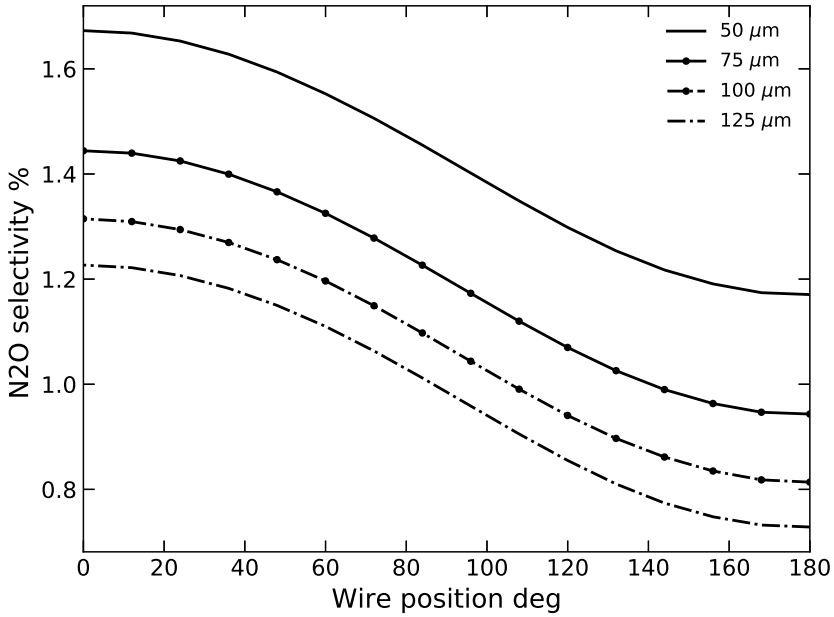

Figure 5.4: Differential selectivity as a function of the position in the wire for a large domain for different wire diameters

Figure 5.4 shows the local selectivity as a function of the wire position. Angle 0 means the front of the wire, and angle 180 is the back of the wire. An inverse relationship between wire diameter and selectivity is found, as shown in Table 5.2. This change is not a function of the position, since reducing the diamenter simply shifts the curve. Secondly, it is found that the selectivity is the highest at the front of the wire. To explain the selectivity change seen in Figure 5.4 there must be a quantity of the chemistry changing on the surface of the wire with the wire diameter. The wire temperature is essentially the same for every case as seen in Table 5.2, so therefore is either the concentration of ammonia, nitrogen oxide or oxygen is changing on the surface.

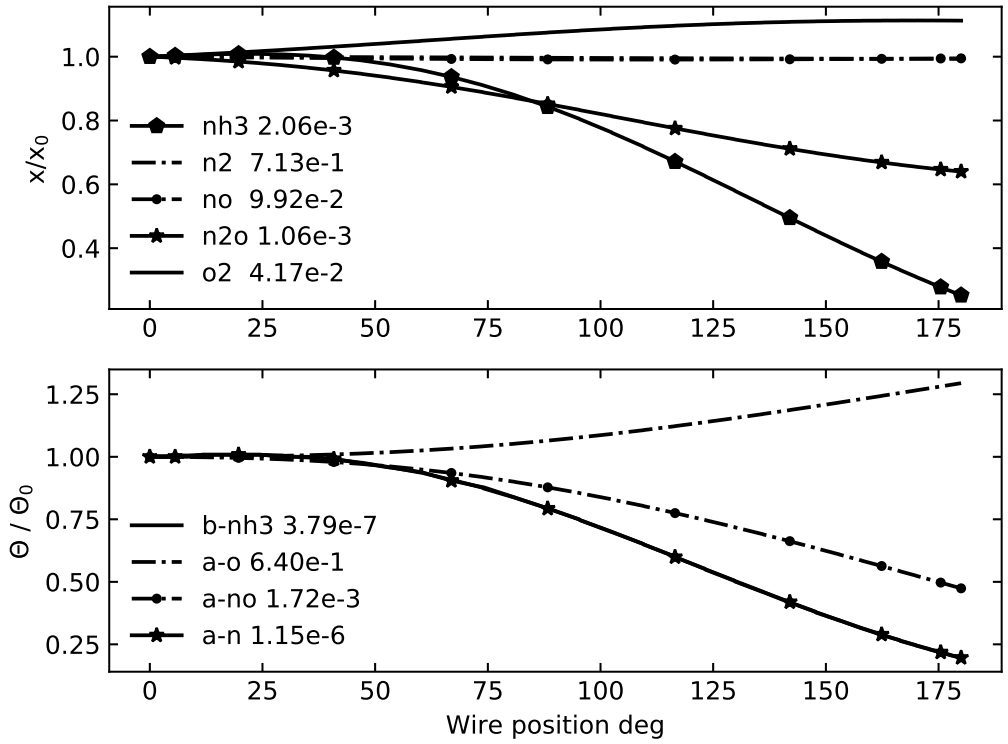

Figure 5.5: Surface conditions from laminar simulations. Mole fraction relative to the one at angle 0 (top) and surface coverages relative to the one at angle 0 (bottom) for the base case conditions, S/D = 20, L/D = 10

Figure 5.5 shows the mole fractions and surface coverages for the base case expressed relatively to the ones found in the front of the wire. The first finding is the null change of the mole fraction of N_2 which is expected as the net production of nitrogen is neglegible for this mechanism. It also can be seen that the mole fraction of NO is not a strong function of the wire position. However, the surface coverage of NO decreases with respect to the angle. This can be explained by the reduction of the surface mol fraction of NH_3 due to the reaction. Therefore, the a-NO coverage depends mainly on the position due to the surface concentration of ammonia, which can explain the selectivity towards N_2O seen in Figure 5.4. The mole fraction of oxygen increases as a function of the position, and the same is true for the surface coverage of the sites a-O, which is explained by a decreased reaction

rate due to the consumption of ammonia, leaving more oxygen available, and allowing a sites to adsorb more oxygen. This in turn blocks the adsorption of NO, and it seems that the available a sites prefer the adorption of oxygen blocking the adsorption of NO. With respect to the b sites, the surface coverage of ammonia on b sites is very low due possibly to the high temperature of the wire. However, it is possible to observe that the the coverage dependens on the position in the same manner as the coverages of nitrogen on a sites is.

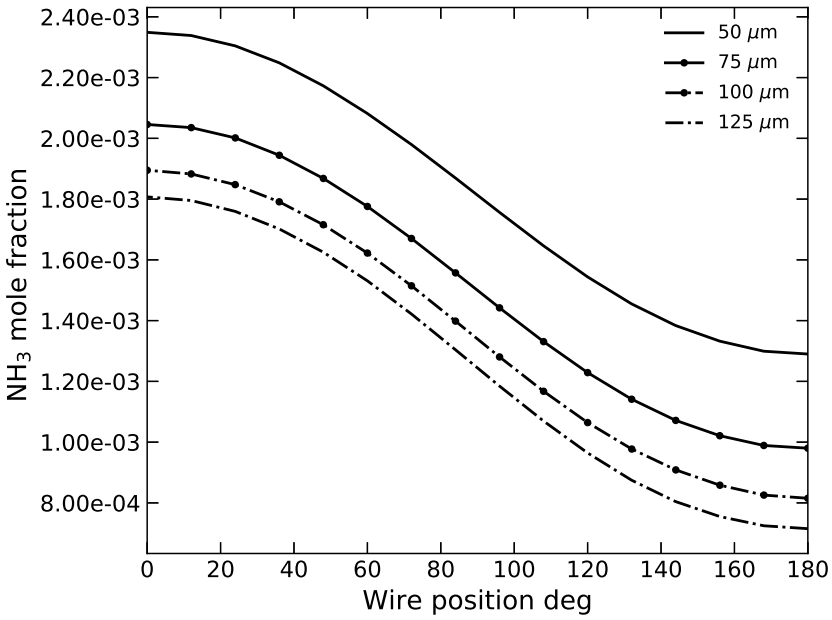

Figure 5.6: Ammonia mole fraction as a function of the position in the wire for a large domain for different wire diameters

Figure 5.6 shows a close match between the selectivity to N_2O and the mole fraction of ammonia on the surface. From the mechanism it is suspected that the surface coverage of NO is increased by the increase of concentration of ammonia on the surface, which in turn leads to a greater rate of production of N_2O. This is a consequence of the varying fluid field around the wire.

Effect of inlet velocity In the previous paragraph we mentioned the effect the selectivity due to changing the wire diameter and we proposed that it is due to changing the flow field around the wire, since the wire temperature was the same. Following the same logic, we

expect an effect on the selectivity when changing the inlet velocity.

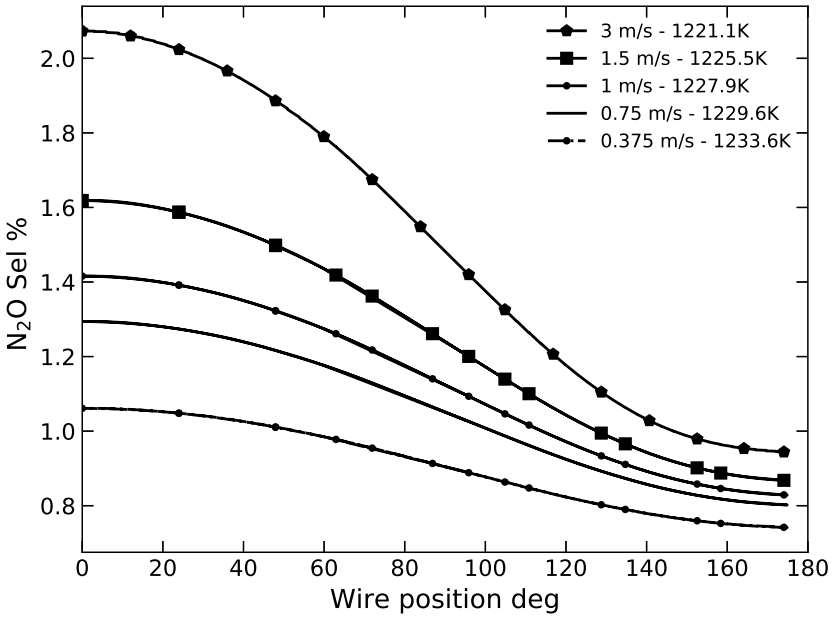

Figure 5.7: Base case wire differential selectivity to N_2O as a function of the position in the wire for a large domain for different velocities. S/D = 20, L/D = 10

In Figure 5.7 we observe that the selectivity depends strongly on the inlet velocity. This effect is stronger on the side facing the inlet, which is angle 0 to 90. After that we observe that the effect is less important. This can be explained by what was observed in the previous section, by the varying flow field around the wire. However, in this case there is the combined effect of varying the wire temperature as well. At higher velocities lower wire temperatures were found, which affects also the selectivity around the wire.

Effect of inlet temperature It is known that the selectivity depends strongly on the wire temperature. At higher temperatures, lower selectivities to N_2O are expected, and higher to NO. We study how the inlet temperature affects the wire temperature and the selectivity, which is an important variable to account for in an industrial operation setup. The results are shown in Table 5.3.

Table 5.3: Conversion, N_2O selectivity and wire temperature for different inlet temperature at constant mass flow. S/D=20 L/D =10

Temp ° C	X %	N_2O sel %	wire temp K
100	4.8	1.40	1186.8
150	5.0	1.10	1229.6
200	5.1	0.90	1272.8
250	5.3	0.74	1308.3

It can be seen that an increase of the temperature leads naturally to hotter wires. This in turn leads to a lower selectivity to nitrous oxide. This effects holds accounting for the velocity change so that the mass flow is constant.

Effect of inlet composition From the previous studies we know that the selectivity is affected by the ammonia mole fraction on the wire surface. We expect a positive correlation between selectivity and ammonia mole fraction at the inlet if the wire temperature were unchanged by changing the ammonia mole fraction at the inlet. In this section we study how the inlet composition affects the selectivity.

In Table 5.4 we observe the effect of varying the ammonia composition at the inlet. The mass flow rate was kept constant, so that the Reynolds number was the same for every calculation. As shown previously, the N_2O selectivity is a strong function of the wire temperature, and the results shown in Table 5.4 can be explained only by a concentration effect.

Table 5.4: Conversion, N_2O selectivity at fixed wire temperature and constant mass flow rate as a function of ammonia inlet composition

xNH_3 %	Tin °C	X %	N_2O sel %	wire temp K
4	638.0	6.2	0.14	1229.6
7	398.5	5.6	0.41	1229.6
10	150.0	5.0	1.10	1229.6
11.5	17.0	7.4	2.58	1229.6

Table 5.4 shows that an increase in the mole fraction at the inlet leads to an increase in

the selectivity towards N_2O, while keeping the mass fraction of oxygen at the inlet constant, and the wire temperature constant as well. This finding reinforces the idea of the direct connection between ammonia and N_2O selectivity.

5.3.2 2D with wire to wire effect

Effect of wire separation and radiation We now study the effect of including more wires into the domain. In 2D one way to approach this is by using symmetry boundary conditions on a smaller domain. The width of the domain represents the separation of the wires. The width is defined as the distance between the wire centers, in diameters. Our base case is defined as 2D, keeping all other parameters of the base case the same.

So far we have neglected the effect of radiation in the energy conservation equation. Considering the high temperatures involved and the strong temperature gradients, radiation is expect to be a relevant mechanism for heat transfer. Since the selectivity is strongly affected by the wire surface temperature, we expect the radiation to be relevant, which effect is shown in Table 5.5.

sep D	Conv %	N_2O sel %	wire temp K
	w/o - with	w/o - with	w/o - with
1.5	90.2 - 89.9	2.25 - 2.67	1143 - 1116
2	68.9 - 68.2	1.66 - 2.17	1186 - 1141
3	41.7 - 40.9	1.35 - 1.98	1227 - 1146
4	29.0 - 28.4	1.26 - 1.96	1218 - 1142

Table 5.5: Conversion, N_2O selectivity and wire temperature for different vertical wire separation. Single wire domain.

sep D	Conv %	N_2O sel %	wire temp K
1.5	90.2	2.25	1143
2	69.8	1.67	1187
2.5	53.5	1.44	1210
3	42.4	1.33	1219
4	29.5	1.24	1225
5	22.5	1.19	1227

Table 5.5 shows the effect of the wire distance in the y axis measured from wire centers on the wire temperature and selectivities. Since separating the wires increases the open area, the overall conversion decreases. More relevant is to observe the effect on N_2O selectivity. Here we find that increasing the separation, the selectivity decreases, whilst the wire temperature increases. This can be the main driver to the change in selectivity.

5.3.3 2D stacked wires

Here we consider a set of 10 wires stacked, representing a 10 layer gauze of Pt catalyts so that we study if there is any flow effect on the selectivity by the obstructions. The spacing in the x direction and in the y direction is of one diameter, measured from the centre of the wires.

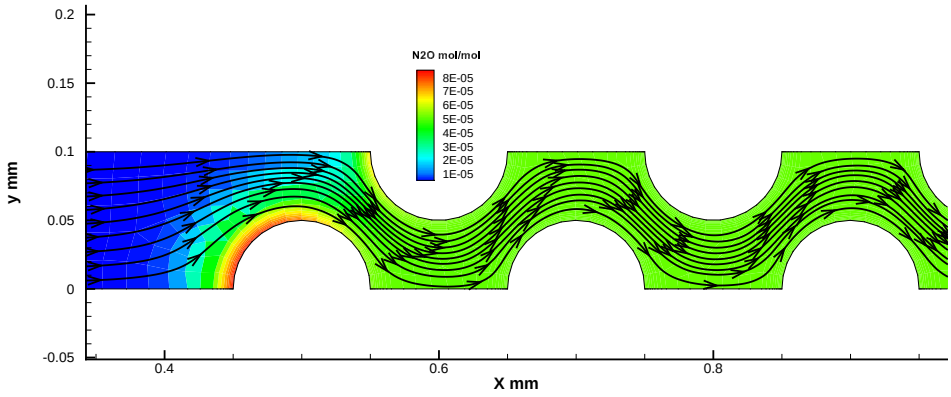

Figure 5.8: N_2O mole fraction in the multiple wires case

Figure 5.8 shows the 2D geometry under consideration, with the wire distribution. Here we are looking for an effect of flow on the wire selectivity. From the findings of the previous section, we consider important to include radiation in the model. We repeat the experiment without radiation as well. Here we observe the highest concentration of N_2O in front of wire 1, in an area of high streamline curvature. This is consistent with the findings of the previous sections. In Figure 5.11 we study the local selectivity around the first 4 wires.

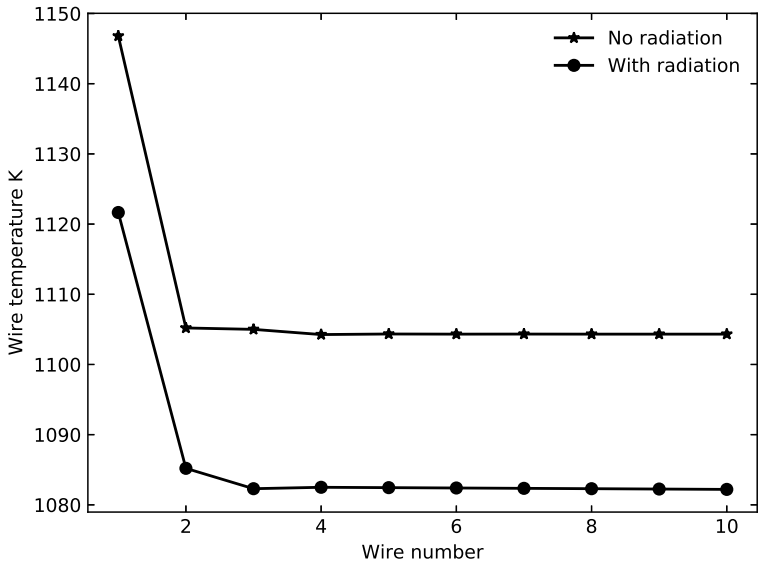

Figure 5.9: Wire temperature vs wire number with and without radiation.

Figure 5.9 shows the wire temperature profile across a the gauze pack of 10 wires shown in Figure 5.8. The highest temperature in both cases is found in the first layer. Without including radiation, the first layer temperature is at $T_1 = 1146.8$ K. The second layer has a significantly lower temperature, at $T_2 = 1105.2$ K. The third layer shows a slight increment of temperature at $T_3 = 1105.0$ K, after which, only minor variations are found. This plateau corresponds to the adiabatic temperature increase associated with a conversion of 100 %. Figure 5.10 shows the temperature profile of the fluid and wires in the domain.

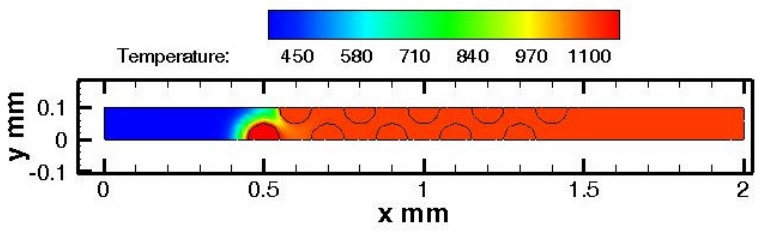

Figure 5.10: Wire temperature vs wire number without radiation.

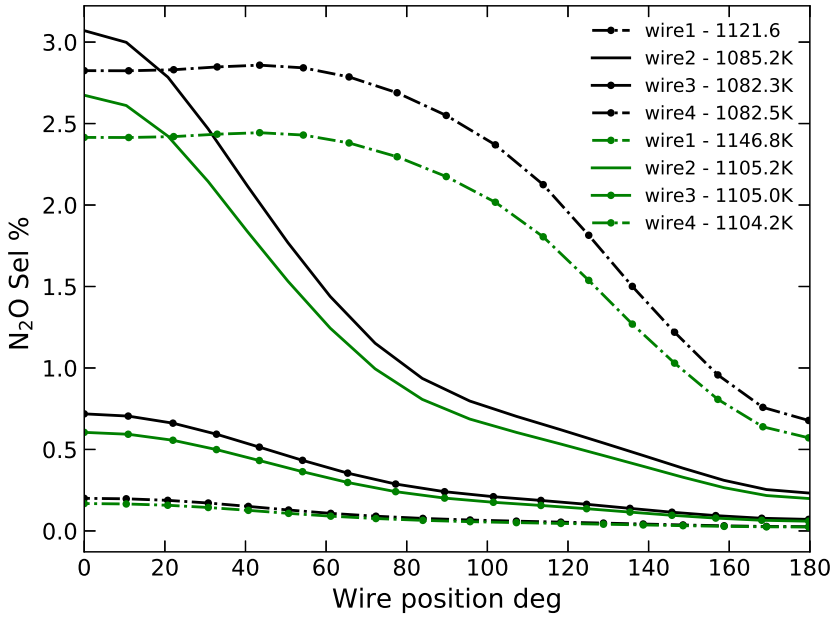

Figure 5.11: Differential selectivity around different wires. For the same wire, higher selectivity was obtained with radiation.

Figure 5.11 shows the differential selectivity for different wires. The same trend is observed with and without radiation. It is found that there is a local area of wire 2 that is more selective to N_2O than wire 1. This can be explained by either the lower temperature of wire 2 compared to wire 1, or by the concentration on the wire surface. To elucidate this effect, we fixed the temperatures of wires 1-5 at T=1121.6K and we study the differential selectivity of the different wires. The results are found in Figure 5.12.

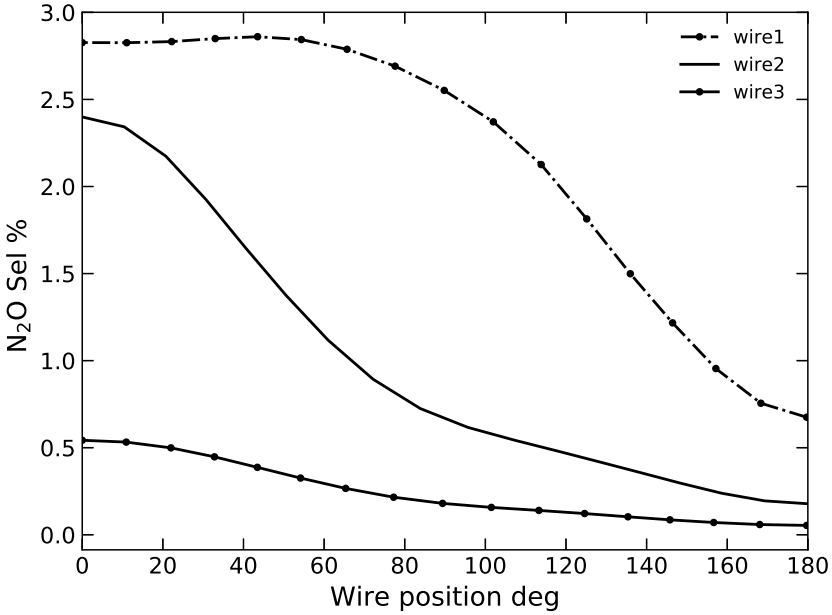

Figure 5.12: Differential selectivity around different wires at constant temperature.

From Figure 5.12 it can be observed that after fixing the temperature, the effect of increased selectivity disappears. We observe that the shape of the differential selectivity of wire 2 is preserved, however when fixing the temperature, it is shifted downwards. We conclude that the main driver of the increased selectivity found in Figure 5.11 is the lower temperature of the second wire.

5.3.4 3D studies

Simulation of a Pt net In this section we present a 3D simulation of a platinum gauze, with cartesian structure. The wire separation is 2D in each coordinate, and we use all base case inlet boundary conditions. We simulate the net with radiation. We reduced the size of the domain by using the symmetries. In this simulation we model only two layers of wires, shown in Figure 5.13.

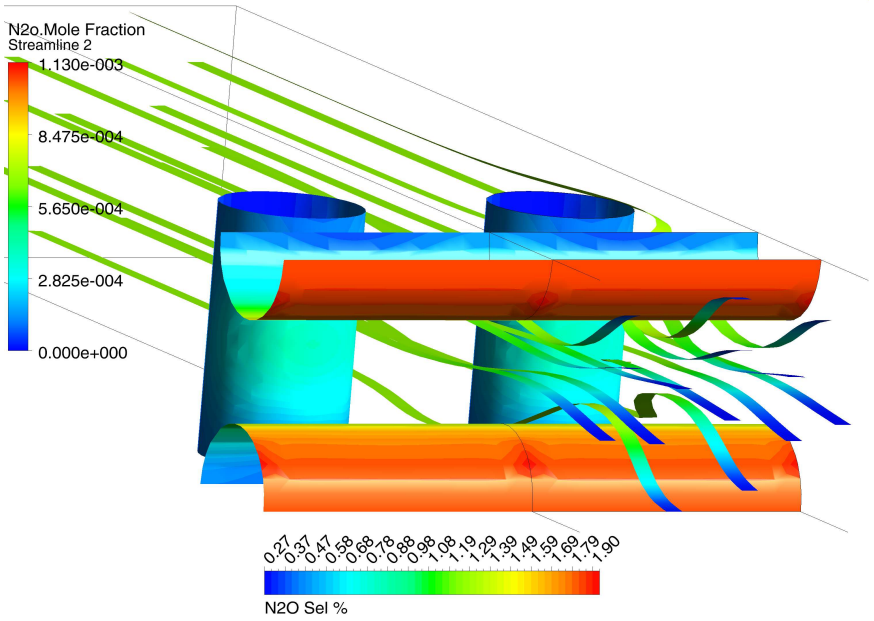

Figure 5.13: Contour of differential selectivity around different wires including radiation. Streamlines show fluid behaviour and N_2O mole fraction.

In this particular case we find that the highest N_2O selectivity is found on the first wire, with a maximum value of 1.9 %. This study shows the feasibility of studying transport phenomena on 3D shapes, which can be used to explore the effect of different mesh geometries on the NO yield.

5.4 Mass and heat transfer coefficients

Ammonia oxidation is a typical example of a diffusion limited reaction. Therefore, if the mass and heat transfer coefficients are known, and the usual assumption of neglegible concentration of ammonia on the wire surface is made, the reaction rate and the wire temperature can be computed by using mass and heat transfer coefficients. In this section the application of correlations is studied and it is compared with the experimental CFD results.

Some correlations have been postulated that model the mass and heat transfer coefficients of a cylinder in cross flow. A review of them is given in [5, 32]. As follows, correlations

for the average Nusselt Nu_m number are presented:

$$Nu_m = (0.376Re^{0.5} + 0.057Re^{2/3})Pr^{1/3} + 0.92[\ln(\frac{7.4055}{Re}) + 4.18Re]^{-1/3}Re^{1/3}Pr^{1/3} \quad (5.12)$$

$$Nu_m = (0.4Re^{1/2} + 0.06Re^{2/3})Pr^{0.4}(\frac{\mu_\infty}{\mu_0})^{1/4} \quad (5.13)$$

$$Nu_m = 0.3 + \frac{0.62Re^{0.5}Pr^{1/3}}{[1 + (\frac{0.4}{Pr})^{2/3}]^{0.25}}[1 + (\frac{Re}{282000})^{0.625}]^{0.8} \quad (5.14)$$

$$Nu_m = CRe^m Pr^{1/3} \quad (5.15)$$

Where Eq. 5.15 has the following parameters depending on the Reynolds number:

Re	C	m
$0.4 < \mathrm{Re} < 4$	0.989	0.330
$4 < \mathrm{Re} < 40$	0.911	0.385
$40 < \mathrm{Re} < 4000$	0.683	0.466
$4000 < \mathrm{Re} < 40000$	0.193	0.618
$40000 < \mathrm{Re} < 400000$	0.027	0.805

If the reaction is external diffusion limited, and the assumption of 0 concentration of ammonia on the surface is made, then the reaction rate can be written as:

$$r_{\mathrm{NH_3}} = \beta C_{\mathrm{NH_3},b} \quad (5.16)$$

where β is the mass transfer coefficient and can be computed by the correlations shown above combining its use with the heat and mass transfer analogy. The Schmidt number is defined as:

$$Sc = \frac{\mu}{\rho D_{AB}} \quad (5.17)$$

To use the heat and mass transfer analogy, the Pr number is replaced by the Sc number. The Sherwood number (Sh) can therefore provide a value of β as:

$$Sh = \frac{\beta L}{D_{\mathrm{NH_3}}} = \frac{\beta D}{D_{\mathrm{NH_3}}} \tag{5.18}$$

With this information, using the heat transfer coefficient h it is possible to obtain the wire temperature, as:

$$Q = \Delta_r H \cdot r_{\mathrm{NH_3}} = \Delta_r H \beta C_{\mathrm{NH_3}} = h(T_\infty - T_{wire}) \tag{5.19}$$

after manipulation:

$$T_{wire} = T_\infty - \Delta_R H \cdot Sh \frac{D_{air,\mathrm{NH_3}}}{D} C_{\mathrm{NH_3}} \frac{1}{h} \tag{5.20}$$

where h is the heat transfer coefficient, which can be computed using the Nusselt number as:

$$Nu = \frac{hD}{k} \tag{5.21}$$

substituting and manipulating:

$$T_{wire} = T_\infty - \Delta_R H \cdot \frac{Sh}{Nu} \frac{D_{\mathrm{NH_3}}}{k} C_{\mathrm{NH_3}} \tag{5.22}$$

The Fuller correlation can be used to compute the ammonia diffusivity in air:

$$D_{AB} = 0.001 \frac{T^{1.75} (\frac{1}{M_a} + \frac{1}{M_b})^{0.5}}{P[(\sum V_a)^{1/3} + \sum (V_b)^{1/3}]^2} \tag{5.23}$$

where P is the pressure in atmospheres, T is the temperature in K, M_i is the molecular mass of compound i in g/mol, and V are the atomic diffusion volumes. The values of the required parameters can be found in the appendix section of this chapter.

The following table shows all the properties evaluated at film, bulk and surface conditions

considering the temperature and composition:

Parameter	Value @film	Value @bulk	Value @surface
Density kg/m^3	2.43	3.56	1.29
Concentration mol/m^3	72.8	142.1	48.9
μ e5 Pa·s	3.76	2.53	4.99
heat conductivity k W/m/K	0.061	0.0387	0.0852
heat capacity c_p J/kg/K	1222.9	1120.5	1325.4
Diffusion coefficient $D_{air,\mathrm{NH_3}}$ m^2/s e5	3.62	1.02	6.22
Sc	0.659	0.697	0.622
Pr	0.754	0.733	0.776
Re	6.25	10.5	1.94
Le	0.88	0.95	0.80

From here, the correlations aforementioned can be used to obtain the Sh and the Nu numbers. The heat and mass transfer coefficients can be also computed from the simulations shown above. The results are shown in Table 5.6

Table 5.6: Correlation results for flow velocity of 0.75 m/s, T∞=423 K, P=5 bar, xNH_3=10%. Film concentration of NH_3 = 7.3 mol/m^3

Equation	Value @film	Value @bulk	Value @surface
Heat transfer Nu_m			
5.12	2.07	2.51	1.37
5.13	1.27	1.66	0.96
5.14	1.90	2.37	1.20
5.15	1.68	2.03	1.13
Mass Transfer Sh_m			
5.12	1.98	2.47	1.27
5.13	1.21	1.63	0.64
5.14	1.85	2.34	1.15
5.15	1.61	2.00	1.05
$\Delta_R H$ kJ/mol	-193.7	-217.2	-178.1
T_{wire} K Eq 5.12	1207.8	832.9	1297.9
T_{wire} K Eq 5.13	1200.8	831.6	1285.1
T_{wire} K Eq 5.14	1219.6	835.0	1324.7
T_{wire} K Eq 5.15	1207.8	832.9	1297.9

Considering that the wire temperature found with the simulations is of 1229.6 K, it can be seen that using the correlations is a good approximation to determine the wire

temperature without the use of CFD. However, it is important to remark the diference of about 10-20 K when using the values computed at film conditions, which in turn have an effect on the selectivity.

For completeness, it is possible to compute the Nu and Sh from the simulation by computing the heat and rate of reaction of ammonia from the solution. The results are shown in Table 5.7

Table 5.7: Correlation results from simulation for flow velocity of 0.75 m/s, T∞=423 K, P=5 bar, xNH_3=10%. T_{wire} = 1229.6 K, rNH_3 = 3.48 mol/s/m^2, q = 616,700 W/m^2. Wire diameter 100 μm

	Value @film	Value @bulk	Value @surface
Nu	1.23	1.97	0.90
Sh	1.34	4.69	0.77

As it can be seen, the correlations give fairly similar results to the values observed in the simulation. However, it is worth noting that the simulation provides a Sh>Nu, whereas the correlations provide the opposite result. The minimum error from a correlation to the experimental results is with 5.13, for either mass and heat transfer coefficients, with errors varying from 3.3% for heat tranfer, to 13% to mass transfer. As for the prediction of the wire temperature, the correlation 5.14 gives the best results, with an error of less than 10 K. Correlations 5.12 and 5.15 give the same results for wire tempeatures, however, the prediction of the Nu and Sh are different.

5.5 Mechanism sensitivity study

In this chapter the effect of the selectivity was studied by varying the operational conditions or design of the catalyst. This is of practical value because the operational conditions can be changed easily during the functioning of the plant. However, considering that the mechanism is known, it is also possible to obtain the sensitivities to the selectivity by varying the surface conditions, which are not easy to control, to observe which variable has the highest effect

on the selectivity. First of all, let us recall the definition of the N_2O selectivity as:

$$sel = -2\frac{r_{\mathrm{N_2O}}}{r_{\mathrm{NH_3}}} \tag{5.24}$$

It is known that the reaction rates are a function of the wire temperature T and the surface mole fractions xNH_3, xO_2 and xNO. Therefore sel = sel(T,x_i). It is then interesting to study which one of these parameters has the highest influence in the selectivity. For this, the sensitivity L with respect to NH_3 can be defined as:

$$L_{\mathrm{xNH_3}} = \frac{\partial sel(T, x_i)}{\partial_{\mathrm{xNH_3}}} \tag{5.25}$$

The sensitivity itself is then a function of T and x_i. To study the sensitivity then, a case is chosen. This is the single wire in a big domain presented in Section 5.3.1 with the following surface conditions:

Table 5.8: Surface conditions

parameter	value
T K	1229.6
xNH_3	2.06e-3
xO_2	4.17e-2
xNO	9.92e-2

The sensitivity is then calculated using second order central difference scheme:

$$f'(x) = \frac{x_{+h} - x_{-h}}{2h} \tag{5.26}$$

The parameter h is chosen arbitrarily at h = 0.001 for the species and h = 1K for the temperature.

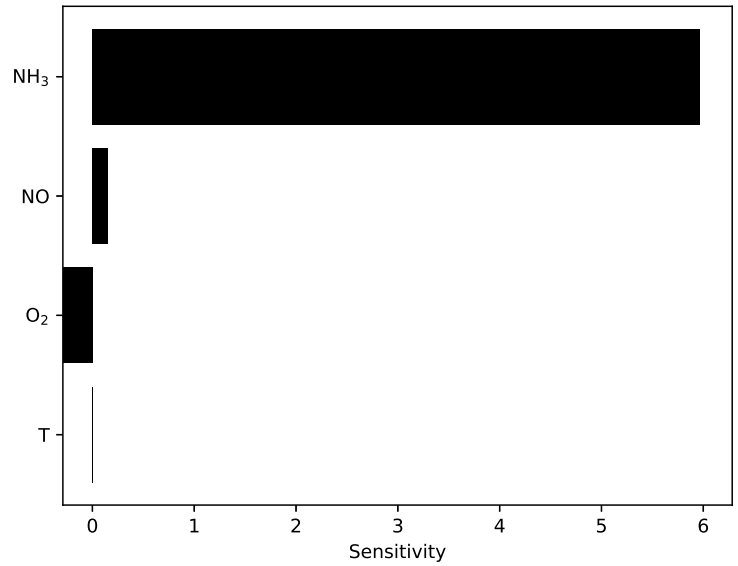

Figure 5.14: N_2O sensitivities to different wire surface conditions.

In Figure 5.14 the results are presented. It is clear that the most sensitive variable is the ammonia mole fraction on the surface, with a sensitivity value of almost 6. This means that an increase of 1% of mole fraction on the surface is reflected as an increase of 6% of selectivity towards N_2O. NO also affects the selectivity to N_2O, but in a much smaller proportion with a sensitivity value of 0.155. Oxygen interestingly has the opposite effect in terms of selectivity, with a sensitivity coefficient of -0.290. Finally the temperature T has also a negative sensitivity coefficient, although very small of -2.35e-8. The comparison of the sensitivity coefficients for species and temperature is not obvious due to the different value of h used. In this case, the small value found for the temperature can be explained due to the region where the sensitivity was calculated. Higher values of sensitivity are found at lower temperature regions. Therefore, in conclusion, the largest effect on selectivity in the region of study occurs due to the surface mole fraction of ammonia, and in a lesser sense, due to the mole fraction of nitric oxide. Oxygen and Temperature have a negative effect on the selectivity. Therefore, according to the mechanism, if the selectivity were to be minimized, the largest effect can be expected to be by obtaining a smaller ammonia mole

fraction on the catalyst surface.

If the sensitivity is only taken with respect to the largest actuator ammonia, then on the surface level it is possible to do the same sensitivity analysis for the surface coverages as:

$$L_{\theta_i} = \frac{\partial \theta_i}{\partial_{\mathrm{xNH_3}}} \tag{5.27}$$

which can help to explain why the selectivity changes at the surface level.

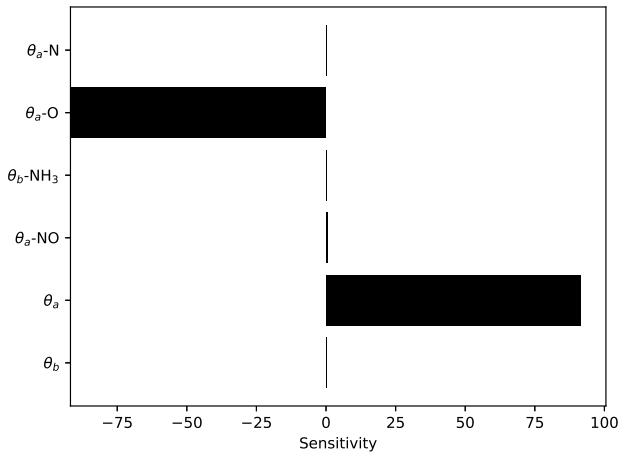

Figure 5.15: Surface coverage sensitivities to NH_3 mole fraction

Figure 5.15 shows the effect on the surface level of a variation on the surface mole fraction. It is found that an increase of mole fraction of ammonia affects largely the surface coverage of sites θ_a-O, by reducing it and hence they become free sites θ_a. Also, with a lower magnitude the surface coverage of θ_a-NO is also increased. The increase of the empty a site coverage θ_a then affects the adsorption reaction $\mathrm{NO} + \mathrm{a} \longrightarrow \mathrm{NO{-}a}$ reducing the net production rate in the gas phase of NO. The increase of surface coverage of θ_b-NO affects the reaction rate of $\mathrm{NO{-}a} + \mathrm{N{-}a} \longrightarrow \mathrm{N_2O} + 2\,\mathrm{a}$ increasing it and affecting positively the selectivity towards N_2O. The slight variation of surface coverages of the b sites shows that the net adsorption rate of ammonia has a neglegible change under these conditions.

5.6 Conclusions

This work presents a numerical investigation of the production of nitrous oxide in the process of ammonia oxidation over a platinum wire under industrial conditions using a detailed chemistry mechanism. Firstly, the production of nitrous oxide was investigated with a isolated wire. The effect of varying the process operating conditions were studied, as well as the effect of the variation of the wire diameter. It was found that the selectivity towards the production of nitrous oxide is affected by changes of the wire surface conditions, e.g. temperature and species mole fractions due to these process modifications. In the isolated wire the effect of changing the wire diameter was studied as well. It was found that the selectivity to N_2O increases when the wire diameter decreases.

The local selectivity around the wire was investigated. It was found that the most selective area of the wire is the one facing the flow, and the least selective is the back part of the wire. This is found to happen due to the changes of ammonia surface concentrations on the surface. The selectivity as a function of the inlet velocity was studied as well, by which we found that the selectivity not only shifts with increasing the inlet velocity, it also makes significantly more selective the front part of the wire.

In other 2D computations, the effect of adding wires perpendicular to the flow was studied. It was found that the closer the wire are, the higher the selectivities. A staggered configuration of wires was investigated as well. In this case, for a specific configuration of geometry and process conditions, it is found that the second wire shows a higher local selectivity than the first wire. This could be explained by the obstacle presented by the first wire changing the flow field around the second wire, or due to a configuration of the second wire's surface. To elucidate which condition affects the most, the temperature of all of the wires was fixed equally. In this case, it is found that the increased selectivity of the second wire disappears, showing that the main driver to a higher selectivity of the second wire is its lower temperature.

In the model, the effect of radiation was accounted for. Including radiation decreases the wire temperature, which increases the N_2O selectivity. It is found that neglecting radiation

may change the N_2O selectivity by as much as 55 %. However, all trends of the parametric studies were similar, regardless of the inclusion of radiation.

Another aspect investigated in this section is the heat and mass transfer coefficients. It is found that the correlations can model relatively well the wire temperature with differences of 10-20 K depending on the correlations. These then were compared with the simulation results and errors of 3-13% were found for heat and mass transfer, respectively. A drawback of using the correlations is the need to know a priori the wire temperature, so that the film temperature can be used. It also does not allow to predict for selectivity.

The correlations to compute the heat and mass transfer coefficients were used to calculate an estimate of the wire temperature. It was found that the wire temperature prediction fits well the CFD results. However, when comparing independently the heat and mass transfer coefficients, it was found that some deviations exist.

On the chemical level, the effect of increased selectivity by increasing the ammonia mole fraction on the surface was studied. Firstly, a sensitivity analysis was performed to all the parameters relevant to the chemical mechanism, i.e., T, xNH_3, xNO, xO_2. It was found that the most relevant sensitivity under the studied conditions is with respect to the variation of ammonia mole fraction xNH_3. Once this was established, then the sensitivity of the surface coverages to varying the ammonia mole fraction on the wire surface was studied. It was found that the highest sensitivity was with respect to the surface coverage of $\theta_a - \mathrm{NO}$. The sensitivity was strong and negative, implying that an increase of the ammonia mole fraction on the surface reduces the surface coverage of oxygen. From the sensitivity analysis, it was found that the empty a site coverage increases accordingly. This can induce a faster adsorption of NO, increasing the site coverage of NO, and therefore, favouring the reaction $\mathrm{NO{-}a + N{-}a} \longrightarrow \mathrm{N_2O + 2\,a}$ which increases the selectivity towards N_2O. Finally a feasible way to study the performance of complex 3D shapes is presented, which can be used in catalyst mesh design with the aim to reduce the nitrous oxide selectivity.

Chapter 6

Effect of turbulence on Pt wires

Acknowledgements

This Chapter was made in collaboration with PhD Student Ivan Cornejo, who did the simulations of the hot wire in air. All other simulations were performed by me.

6.1 Introduction

The aim of this chapter is to elucidate the effect of turbulence in the simulation of the ammonia oxidation process. The industrial scale reactor is of a large size, and operates at Reynolds of about 500,000. Therefore, turbulence is expected in the reactor. The variables that are of interest are the effect on wire temperature, the conversion and the selectivity.

The approach of this problem is separated in two parts. First, a single wire in a sufficiently large domain is studied with only heat transfer. This simplifies the computational requirements considering that the simulation of the reactions can be very expensive. This is done for a variety of parameters and boundary conditions, to determine their influence in the result. Lastly, a simulation is performed using all the transport properties plus the surface reactions.

The heating of a single wire is a popular problem. A thorough example for low to medium Re is [43]. However, the peculiarity of this problem is the existence of two Re describing the flow, that may affect the existence of turbulence. The first is based on reactor conditions,

and as mentioned in the previous early, its magnitude is of about 500,000. The second Re is based on wire conditions, considering the increase of temperature which affects the viscosity, and the wire diameter, which is orders of magnitude smaller than the reactor diameter. In this case the Re is of about 4. Therefore, some form of transitioning is expected, and this might affect the speed of the reaction and it selectivity by changing the composition of the gas phase species on the wire surface.

6.2 Computational model

6.2.1 Domain

The domain used in this study consists of a cylinder in a large domain, presented in Figure 6.1.

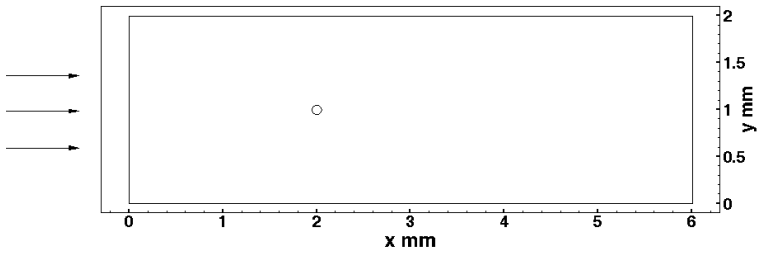

(a) xy plane of the domain

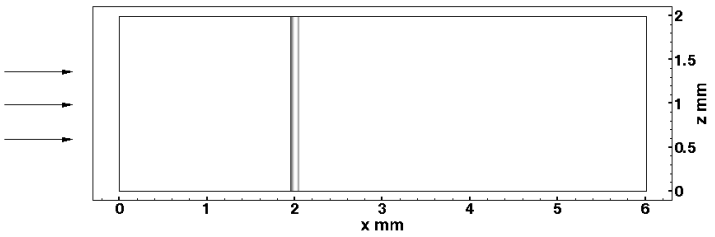

(b) xz plane of the domain

Figure 6.1: Domain of study

The diameter of the cylinder is 100 μm and it is located at the center in the y axis, and

20 diameters from the inlet in the x axis. The domain height was parameterized, so that the results do not see an influence of the boundary placements. In this study, a height of 20 Diameters was used. The boundary placements study is shown in Figure 6.2.

6.2.2 Boundary conditions

For every inlet we impose a velocity inlet, for every outlet we impose a pressure outlet. For the walls periodic boundary conditions were used. The boundary conditions at the wire surface are described now. The wire surface is modeled as no-slip for fluid flow. No thermal boundary condition is needed for the fluid, because the solid-fluid problem is modeled as conjugated heat transfer. The boundary condition for the wire surface includes the source term accounting for the heat of reaction. For species source terms, we used a modified version of the ammonia oxidation mechanism proposed by [40] with surface density of $\Gamma = 2.72 \cdot 10^{-5}$ mol/m^2 [62] for both active sites. The surface rates are integrated over time until steady state is obtained [35], which gives the surface coverages of the species, with which the reaction source terms can be computed. The net source terms for each species are expressed as:

$$\frac{d\Theta_i}{dt} = \frac{\dot{s_i}}{\Gamma} \rightarrow 0 \tag{6.1}$$

where i refers to the adsorbed species i and s is the net source term of adsorbed species i. Once in steady state, the surface concentrations of the adsorbed species can be found, and used to calculate the net source terms of the gas phase species. These source terms are coupled with the boundary conditions on the wire. First, the species flux boundary conditions is presented in Equation (6.2) [32]:

$$-D_{im}\frac{\partial C_i}{\partial n}|_{wire} = \dot{s_i} \tag{6.2}$$

The thermal boundary condition is given by the net difference of enthalpy of formation on the surface for each of the reactions, which in steady state is equals to the heat flux from

the surface to the flow:

$$-k_s \frac{\partial T_f}{\partial n}|_{wire,in} - k_f \frac{\partial T_f}{\partial n}|_{wire,out} = \sum_j \Delta H_{R,j} \dot{s_j} \tag{6.3}$$

j runs for each of the products NO, N_2O and N_2, k_f is the thermal conductivity of the fluid and $\Delta H_{R,j}$ is the heat of reaction of species j.

For the turbulent boundary conditions, the default length scale is set to 2 mm, which is the maximum allowed by the domain of study, and 40% of inlet turbulent intensity, unless otherwise stated.

6.2.3 Mesh study and code validation

Mesh studies were performed to guarantee mesh independence of the solution.

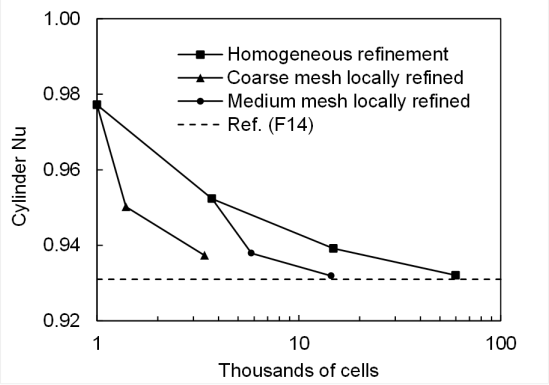

(a) Nusselt number based on cylinder properties versus the number of elements of the domain, for different local boundary mesh refinements.

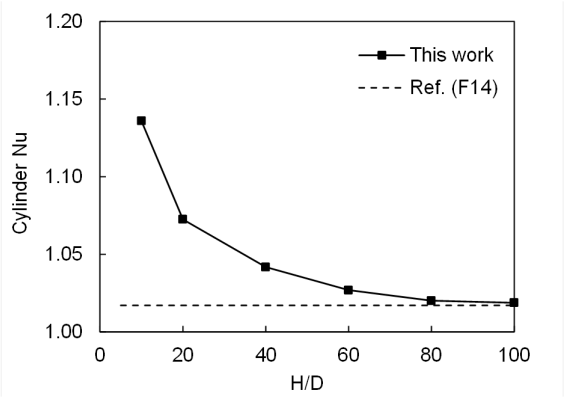

(b) Nusselt number based on cylinder properties versus the number of elements of the domain, for different local boundary mesh refinements

Figure 6.2: Mesh and Domain independence study. Ref refers to Figure 14 of [43]

6.3 Results and discussion

The base case parameters are shown in Table 6.1:

Table 6.1: Base case parameters

Parameter	value
inlet velocity m/s	0.75
Pressure bar	5
inlet temperature °C	200
xNH_3	0.10
xO_2	0.19
wire diameter μm	100
Re_∞ /Re_{wire}	10.6 / 2.0
Turbulence intensity	40%
Turbulence length scale mm	2

6.3.1 Constant temperature wire in air

The cylinder temperature is fixed at T=1265 K. The temperature of air at the inlet is 423 K. The Nusselt number is computed based on the wire temperature.

Comparison of turbulence models

The Nusselt number based on wire temperature is studied under with different turbulence models. The results are shown in Figures 6.3 and 6.4.

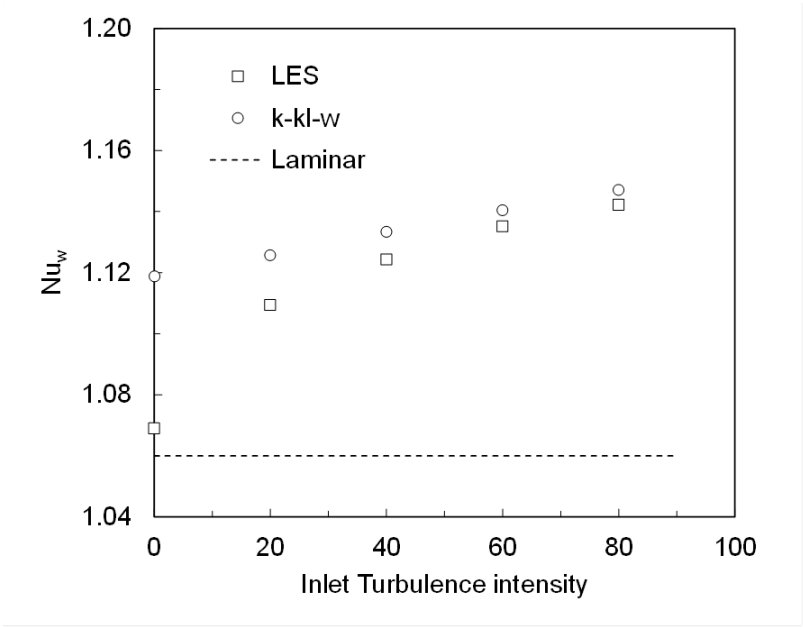

Figure 6.3: Comparison of different turbulence models applied for the case of a cylinder with constant temperature. Laminar case is shown

Figure 6.3 shows that the Nusselt number is a function of the inlet turbulent intensity. Firstly, it is found that the Nu number is increased with respect to laminar flow at any turbulence intensity level. Also, it is found that larger turbulent intensities increase the Nusselt number. These findings are expected as larger turbulence intensities are expected to increase energy transport by the eddies. Considering the LES, the case where high turbulence intensity versus the case where low turbulence intensities, the variations are of the order of 6%.

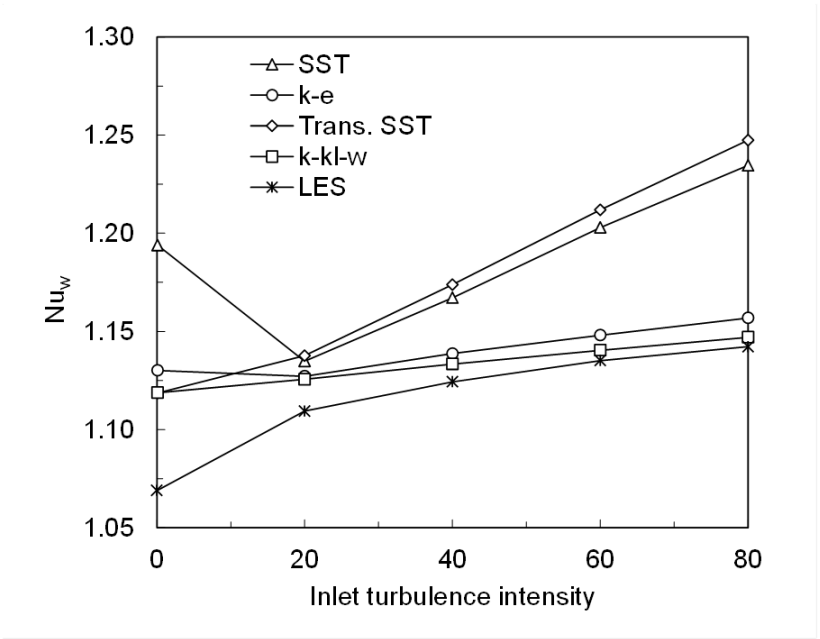

Figure 6.4: Turbulence intensity and Nu for different turbulence models applied for the case of a cylinder with constant temperature.

Considering the LES to be the most realistic approximation, it is found that SST and transitional SST models overpredict the turbulence, which is magnified at larger inlet turbulent intensities. The magnitude of this deviation is of about 9%. This is understandable since these models are meant to approximate better fluid flow close to surfaces, and in this case most of the flow is unbounded flow. The models k-e and k-kl-ω model better the Nusselt number based on wire temperatures. The deviation decreases as the inlet turbulent intensity increases. The magnitude of the error is of 5% for inlet turbulence intensity $<$ 20% and of 3% at higher turbulece intensities. The model k-kl-ω gives slightly better results compared to k-e.

6.3.2 Sensitivity to turbulence boundary conditions

Considering that each LES is very time consuming, and that from the findings of Figure 6.4 k-kl-w and LES give similar results, it is considered that k-kl-w can be used to do a parameterization of the inlet boundary conditions in the most economical manner. As the

sensitivity to turbulent intensity was studied in the previous section, here the turbulence length scale is parameterized at a constant turbulent intensity of 40%. The results are presented in Figure 6.5.

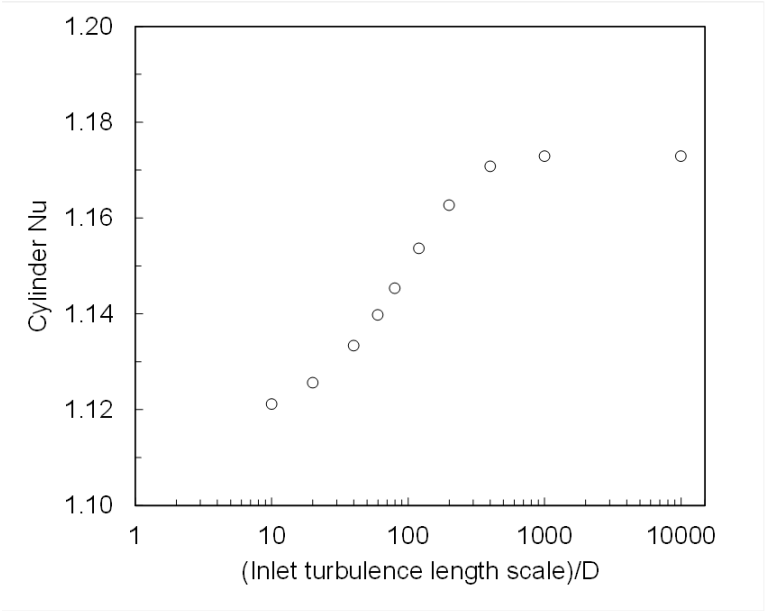

Figure 6.5: k-kl-w turbulence length scale parameterization

It can be seen in Figure 6.5 that the Nusselt number is an increasing function of the Inlet turbulence length scale, up to point where a plateau is reached. This occurs at about LE = 400 D. The Nusselt variation is bounded then by the lowest number of 1.12 to the largest of 1.17. This means a variation of 4.5 % in the Nusselt number estimation due to the turbulence length scale.

6.3.3 Constant temperature wire conclusions

It was found in this section that the Nusselt number based on wire conditions is dependent on bulk stream turbulence. These variations are of the order of 6% regarding the inlet turbulence intensity in a range of 0-80% for length scale of 2 mm. With respect to the length scale, it is found that the variations are of 4.5% in a range of LE of 10D to 10000D.

6.4 Ammonia oxidation

The domain under consideration is shown in Figure 6.1. The mesh is a coarse mesh locally refined, as swown in Figure 6.2 (a). The discretization error is therefore bounded, and lower than 1%. The H/D in this case is of 20, which relates to a 7% difference with respect to a completely isolated wire in terms of the Nusselt number. It is important to consider that the wires are normally grouped in distances of the order of 1.5D to 3D in a common Pt gauze. In this section we study the effect of bulk turbulence in terms of NO and N_2O selectivities, conversion and wire temperature. Firstly the laminar case of this model is presented and then the LES is presented, so that comparisons can be made.

6.4.1 Adsorption dynamics

Considering that the time step for resolving LES can be very small, it is important to elucidate what are the dynamics of the adsorption sites according to the chemical mechanism. The mechanism by [40] consists of 4 site species and 2 adsorption sites. According to the mechanism, the site balances can be written as:

$$
\begin{aligned}
\Gamma_a \frac{d\Theta_{N-a}}{dt} &= k_5\Theta_{NH_3-b}\Theta_{O-a} - 2k_8\Theta_{N-a}^2 - k_9\Theta_{N-a}\Theta_{O-a} - k_{10}\Theta_{NO-a}\Theta_{N-a} \\
\Gamma_a \frac{d\Theta_{O-a}}{dt} &= 2k_3P_{O_2}\Theta_a^2 - 2k_4\Theta_{O-a}^2 - 1.5k_5\Theta_{NH_3-b}\Theta_{O-a} - k_9\Theta_{N-a}\Theta_{O-a} \\
\Gamma_b \frac{d\Theta_{NH_3-b}}{dt} &= k_1P_{NH_3}\Theta_b - k_2\Theta_{NH_3-b} - k_5\Theta_{NH_3-b}\Theta_{O-a} \\
\Gamma_a \frac{d\Theta_{NO-a}}{dt} &= k_6P_{NO}\Theta_a - k_7\Theta_{NO-a} + k_9\Theta_{N-a}\Theta_{O-a} - k_{10}\Theta_{NO-a}\Theta_{N-a} \\
\Theta_a &= 1 - \Theta_{N-a} - \Theta_{NO-a} - \Theta_{O-a} \\
\Theta_b &= 1 - \Theta_{NH_3-b}
\end{aligned}
$$

The initial conditions used are of empty sites, or $\Theta_a(t=0) = \Theta_b(t=0) = 1$. The last two equations correspond to the site coverage balance, meaning that the active sites are either empty or covered with some of the surface species. This system as it is presented is a Differential Algebraic Equation (DAE). The algebraic equations correspond to the site

balances. This DAE is of order one, because the last to equations can be derived with respect to time once to obtain a system of Ordinary differential equations (ODE). However, this system is not a normal system of ODE because of the use of the mole balance, which gives equations that are linearly dependent on the others, and gives a singular Jacobian. This therefore requires special treatment for integration such as stiff solvers.

Another characteristic of the system is its dependence on partial pressures, as can be seen by P_{NO}, P_{O_2} and P_{NH_3}. The Arrhenius terms depend on the temperature T, so the solution depends on four parameters. Varying any of these values leads to different adsorption dynamics and steady state coverages surface. In this section the study of the dynamics is performed by considering empty sites as initial conditions, and for the parameters, the values of the bulk partial pressures on the wire surface performed in the single wire study. With this information, the steady state coverages and its dynamics can be computed.

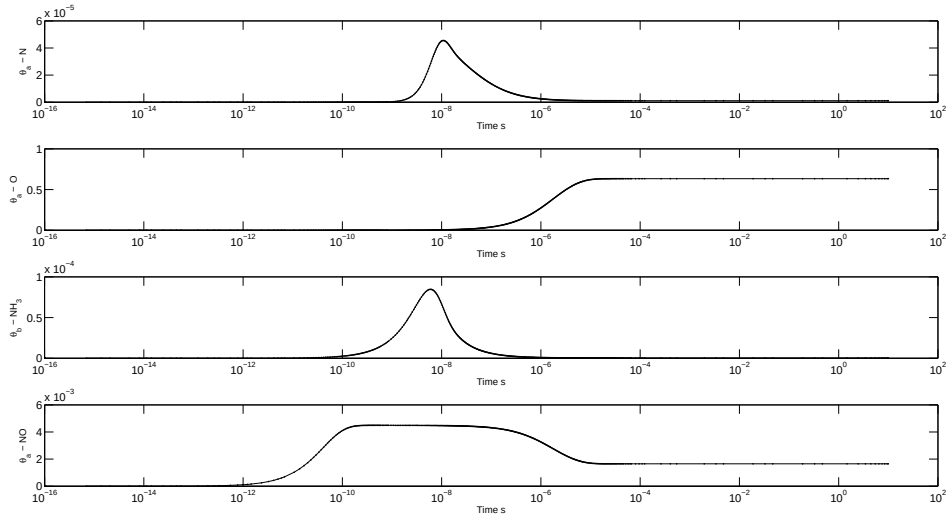

Figure 6.6: Adsorption dynamics with initial conditions of empty sites, and surface conditions of T = 1229.6, xNH_3 = 2.06 e-3, xO_2 = 4.17e-2 and xNO = 9.92 e-2

Figure 6.6 shows the adsorption dynamics considering the single wire case presented in Chapter 5. The surface temperature and mole fractions are obtained from the CFD simulation. Here the interest is regarding the time to achieve the steady state. It was found

that this time for this case is of about 1e-5 s or 10 μs. This calculation is done independently by solving the DAE shown above, but it can be seen that the solution matches the results shown in Chapter 5. The largest surface coverage is of θ_a-O = 0.64. The slowest response is the one of θ_a-O and θ_a-NO.

6.4.2 LES study

Before considering the LES study, a simpler study with k-ω SST turbulence model was used to describe the behaviour of turbulence close to the wire.

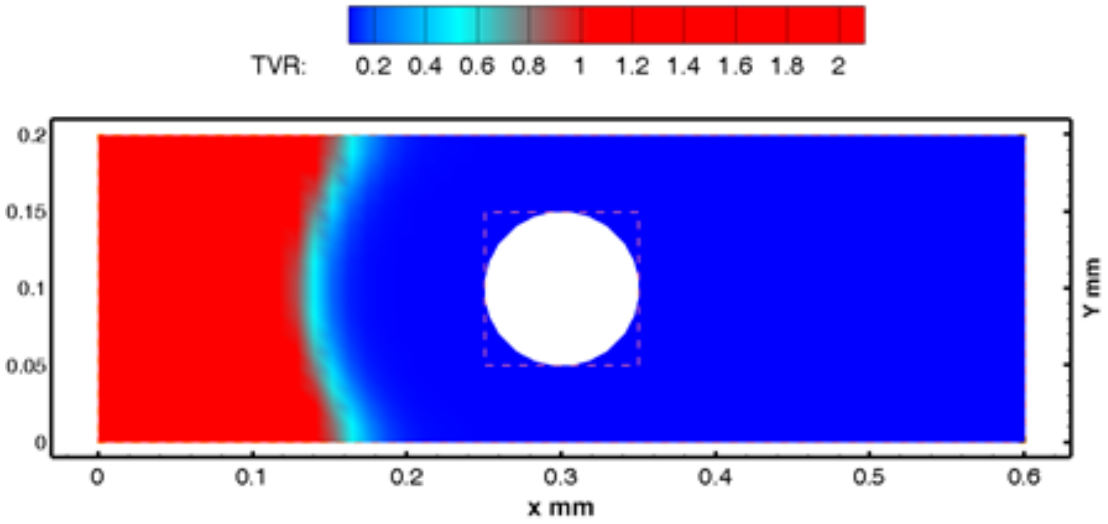

Figure 6.7: Turbulent viscosity ratio for model k-ω SST, I=40%, l=1e-3, V_{in}=0.75 m/s, O/A = 1.8, T_{in} = 473.15 K

In Figure 6.7 it can be seen that the turbulent viscosity ratio decays quickly upstream of the wire. This can be explained by the upstream thermal diffusion, which increases the molecular viscosity and reduces the ratio. From this, it is expected that the turbulent effects on the wire surface are not of relevance, given the fact that the TVR is of the order of 0.2 close to the wire.

However, considering the findings of the previous section, it seems logical to compare a LES if computationally possible with the laminar case, since the deviation of Nusselt

number is $< 10\%$. In this case we refer to the inlet conditions presented in Table 6.1. The time step used in this study is 2.5e-5 s and the CFL is of 0.4, well below 1. It is worthwhile noting that the timestep is 2.5 times longer than the required to achieve steady state from empty sites for the chemical mechanism, as shown in the previous section, so that it is fair to assume that the chemistry is in steady state for the flow. The subgrid scale stress is modeled using WALE as described in the theory section. The boundary conditions are the ones shown in Table 6.1. The spectral generator is used to create the turbulent eddies.

The summary of results showing global variables considering the laminar case and LES are shown in Table 6.2. In the same table the time average results for 0.1s which is 12.5 space time τ.

Table 6.2: Laminar and time averaged LES results

Parameter	Laminar	LES
conversion %	5.30	5.25
N_2O sel %	0.85	0.84
NO sel %	98.9	98.9
Twire K	1265.66	1266.04
Tout K	511.53	511.25
r NH_3 mol/m2/s	3.266	3.232
r N_2O mol/m2/s	0.01391	0.01368

In Table 6.2 a comparison betweeen the results of Laminar model and LES model in terms of global variables is shown. It can be seen that the differences are very small. For instance, in terms of selectivities, the differences is of the order of 0.01% for N_2O. The average wire temperature is 0.38 K in LES. The effluent gas temperature differs only by 0.28 K. The conversion changes by 0.5%.

The transient temperature of the Pt wire is shown in Figure 6.8.

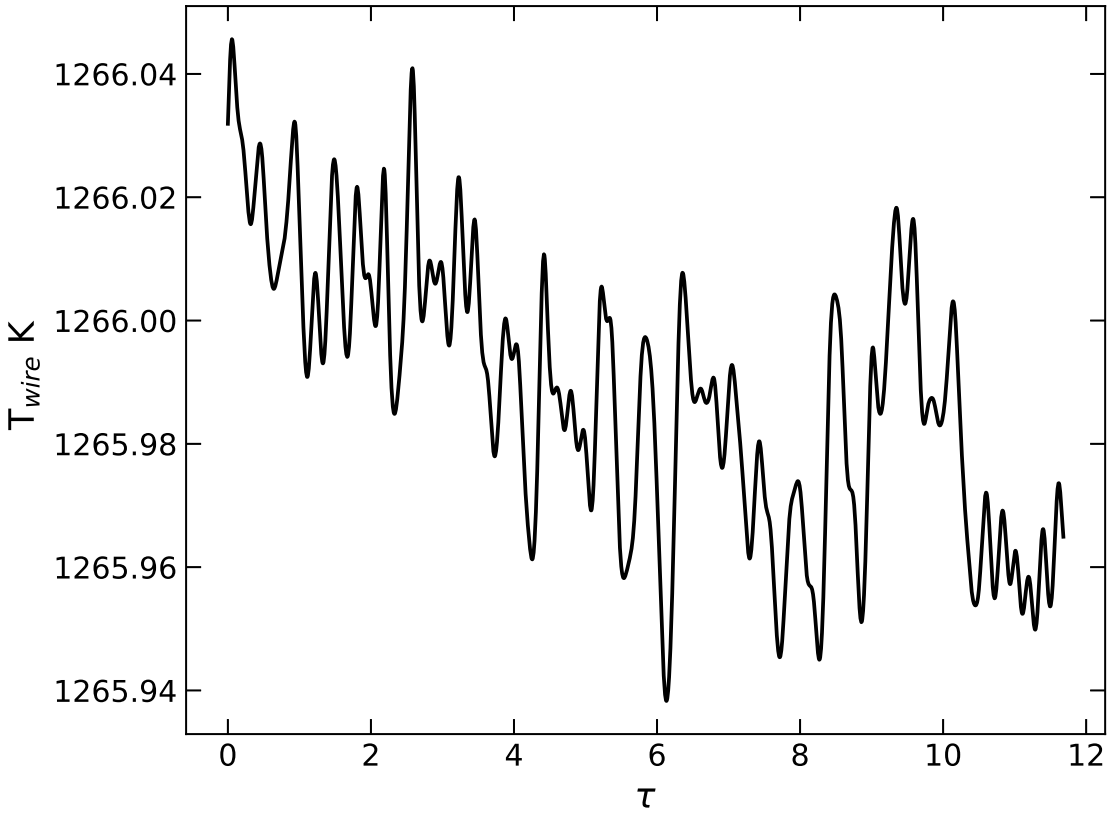

Figure 6.8: Wire temperature a function of time measured in space times.

It can be seen in Figure 6.8 that the wire temperature is fairly constant, varying no more than 0.2 K over the 11.9 τ under study. The variations can be explained by the varying amount of ammonia hitting the surface. However, this effect is compensated by an increase in reaction rate and heat transfer, which explains why the wire temperature is relatively constant.

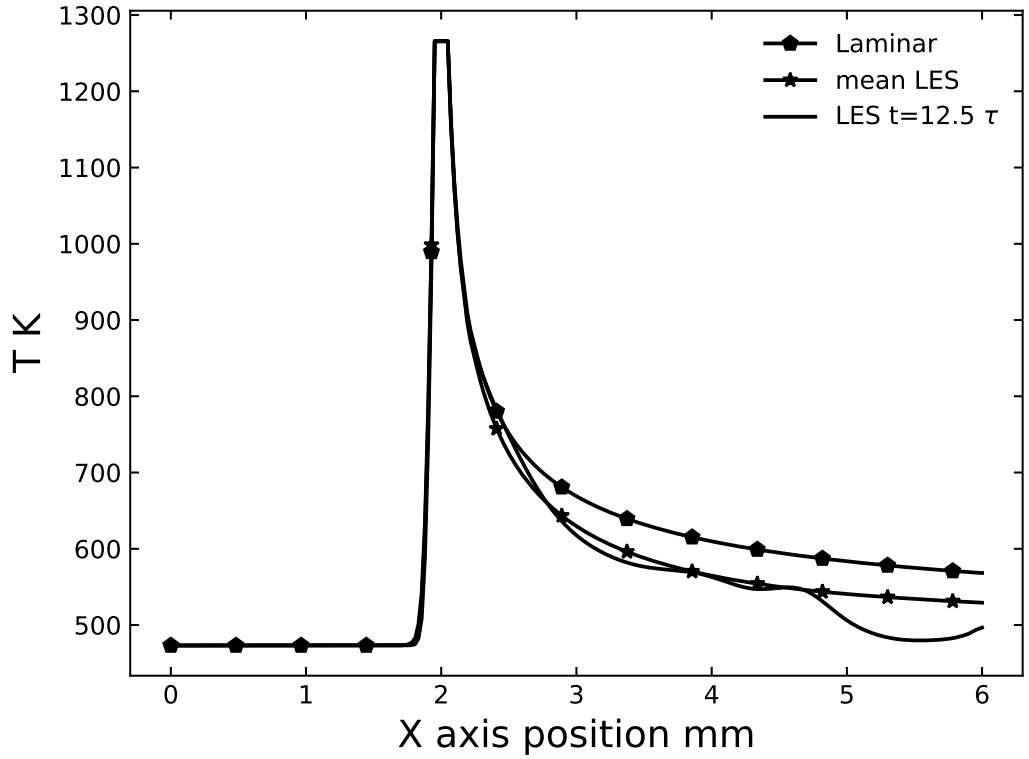

Figure 6.9: Temperature profile along a centerline on the x axis

In Figure 6.9 the temperature profile along a centerline of the x axis is shown. The three profiles correspond to the laminar temperature profile, the time averaged LES profile, and an instantaneous LES profile at t=12.5 τ. The profiles do not differ noticeably until about x=2.5 mm, which corresponds to 5D downstream the cylinder. Therefore, the wire surface does not see an influence of the turbulent flow in regards of the temperature compared to the laminar case.

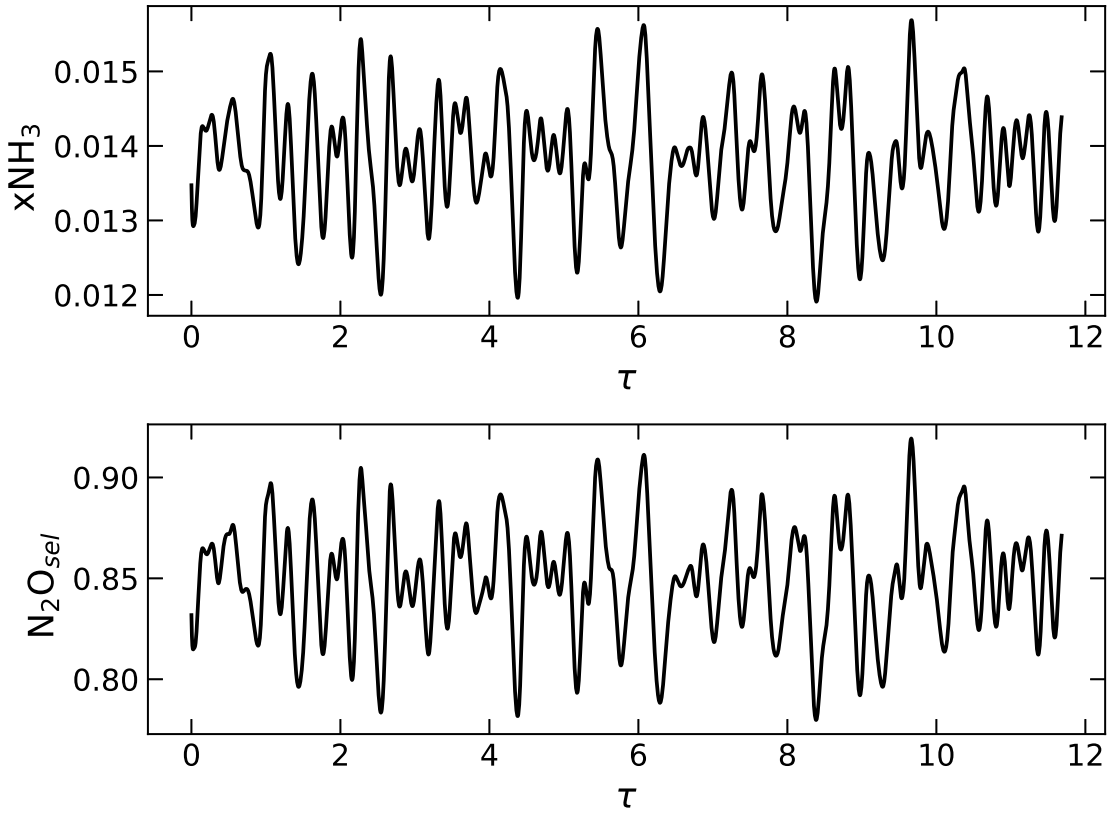

Figure 6.10: Transient surface ammonia mole fraction and N_2O selectivity as a function of time measured in space times. The correlation coefficient between these two series is 0.995.

In Figure 6.10 the instantaneous selectivity and surface ammonia mole fraction are presented. The N_2O selectivity is bounded within 0.84% +/- 0.08%. The ammonia surface mole fraction varies in the same way as the selectivity. The correlation coefficient between the two time series is 0.995, reflecting this observation.

Finally, it is possible to study the transient Nusselt and Sherwood numbers, as defined in Chapter 5.

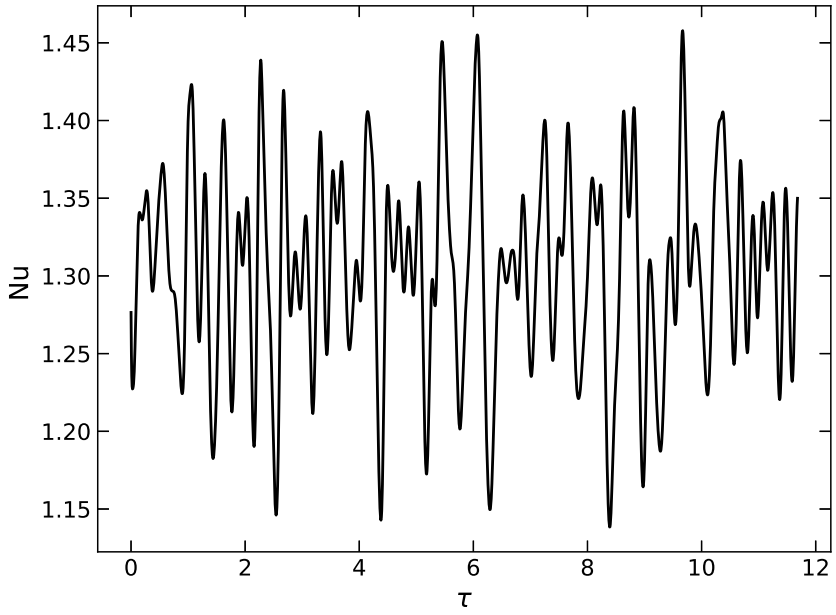

Figure 6.11: Transient Nusselt number under the LES study

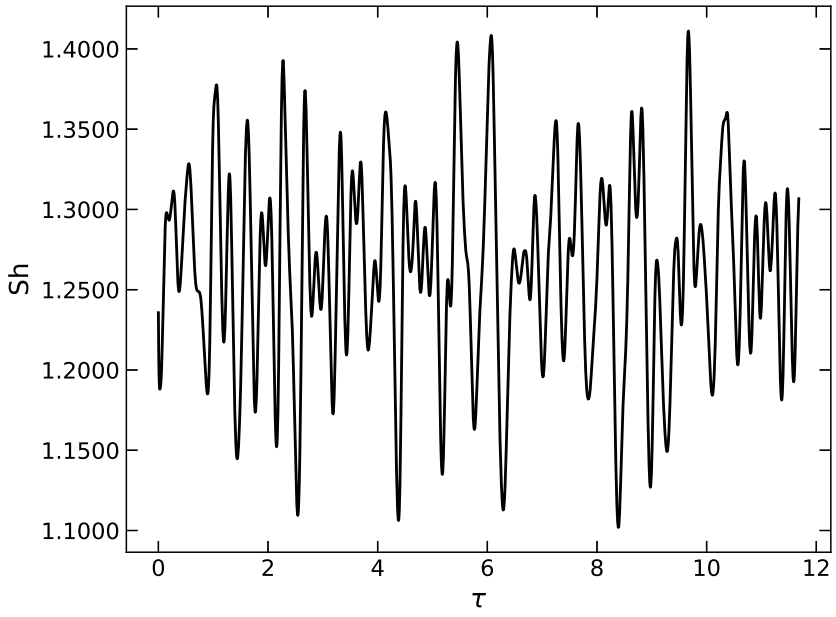

Figure 6.12: Transient Sherwood number under the LES study

As can be seen in Figures 6.11 and 6.12, the Nu and Sh numbers vary considerably. However, the wire temperature varies very little. This is because the wire temperature is a

function of the ratio of these two quantities as shown in Section 5. The ratio is shown in Figure 6.13.

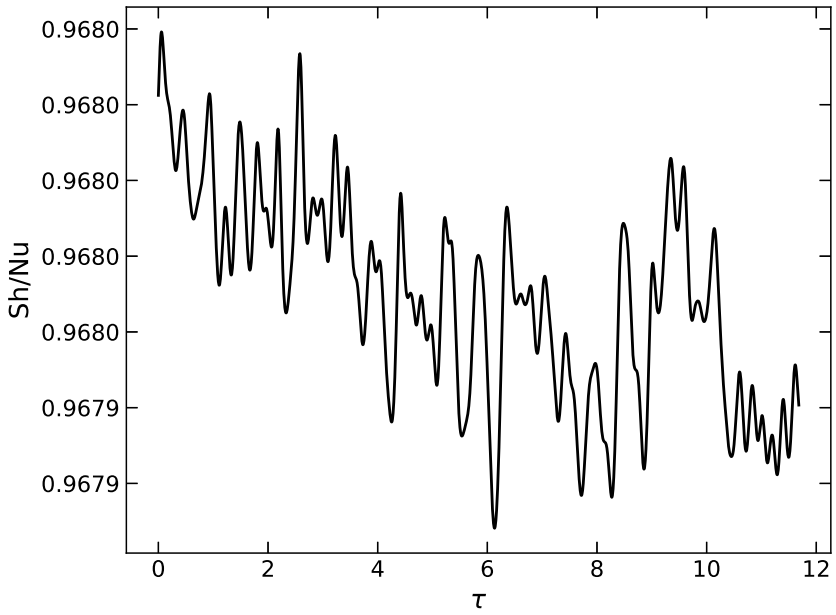

Figure 6.13: Transient Sh/Nu number the LES study

In Figure 6.13 it is possible to observe that the temporal variation of the Sh/Nu is lower than 1E-4, which is reflected in the almost inexistent wire temperature variation. Then, as predicted by the ratio of Sh/Nu, the temperature shown in Figure 6.8 follows the same trend as the ratio of Sh/Nu.

6.5 Conclusions

Hot wire in air Nusselt number is increased with turbulence intensity and turbulence length scale with respect to the laminar case. Two equations RANS models do not predict well the Nusselt number. Best prediction is with k-kl-ω at medium turbulence intensity levels. The variations of Nusselt number with respect to laminar case are of the order of 6% accounting for sensitivity of turbulence boundary conditions.

Ammonia oxidation LES and laminar give similar global variables. Conversion changes by 0.05% and N_2O selectivity by 0.01% on average. The transient response of the wire temperature is almost constant, varying less than 0.2K in 11.9 τ. The temperature profiles are indistinguishable until 5D downstream the cylinder. The N_2O selectivity and ammonia surface mole fraction are highly correlated. The Nusselt and Sherwood number vary in the LES case as a function of the time. However, the ratio Sh/Nu varies very little, which explains the almost constant wire temperature. Transient variations of the selectivity are explained mainly due to transient variations of the ammonia surface concentration, and on average no effect is found compared to the laminar case, which can be explained by the upstream diffusion of the thermal energy, which decreases the turbulent viscosity ratio, so that any effect of turbulence at the wire surface is neglegible.

Chapter 7

Conclusions and future work

In this work a mechanism for ammonia combustion on polycrystalline Pt surface is used. This mechanism is then coupled with a CFD code, using transport information available in the literature, so that the combustion process can be explored in more detail. In this work it was shown for first time that, for the range of operating conditions, the coupling of the mechanism with the transport phenomena shows expected results for an operating plant. These results are further explored to gain more insight on what occurs at surface level, and to gain more insight on the production of nitrous oxide. The reaction is mass transfer controlled and a typical assumption when this is the case is to consider the concentration of the reacting gas, in this case ammonia (NH_3) to be zero. It is shown that that is not the case, although the concentration is very low as expected. The concentration of ammonia on the surface affects the surface coverage of O_2 on sites a of the mechanism, leads to an increase coverage of NO and reduced gas phase production rate of NO, leading directly to the creation of more N_2O. This has not been shown in the literature prior to this work.

The assumption of laminar flow was used to determine the results shown above. However, it is known that that is not the case, and some degree of turbulence is expected in the reactor considering its dimensions, design and operating conditions. The Reynolds number based on reactor diameter is of about 500,000. However, the Reynolds number based on the wire diameter is of the order of 10. Therefore bulk turbulence is expected, but at the local level is expected to laminarize. However, the reaction takes place on Pt wires of about 100 μm diameter, and no more than 10 are used in mid pressure reactors. Therefore, some

form of transitional flow is expected in this area and whether the turbulence plays a role in the reaction speed or selectivity was unknown prior to this work. Here, it was shown also for first time that the laminar assumption shows almost the same results in terms of conversion and selectivity, as the turbulent models. The turbulence was modelled using different approaches, but all the results refer to the use of LES. Since the time scale required for LES is very small, the time scale for the adsorption process was studied. It was found that the steady state for empty sites is achieved 2.5 times faster than the time scale used in the LES study, so that the chemical mechanism is in steady state with respect to the flow.

A last point, the methodology of combining CFD and detailed chemical mechanism can be easily used in other processes, and some researchers already have done it. However, an important limitation of the use of detailed mechanistic models is its strong computational cost. In this work explorations were performed to see if the mechanism can be computed using surrogate models such as lookup tables. These are extensively studied, and the conclusions are that they can work well only for limited number of inputs. A variation of the Hermite lookup tables was studied, namely the four point stencil approach, which in principle could save memory and allow for extension of the number of input variables. The results show that the performance is equal to the one of Hermite lookup tables levelling for accuracy, and therefore not allowing for an increase in the number of input variables. Another explored alternative was the use of Neural Networks, which was applied only to the ammonia oxidation mechanism. It was shown that the mapping reduces considerably the computational expense and the memory requirements, while keeping the accuracy constant. However, this alternative was not tested successfully for other mechanisms, and this could be an isolated result for a rather simplistic mechanism.

In future work the complete reactor can be simulated using the approach presented in this work, which would allow for more insight in the ammonia oxidation process. The surface reactions can be coupled with the gas phase reactions and compared with the actual effluent from a ammonia oxidation reactor. Also, an expansion of the use of the reduction techniques can be used to reduce the need for computational power in the simulation of the ammonia

oxidation reactor. The effect of transient phenomena as varying the inlet conditions can be computed easier than modelling the complete reactor. Finally, the neural network approach can be used for calculating the selectivity in the ammonia oxidation process. Later it can extended for other mechanisms, considering its potentialities of reducing the required memory and increased speed up, while giving the same accuracies as the lookup tables approach.

References

[1] *Ullmann's encyclopedia of industrial chemistry*. Wiley-VCH, 2002.

[2] *Ansys Fluent user guide 17.2*. 2016.

[3] Hamed Abbasfard, Mehdi Ghanbari, Amin Ghasemi, Ghazal Ghahraman, Seyyed Mohammad Jokar, and Mohammad Reza Rahimpour. Cfd modelling of flow maldistribution in an industrial ammonia oxidation reactor: A case study. *Applied Thermal Engineering*, 67(1):223 – 229, 2014.

[4] M. Baerns, R. Imbihl, V.A. Kondratenko, R. Kraehnert, W.K. Offermans, R.A. van Santen, and A. Scheibe. Bridging the pressure and material gap in the catalytic ammonia oxidation: structural and catalytic properties of different platinum catalysts. *Journal of Catalysis*, 232(1):226 – 238, 2005.

[5] R. Byron Bird, Warren E. Stewart, and Edwin N. Lightfoot. *Transport Phenomena*. Second edition, 2006.

[6] Christopher M. Bishop. *Neural Networks for Pattern Recognition*. Clarendon Press - Oxford, 1995.

[7] J Blasco, N Fueyo, C Dopazo, and J-Y Chen. A self-organizing-map approach to chemistry representation in combustion applications. *Combustion Theory and Modelling*, 4(1):61–76, 2000.

[8] J.A. Blasco, N. Fueyo, C. Dopazo, and J. Ballester. Modelling the temporal evolution of a reduced combustion chemical system with an artificial neural network. *Combustion and Flame*, 113(1):38 – 52, 1998.

[9] Justin M. Blasi and Robert J. Kee. In situ adaptive tabulation (isat) to accelerate transient computational fluid dynamics with complex heterogeneous chemical kinetics. *Computers and Chemical Engineering*, 84:36 – 42, 2016.

[10] Edwin Catmull and Raphael Rom. A class of local interpolating splines. In Robert E. Barnhill and Richard F. Riesenfeld, editors, *Computer Aided Geometric Design*, pages 317 – 326. Academic Press, 1974.

[11] A.K. Chatzopoulos and Stelios Rigopoulos. A chemistry tabulation approach via rate-controlled constrained equilibrium (rcce) and artificial neural networks (anns), with application to turbulent non-premixed ch4/h2/n2 flames. *Proceedings of the Combustion Institute*, 34(1):1465 – 1473, 2013.

[12] F. C. Christo, A. R. Masri, E. M. Nebot, and T. Turanyi. Utilising artificial neural network and repro-modelling in turbulent combustion. In *Neural Networks, 1995. Proceedings., IEEE International Conference on*, volume 2, pages 911–916 vol.2, Nov 1995.

[13] Carl De Boor. *A practical guide to splines*. Springer Verlag, New York, 2001.

[14] Karla Herrera Delgado, Lubow Maier, S. Tischer, , Alexander Zellner, Henning Stotz, and O. Deutschmann. Surface reaction kinetics of steam- and co2- reforming as well as oxidation of methane over nickel-based catalyst. *Catalyst*, 5:871–904, 2015.

[15] C.R.H. deSmet, M.H.J.M de Croon, R.J. Berger, G.B. Marin, and J.C. Schouten. An experimental reactor to study the intrinsic kinetics of catalytic partial oxidation of methane in the presence of heat-transport limitations. *Applied Catalysis A: General*, 187:33–48, 1999.

[16] O. Deutschmann, R. Schmidt, F. Behrendt, and J. Warnatz. Numerical modeling of catalytic ignition. *Symposium (International) on Combustion*, 26(1):1747 – 1754, 1996.

[17] Olaf Deutschmann and Lanny D. Schmidt. Modeling the partial oxidation of methane in a short-contact-time reactor. *AIChE Journal*, 44(11):2465–2477, 1998.

[18] J Dumesic, D Rudd, L Aparicio, J Rekoske, and A Trevino. *The microkinetics of heterogeneous catalysis*, pages 1–53. American Chemical Society, 1993.

[19] US Environment Protection Agency. Methane and nitrous oxide emissions from natural sources. 2010.

[20] Anton Fadic, Teng-Wang Nien, Joseph Mmbaga, Robert E. Hayes, and Martin Votsmeier. A case study in multi-scale model reduction: The effect of cell density on catalytic converter performance. *The Canadian Journal of Chemical Engineering*, 92(9):1607–1617, 2014.

[21] Robin E. Ferner and Jeffrey K. Aronson. Cato guldberg and peter waage, the history of the law of mass action, and its relevance to clinical pharmacology. *British Journal of Clinical Pharmacology*, December 2015.

[22] Lucas L.C. Franke, Athanasios K. Chatzopoulos, and Stelios Rigopoulos. Tabulation of combustion chemistry via artificial neural networks (anns): Methodology and application to les-pdf simulation of sydney flame l. *Combustion and Flame*, 185:245 – 260, 2017.

[23] Edward N. Fuller, Paul D. Schettler, and J. Calvin. Giddings. New method for prediction of binary gas-phase diffusion coefficients. *Industrial & Engineering Chemistry*, 58(5):18–27, 1966.

[24] Juan D. Gonzalez, Maximilian Warner, Brian S. Haynes, and Alejandro Montoya. N2o formation and dissociation during ammonia combustion: A combined dft and experimental study. *Proceedings of the Combustion Institute*, 36(1):637 – 644, 2017.

[25] David G. Goodwin, Harry K. Moffat, and Raymond L. Speth. Cantera: An object-oriented software toolkit for chemical kinetics, thermodynamics, and transport processes, 2017. Version 2.3.0.

[26] Michael Groves, Meinhard Schwefer, and Rolf Siefert. Nitric acid - without the emissions. *TCE*, April 2006.

[27] Martin T. Hagan, Howard B. Demuth, and Mark H. Beale. *Neural Network Design*, chapter 9. PWS Publishing Company, 1996.

[28] S. L. Handforth and J. N. Tilley. Catalysts for oxidation of ammonia to oxides of nitrogen. *Industrial & Engineering Chemistry*, 26(12):1287–1292, 1934.

[29] S Hatscher, T Fetzer, E Wagner, and H. J. Kneuper. *Ammonia oxidation*, page 25752592. Wiley-VCH, 2008.

[30] Daniel A. Hickman and Lanny D. Schmidt. Modeling catalytic gauze reactors: ammonia oxidation. *Industrial & Engineering Chemistry Research*, 30(1):50–55, 1991.

[31] R. Imbihl, A. Scheibe, Y. F. Zeng, S. Gunther, R. Kraehnert, V. A. Kondratenko, M. Baerns, W. K. Offermans, A. P. J. Jansen, and R. A. van Santen. Catalytic ammonia oxidation on platinum: mechanism and catalyst restructuring at high and low pressure. *Phys. Chem. Chem. Phys.*, 9:3522–3540, 2007.

[32] F Incropera, D Dewitt, T Bergman, and A Lavinne. *Fundamentals of heat and mass transfer*, page 557. John Wiley and Sons, New York, 2011.

[33] ThyssenKrupp industrial solutions. Nitric acid brochure.

[34] Andreas Jess and Peter Wasserscheid. *Chemical Technology. An Integral Textbook.*, page 557. WILEY-VCH Verlag, Weinheim, Germany, 2013.

[35] Robert Kee, Michael Coltrin, and Peter. Glarborg. *Chemically reacting flow.* John Wiley and Sons, New Jersey, 2003.

[36] Markus Klingenberger, Ofer Hirsch, and Martin Votsmeier. Efficient interpolation of precomputed kinetic data employing reduced multivariate hermite splines. *Computers and Chemical Engineering*, 98:21 – 30, 2017.

[37] Andrzej Kolodziej, Mieczyslaw Jaroszynski, Bozena Janus, Tadeusz Kleszcz, Joanna Lojewska, and Tomasz Lojewski. An experimental study of the pressure drop in fluid flows through wire gauzes. *Chemical Engineering Communications*, 196(8):932–949, 2009.

[38] Andrzej Kolodziej and Joanna Lojewska. Mass transfer for woven and knitted wire gauze substrates: Experiments and modelling. *Catalysis Today*, 147(Supplement):S120 – S124, 2009. 3rd International Conference on Structured Catalysts and Reactors, ICOSCAR-3, Ischia, Italy, 27-30 September 2009.

[39] Andrzej Kolodziej, Joanna Lojewska, Mieczyslaw Jaroszynski, Anna Gancarczyk, and Przemyslaw Jodlowski. Heat transfer and flow resistance for stacked wire gauzes: Experiments and modelling. *International Journal of Heat and Fluid Flow*, 33(1):101 – 108, 2012.

[40] Ralph Kraehnert and Manfred Baerns. Kinetics of ammonia oxidation over pt foil studied in a micro-structured quartz-reactor. *Chemical Engineering Journal*, 137(2):361 – 375, 2008.

[41] R. Kraichnan. Diffusion by a random velocity field. *Physics of fluids*, (11):21–31, 1970.

[42] Ankan Kumar and Sandip Mazumder. Adaptation and application of the in situ adaptive tabulation (isat) procedure to reacting flow calculations with complex surface chemistry. *Computers and Chemical Engineering*, 35(7):1317 – 1327, 2011.

[43] C.F. Lange, F. Durst, and M. Breuer. Momentum and heat transfer from cylinders in laminar crossflow at 104 re 200. *International Journal of Heat and Mass Transfer*, 41(22):3409 – 3430, 1998.

[44] Shuang Li, Bin Yang, and Fei Qi. Accelerate global sensitivity analysis using artificial neural network algorithm: Case studies for combustion kinetic model. *Combustion and Flame*, 168:53 – 64, 2016.

[45] Sandip Mazumder. Adaptation of the in situ adaptive tabulation (isat) procedure for efficient computation of surface reactions. *Computers and Chemical Engineering*, 30(1):115 – 124, 2005.

[46] A. D. McNaught and A. Wilkinson. *IUPAC. Compendium of Chemical Terminology, 2nd ed. (the Gold Book)*. Blackwell Scientific Publications, 1997.

[47] T. Nien, J.P. Mmbaga, R.E. Hayes, and M. Votsmeier. Hierarchical multi-scale model reduction in the simulation of catalytic converters. *Chemical Engineering Science*, 93:362 – 375, 2013.

[48] Gerard Novell-Leruth, Josep M. Ricart, and Javier Prez-Ramrez. Pt(100)-catalyzed ammonia oxidation studied by dft: Mechanism and microkinetics. *The Journal of Physical Chemistry C*, 112(35):13554–13562, 2008.

[49] E.J. Nowak. Prediction of platinum losses during ammonia oxidation. *Chemical Engineering Science*, 24(2):421 – 423, 1969.

[50] Government of Alberta Environment and Parks. Alberta greenhouse gas reporting program. September 2013.

[51] W.K. Offermans, A.P.J. Jansen, and R.A. van Santen. Ammonia activation on platinum 111: A density functional theory study. *Surface Science*, 600(9):1714 – 1734, 2006.

[52] Wilhem Ostwald. Improvements in the manufacture of nitric acid and nitrogen oxides., 1906. Application number GBD190200698 19020109.

[53] Atkins P. and DePaula J. *Physical Chemistry*. W.H. Freeman and Company, New York, 2006.

[54] B. Partopour and A.G. Dixon. Computationally efficient incorporation of microkinetics into resolved-particle cfd simulations of fixed-bed reactors. *Computers and Chemical Engineering*, 88:126–134, 2016. cited By 12.

[55] M. Patricio, J.L. Santos, F.Patricio, and A.J.C. Varandas. Roadmap to spline-fitting potentials in high dimensions. *Journal of mathematical chemistry*, 51:1729–1746, 2013.

[56] J Perez-Ramirez, F Kapteijn, K Schffel, and J.A Moulijn. Formation and control of n2o in nitric acid production: Where do we stand today? *Applied Catalysis B: Environmental*, 44(2):117 – 151, 2003.

[57] Javier Perez-Ramirez, Evgenii V. Kondratenko, Gerard Novell-Leruth, and Josep M. Ricart. Mechanism of ammonia oxidation over pgm (pt, pd, rh) wires by temporal analysis of products and density functional theory. *Journal of Catalysis*, 261(2):217 – 223, 2009.

[58] T. Pignet and L.D. Schmidt. Kinetic of nh3 oxidation on pt, rh and pd. *Journal of Catalysis*, 40:212–225, 1975.

[59] S.B. Pope. Computationally efficient implementation of combustion chemistry using in situ adaptive tabulation. *Combustion Theory and Modelling*, 1(1):41–63, 1997.

[60] Stephen Pope. *Turbulent Flows*. Cambridge University Press, 2000.

[61] Merle Potter and David Wiggert. *Mechanics of fluids*. Brooks/Cole, 2002.

[62] Raul Quiceno, Javier Perez-Ramirez, Juergen Warnatz, and Olaf Deutschmann. Modeling the high-temperature catalytic partial oxidation of methane over platinum gauze: Detailed gas-phase and surface chemistries coupled with 3d flow field simulations. *Applied Catalysis A: General*, 303(2):166 – 176, 2006.

[63] A. Scheuer, A. Drochner, J. Gieshoff, H. Vogel, and M. Votsmeier. Runtime efficient simulation of monolith catalyst with a dual-layer washcoat. *Catalysis today*, 188:70–79, 2012.

[64] A. Scheuer, O. Hirsch, R. Hayes, H. Vogel, and M. Votsmeier. Efficient simulation of an ammonia oxidation reactor using a solution mapping approach. *Catalysis Today*, 175(1):141–146, 2011. cited By 19.

[65] A. Scheuer, M. Votsmeier, A. Schuler, J. Gieshoff, A. Drochner, and H. Vogel. Nh3-slip catalysts: Experiments versus mechanistic modelling. *Topics in Catalysis*, 52(13-20):1847–1851, 2009. cited By 26.

[66] R. Smirnov, S. Shi, and I. Celik. Random flow generation technique for large eddy simulations and particle-dynamics modeling. *Journal of Fluids Engineering*, (123), 2001.

[67] Michael Thiemann, Erich Scheibler, and Karlk Wilhelm Wiegand. *nitric Acid, Nitrous Acid and Nitrogen Oxides*. Wiley-VCH, 2005.

[68] Tamas Turanyi and Alison S. Tomlin. *Storage of Chemical Kinetic Information*, pages 485–512. Springer London, London, 2013.

[69] EPA US. Available and emerging technologies for reducing greenhouse gas emissions from the nitric acid production industry. *Environment Protection Agency U.S.*, December 2010.

[70] V. I. Vanchurin, E. V. Golovnya, and A. V. Yashchenko. Oxidation of ammonia on woven and knitted platinoid gauzes. *Catalysis in Industry*, 4(2):105–109, Apr 2012.

[71] M. Votsmeier, A. Scheuer, A. Drochner, H. Vogel, and J. Gieshoff. Simulation of automotive nh3 oxidation catalysts based on pre-computed rate data from mechanistic surface kinetics. *Catalysis Today*, 151(3):271 – 277, 2010.

[72] Martin Votsmeier. Efficient implementation of detailed surface chemistry into reactor models using mapped rate data. *Chemical Engineering Science*, 64(7):1384 – 1389, 2009.

[73] N. Waletzko and L. D. Schmidt. Modeling catalytic gauze reactors: Hcn synthesis. *AIChE Journal*, 34(7):1146–1156, 1988.

[74] Maximilian Warner and Brian S. Haynes. Formation of n2 and n2o in industrial combustion of ammonia over platinum. *Proceedings of the Combustion Institute*, 35(2):2215 – 2222, 2015.

[75] Steffen Weise, Sebastian Popp, Danny Messig, and Christian Hasse. A computationally efficient implementation of tabulated combustion chemistry based on polynomials and automatic source code generation. *Flow, Turbulence and Combustion*, 100(1):119–146, Jan 2018.

[76] David Wilcox. *Turbulence Modeling for CFD*. DCW Industries, 1994.

[77] Carl L. Yaws. *Chemical Properties Handbook: Physical, Thermodynamic, Environmental, Transport, Safety, and Health Related Properties for Organic and Inorganic Chemicals*. McGraw-Hill, 1999.

[78] Carl L. Yaws. *Yaws' Transport Properties of Chemicals and Hydrocarbons (Electronic Edition)*. Knovel, 2010.

Appendix

Transport properties

Table 1: Heat capacities coefficients J/mol/K for selected compounds [77].
$C_p = a + bT + cT^2 + dT^3 + eT^4$ 150 K < T < 1500 K

Compound	a	b x 10^3	c x 10^5	d x 10^9	e x 10^{12}	$\Delta_f H^0_{298}$ kJ/mol
N_2	29.342	-3.54	1.01	-4.31	0.26	0
O_2	29.526	-8.89	3.81	-3.26	8.86	0
NH_3	33.573	-12.6	8.89	-7.18	18.6	-45.9
NO	33.227	-23.6	5.32	-3.79	9.12	90.3
H_2O	33.933	-8.42	2.99	-17.8	3.69	-241.8
N_2O	23.219	62.0	3.80	6.97	0.81	82.1

Table 2: Viscosity coefficients for selected compounds [78].
$\mu = a + bT + cT^2 + dT^3$ μ Pa· s . 150 K < T < 1500 K

Compound	a	b	c x 10^4	d x ^{8}
N_2	4.4656	0.63814	2.6596	5.411
O_2	-4.9433	0.80673	-4.0416	10.11
NH_3	-7.6819	0.36699	-4.7132	0.048
NO	-0.6242	0.73843	3.7604	9.267
H_2O	22.821	0.17387	3.2465	-14.33
N_2O	-15.241	0.61281	2.4874	5.316

Table 3: Heat conductivity coefficients for selected compounds [78].
$k = a + bT + cT^2 + dT^3$ W/m/K . 180 K < T < 1500 K

Compound	a	b x 10^4	c x 10^8	d x 10^{11}
N_2	2.2678	1.02746	-6.0151	2.2332
O_2	1.5475	0.94154	-2.7529	0.5206
NH_3	9.1414	0.07295	21.665	-6.4465
NO	29.999	0.83047	-1.5185	0.1881
H_2O	56.198	0.15699	10.106	-2.4282
N_2O	83.454	0.93782	1.6490	0.1756

The Fuller correlation [23] is:

$$D_{AB} = 0.001 \frac{T^{1.75}(\frac{1}{M_a} + \frac{1}{M_b})^{0.5}}{P[(\sum V_a)^{1/3} + \sum (V_b)^{1/3}]^2} \tag{1}$$

Where the molecular weights M_i have units of g/mol, the Pressure P is atm, and the temperature T is in K. D_{AB} has units of cm^2/s.

Table 4: Diffusion volumes [23]

Compound	Diffusion Volume
N_2	17.9
O_2	16.6
NH_3	14.9
NO	11.2
H_2O	12.7
N_2O	35.9

Temperature profiles with turbulence

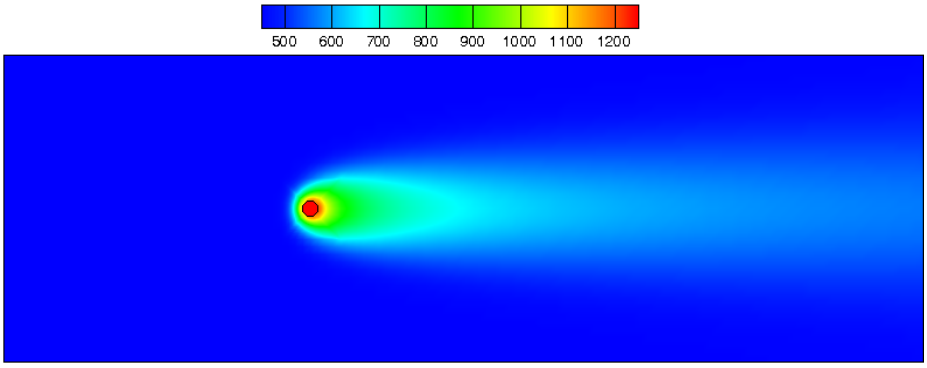

(a) Laminar flow

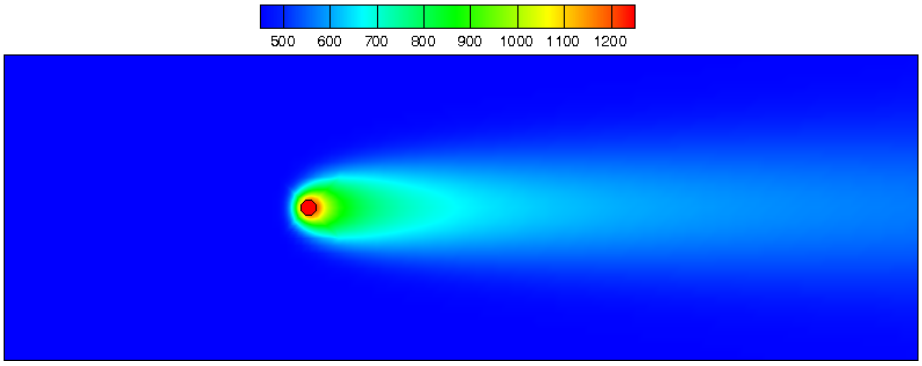

(b) Mean LES

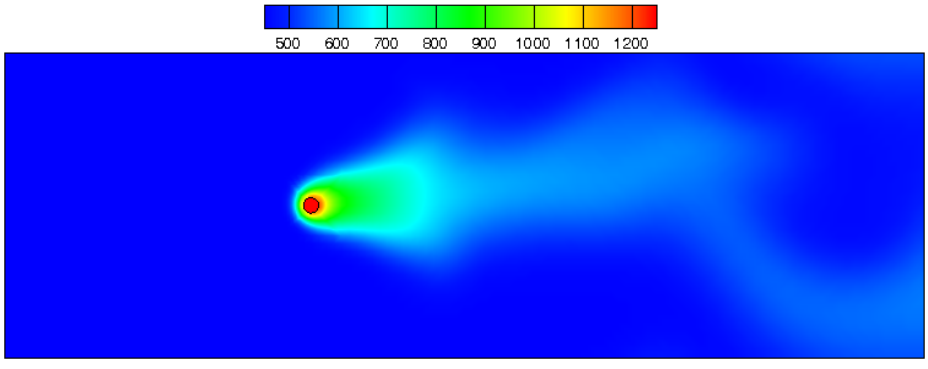

(c) LES at 12.5 τ

Figure 1: Contour plot of temperatures in (a) Laminar flow, (b) time averaged LES and (c) LES at t = 12.5 τ